Jordan Journal of
PHYSICS
An International Peer-Reviewed Research Journal

Volume 15, No. 4, Oct. 2022, Rabie2 1444 H

Jordan Journal of Physics (*JJP*): An International Peer-Reviewed Research Journal funded by the Scientific Research and Innovation Support Fund, Jordan, and published quarterly by the Deanship of Research and Graduate Studies, Yarmouk University, Irbid, Jordan.

Manuscripts should be submitted to:

Prof. Mahdi Salem Lataifeh
Editor-in-Chief, Jordan Journal of Physics
Deanship of Research and Graduate Studies
Yarmouk University-Irbid-Jordan
Tel. 00 962 2 7211111 Ext. 2075
E-mail: *jjp@yu.edu.jo*
Website: *http://Journals.yu.edu.jo/jjp*

Jordan Journal of
PHYSICS
An International Peer-Reviewed Research Journal

Volume 15, No. 4, Oct. 2022, Rabie2 1444 H

The Hashemite Kingdom of Jordan

Yarmouk University

Jordan Journal of

PHYSICS

An International Peer-Reviewed Research Journal

Funded by the Scientific Research and Innovation Support Fund

Volume 15, No. 4, Oct. 2022, Rabie2 1444 H

Instructions to Authors

Instructions to authors concerning manuscript organization and format apply to hardcopy submission by mail, and also to electronic online submission via the Journal homepage website (http://jjp.yu.edu.jo).

Manuscript Submission

1- **E-mail to** : jjp@yu.edu.jo

2- **Online**: Follow the instructions at the journal homepage website.

Original *Research Articles*, *Communications* and *Technical Notes* are subject to critical review by minimum of two competent referees. Authors are encouraged to suggest names of competent reviewers. *Feature Articles* in active Physics research fields, in which the author's own contribution and its relationship to other work in the field constitute the main body of the article, appear as a result of an invitation from the Editorial Board, and will be so designated. The author of a *Feature Article* will be asked to provide a clear, concise and critical status report of the field as an introduction to the article. *Review Articles* on active and rapidly changing Physics research fields will also be published. Authors of *Review Articles* are encouraged to submit two-page proposals to the Editor-in-Chief for approval. Manuscripts submitted in *Arabic* should be accompanied by an Abstract and Keywords in English.

Organization of the Manuscript

Manuscripts should be typed double spaced on one side of A4 sheets (21.6 x 27.9 cm) with 3.71 cm margins, using Microsoft Word 2000 or a later version thereof. The author should adhere to the following order of presentation: Article Title, Author(s), Full Address and E-mail, Abstract, PACS and Keywords, Main Text, Acknowledgment. Only the first letters of words in the Title, Headings and Subheadings are capitalized. Headings should be in **bold** while subheadings in *italic* fonts.

Title Page: Includes the title of the article, authors' first names, middle initials and surnames and affiliations. The affiliation should comprise the department, institution (university or company), city, zip code and state and should be typed as a footnote to the author's name. The name and complete mailing address, telephone and fax numbers, and e-mail address of the author responsible for correspondence (designated with an asterisk) should also be included for official use. The title should be carefully, concisely and clearly constructed to highlight the emphasis and content of the manuscript, which is very important for information retrieval.

Abstract: A one paragraph abstract not exceeding 200 words is required, which should be arranged to highlight the purpose, methods used, results and major findings**.**

Keywords: A list of 4-6 keywords, which expresses the precise content of the manuscript for indexing purposes, should follow the abstract.

PACS: Authors should supply one or more relevant PACS-2006 classification codes, (available at http://www.aip.org/pacs/pacs06/pacs06-toc.html)

Introduction: Should present the purpose of the submitted work and its relationship to earlier work in the field, but it should not be an extensive review of the literature (e.g., should not exceed 1 ½ typed pages).

Experimental Methods: Should be sufficiently informative to allow competent reproduction of the experimental procedures presented; yet concise enough not to be repetitive of earlier published procedures.

Results: should present the results clearly and concisely.

Discussion: Should be concise and focus on the interpretation of the results.

Conclusion: Should be a brief account of the major findings of the study not exceeding one typed page.

Acknowledgments: Including those for grant and financial support if any, should be typed in one paragraph directly preceding the References.

References: References should be typed double spaced and numbered sequentially in the order in which they are cited in the text. References should be cited in the text by the appropriate Arabic numerals, enclosed in square brackets. Titles of journals are abbreviated according to list of scientific periodicals. The style and punctuation should conform to the following examples:

1. Journal Article:

a) Heisenberg, W., Z. Phys. 49 (1928) 619.
b) Bednorz, J. G. and Müller, K. A., Z. Phys. B64 (1986) 189
c) Bardeen, J., Cooper, L.N. and Schrieffer, J. R., Phys. Rev. 106 (1957) 162.
d) Asad, J. H., Hijjawi, R. S., Sakaji, A. and Khalifeh, J. M., Int. J. Theor. Phys. 44(4) (2005), 3977.

2. Books with Authors, but no Editors:

a) Kittel, C., "Introduction to Solid State Physics", 8th Ed. (John Wiley and Sons, New York, 2005), chapter 16.
b) Chikazumi, S., C. D. Graham, JR, "Physics of Ferromagnetism", 2nd Ed. (Oxford University Press, Oxford, 1997).

3. Books with Authors and Editors:

a) Allen, P. B. "Dynamical Properties of Solids", Ed. (1), G. K. Horton and A. A. Maradudin (North-Holland, Amsterdam, 1980), p137.
b) Chantrell, R. W. and O'Grady, K., "Magnetic Properities of Fine Particles" Eds. J. L. Dormann and D. Fiorani (North-Holland, Amsterdam, 1992), p103.

4. Technical Report:

Purcell, J. "The Superconducting Magnet System for the 12-Foot Bubble Chamber", report ANL/HEP6813, Argonne Natt. Lab., Argonne, III, (1968).

5. Patent:

Bigham, C. B., Schneider, H. R., US patent 3 925 676 (1975).

6. Thesis:

Mahmood, S. H., Ph.D. Thesis, Michigan State University, (1986), USA (Unpublished).

7. Conference or Symposium Proceedings:

Blandin, A. and Lederer, P. Proc. Intern. Conf. on Magnetism, Nottingham (1964), P.71.

8. Internet Source:

Should include authors' names (if any), title, internet website, URL, and date of access.

9. Prepublication online articles (already accepted for publication):

Should include authors' names (if any), title of digital database, database website, URL, and date of access.

For other types of referenced works, provide sufficient information to enable readers to access them.

Tables: Tables should be numbered with Arabic numerals and referred to by number in the Text (e.g., Table 1). Each table should be typed on a separate page with the legend above the table, while explanatory footnotes, which are indicated by superscript lowercase letters, should be typed below the table.

Illustrations: Figures, drawings, diagrams, charts and photographs are to be numbered in a consecutive series of Arabic numerals in the order in which they are cited in the text. Computer-generated illustrations and good-quality digital photographic prints are accepted. They should be black and white originals (not photocopies) provided on separate pages and identified with their corresponding numbers. Actual size graphics should be provided, which need no further manipulation, with lettering (Arial or Helvetica) not smaller than 8 points, lines no thinner than 0.5 point, and each of uniform density. All colors should be removed from graphics except for those graphics to be considered for publication in color. If graphics are to be submitted digitally, they should conform to the following minimum resolution requirements: 1200 dpi for black and white line art, 600 dpi for grayscale art, and 300 dpi for color art. All graphic files must be saved as TIFF images, and all illustrations must be submitted in the actual size at which they should appear in the journal. Note that good quality hardcopy original illustrations are required for both online and mail submissions of manuscripts.

Text Footnotes: The use of text footnotes is to be avoided. When their use is absolutely necessary, they should be typed at the bottom of the page to which they refer, and should be cited in the text by a superscript asterisk or multiples thereof. Place a line above the footnote, so that it is set off from the text.

Supplementary Material: Authors are encouraged to provide all supplementary materials that may facilitate the review process, including any detailed mathematical derivations that may not appear in whole in the manuscript.

Revised Manuscript and Computer Disks

Following the acceptance of a manuscript for publication and the incorporation of all required revisions, authors should submit an original and one more copy of the final disk containing the complete manuscript typed double spaced in Microsoft Word for Windows 2000 or a later version thereof. All graphic files must be saved as PDF, JPG, or TIFF images.

Allen, P.B., "…….", in: Horton, G.K., and Muradudin, A. A., (eds.), "Dynamical…….", (North……..), pp….

Reprints

Twenty (20) reprints free of charge are provided to the corresponding author. For orders of more reprints, a reprint order form and prices will be sent with the article proofs, which should be returned directly to the Editor for processing.

Copyright

Disclaimer

Indexing

JJP is currently indexing in:

Scopus	ULRICHSWEB GLOBAL SERIALS DIRECTORY

Jordan Journal of
PHYSICS
An International Peer-Reviewed Research Journal

Volume 15, No. 4, Oct. 2022, Rabie2 1444 H

Table of Contents:

Volume 15, Number 4, 2022. pp. 331-341

Jordan Journal of Physics

ARTICLE

Shielding Properties of Glass Samples Containing Li_2O, K_2O, Na_2O, PbO and B_2O_3 by Geant4, XCOM and Experimental Data

Ali H. Taqi, Abdulahdi M. Ghalib and **Shlair I. Mohammed**

Department of Physics, College of Science, Kirkuk University, Kirkuk, Iraq.

Doi: **https://doi.org/10.47011/15.4.1**

Received on: 21/09/2020; *Accepted on: 05/04/2021*

Abstract: In the present work, glass samples containing $10Li_2O$, $10K_2O$, $20Na_2O$. xPbO, $(60\text{-}x)B_2O_3$ (where x = 0-60) were prepared by the melt quenching method. The shielding parameters of the prepared samples were measured experimentally and calculated theoretically. The measurements have been performed at energies of 356.5, 662, 1173 and 1333 keV to obtain the total mass attenuation coefficient (μ_m), using a gamma spectrometer containing a shielded NaI (TI) detector. The results of mass attenuation coefficient (μ_m), half-value layers (HVLs), mean free path (MFP), radiation protection efficiency (RPE), atomic and electronic electron cross-sections (σ_a and σ_e), effective atomic number (Z_{eff}) and effective electron number (N_{eff}) were calculated at energies from 1 keV to 100 GeV using the Monte Carlo simulation code Geant4 and XCOM. The calculated results were compared with each other and with the experimental values. Good agreement has been observed.

Keywords: Shielding properties, Glass, Photon mass attenuation coefficient, Atomic and electronic cross-sections, Effective atomic and electron numbers, XCOM, Geant4.

Introduction

Exposure to or using ionizing rays can cause damage. Such damage can be controlled, particularly by the shielding method, because it gives a good working-safety level [1]. The study of interaction of radiation with matter is an important research field for the evolution of substances that can be used in a high-radiation setting [2-4]. The intensity of the radiation gradually decreases, as a result of a sequence of interactions, where the linear attenuation coefficient (μ) can be defined as the probability per unit length that a radiation will undergo an interaction in the material [5]. Due to the many and important uses of radioactive isotopes in medical and industrial applications, it became necessary to evolve materials that are used in protection [6].

There is an ongoing need to find more designs suitable for radiation protection. The shielding parameters, such as total linear attenuation coefficient (μ), mass attenuation coefficient ($\mu_m=\mu/\rho$), half-value layers (HVLs), mean free path (MFP), radiation protection efficiency (RPE), electronic and atomic cross sections (σ_e and σ_a), effective atomic and electron numbers (Z_{eff} and N_{eff}), are major for testing materials in radiation protection [7]. From the shielding point of view, it is known that an increase in μ_m, Z_{eff} and N_{eff} values enhances the gamma-ray shielding properties, while less MFP and HVL values clearly indicate improving the gamma-ray shielding performance of the absorbent material.

Glass has a set of features that make it useful and important in radiation shielding, like transparency, high homogeneity that can be attained and accepting a wide range of composition. Many experimental and theoretical

Corresponding Author: Ali H. Taqi **Email**: alitaqi@uokirkuk.edu.iq

studies of glass shielding parameters have been investigated at different energies, such as bismuth borate glasses [8], PbO–SiO_2 glasses [9], xPbO:(100-x) B_2O_3 glasses at 662 keV [10], phosphate glass containing Bi_2O_3, PbO and BaO at 662 keV [11], silicate glasses containing Bi_2O_3, BaO and PbO in the energy region of 1 keV to 100 GeV [12], lead zinc borate glasses [13], heavy-metal oxide glasses [14, 15], PbO-Li_2O-B_2O_3 glasses [16], PbO-B_2O_3, PbO-SiO_2, PbO-GeO_2 and PbO-WO_3-TeO_2 glass systems [17], xPbO-(100-x) P_2O_5 glasses [18] and PbO-Na_2O-B_2O_3-CaO-Al_2O_3-SiO_2 glasses [19].

The purpose of this study is to prepare glass samples containing $10Li_2O$. $10K_2O$. $20Na_2O$. xPbO. (60-x)B_2O_3, where x varies between 0 and 60. We studied the shielding parameters of the samples theoretically by using the Monte Carlo simulation code Geant4 and the XCOM program in the energy range of 1 keV-100 GeV. This was experimentally investigated by using a gamma spectrometer that contains a shielded NaI(Tl) detector at the energies of (356.5 keV)^{133}Ba, (662 keV)^{137}Cs, (1173, 1333 keV)^{60}Co. The calculated results will be compared between XCOM and Geant4 and compared with the experimental values.

Theory

The total mass attenuation coefficient (μ_m=μ/ρ) measures the gamma photon interaction probability (absorption or scattering) with the matter. The μ_m can be used to evaluate different shielding parameters. The common methods to evaluate μ_m of any material is explained with the following Lambert-Beer law [20, 21]:

$$I = I_0 e^{-\mu_m x \rho} \quad (1)$$

where I and I_0 are photon intensity with sample and without sample, ρ (g cm^{-3}) and x(cm) are the material density and the absorber thickness, respectively. μ_m of chemical compounds in terms of the weight fraction w_i can be calculated by [22]:

$$\mu_m = \sum_i w_i (\mu_m)_i \quad (2)$$

where w_i is expressed in terms of the atomic weight A as:

$$w_i = \frac{n_i A_i}{\sum_j n_j A_j} \quad (3)$$

where n_i is the number of formula units.

The half-value layer (HVL) is important to determine the material effectiveness against radiation and can be obtained by:

$$\mathrm{HVL} = \frac{\ln(2)}{\mu}. \quad (4)$$

Reducing the photon intensity by 1/e is known as the mean free path (MFP):

$$\mathrm{MFP} = \frac{1}{\mu}. \quad (5)$$

The effective atomic number (Z_{eff}) can be expressed in terms of the total atomic effective cross-section (σ_a) and the total electronic effective cross-section (σ_e) [23]:

$$Z_{\mathrm{eff}} = \frac{\sigma_a}{\sigma_e} \quad (6)$$

where σ_a and σ_e are evaluated by the following equations:

$$\sigma_a = \frac{1}{N_A} \sum_i f_i A_i (\mu_m)_i \quad (7)$$

$$\sigma_e = \frac{1}{N_A} \sum_i \frac{f_i A_i}{Z_i} (\mu_m)_i. \quad (8)$$

Z_{eff} is closely related to the average number of electrons per unit mass N_e [22]:

$$N_e = \frac{\mu_m}{\sigma_e} \quad (9)$$

The radiation protection efficiency (RPE) value can be obtained using the following expression:

$$\mathrm{RPE} = (1 - I/I_0) \times 100. \quad (10)$$

Materials and Methods

Sample Preparation

In the present work, seven glass samples were prepared using the melt quenching technique for the chemical formula: $10Li_2O$. $10K_2O$. $20Na_2O$. xPbO. (60-x) B_2O_3, where x takes the values 0, 10, 20, 30, 40, 50 and 60. Pure powder of the chemical compounds: H_3BO_3, Li_2CO_3, K_2CO_3, Na_2CO_3, PbO were used in the preparation of the samples. These compounds were weighed using an electronic balance having an accuracy of the order of 0.001g and mixed in a mortar for 10 minutes to prepare a 20-g batch of each composition. The alumina ceramic crucible containing the mixture was placed in an electric furnace at 1000 °C for 1 hour until being fully molten. The molten mixture will be converted into oxides of Li_2O, K_2O, Na_2O, PbO, and B_2O_3. The molten mixture was poured into a stainless

steel mold inside an annealing furnace at 200 °C and kept for 2 hours, then slowly cooled to room temperature. The density of the investigated glass samples was measured using the Archimedes principle. The symbols and the densities of the prepared glass samples are given in Table 1, where the concentration of PbO and B_2O_3 varies from 0 to 60%, respectively.

Experimental Procedures

The experimental measurements were performed using a gamma spectrometer containing an NaI(TI) detector. The experimental arrangement is shown in Fig. 1. To reduce the background radiation, the whole system was shielded with 5 cm lead, 0.5 cm copper and 0.5 cm steel. The radioactive sources ^{133}Ba (356.5 keV), ^{137}Cs (662 keV), ^{60}Co (1173, 1333 keV) were used to obtain the mass attenuation coefficients. The background of the system is taken for 900s, the number of counts I_o of gamma particles was measured for each path length and then, by inserting the glass sample, the number of gamma counts I was recorded.

The theoretical calculations of the investigated samples are carried out by XCOM program and simulated by the Monte Carlo code Geant4 at the photon energies 1 keV-100 GeV. The gamma-ray shielding parameters of the prepared glass samples as functions of the incident photon energy and the chemical composition were calculated.

TABLE 1. Symbols and densities of the prepared glass samples.

Symbol	Composition $10Li_2O.10K_2O.20Na_2O.xPbO.(60-x)B_2O_3$ x varied as 0, 10, 20, 30, 40, 50 and 60	ρ(g cm^{-3})
S1	$10Li_2O.10K_2O.20Na_2O.0PbO.60B_2O_3$	2.3724
S2	$10Li_2O.10K_2O.20Na_2O.10PbO.50B_2O_3$	3.0699
S3	$10Li_2O.10\ K_2O.20Na_2O.20PbO.40B_2O_3$	3.3904
S4	$10\ Li_2O.10K_2O.20Na_2O.30PbO.30B_2O_3$	3.8453
S5	$10Li_2O.10K_2O.20Na_2O.40PbO.20B_2O_3$	4.0063
S6	$10Li_2O.10K_2O.20Na_2O.50PbO.10B_2O_3$	4.4495
S7	$10Li_2O.10K_2O.20Na_2O.60PbO.0B_2O_3$	5.0863

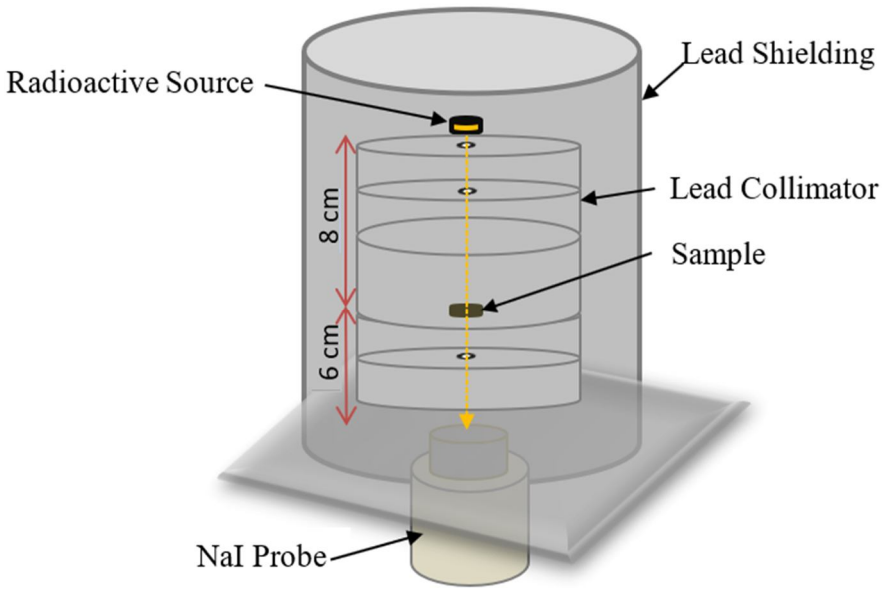

FIG. 1. Experimental arrangement to obtain the gamma attenuation coefficients.

Computational Methods

The computational calculations of the prepared glass samples were carried out using XCOM program and simulated by the Monte Carlo code Geant4 within the photon energy range from 1 keV to 100 GeV; then, all the parameters of radiation shielding were calculated as functions of the energy of the incident photon.

All the elements, materials and compounds were defined. The geometry is constructed to evaluate the initial and final numbers of photons before and after passing the samples (I_0 and I of Eq. 1), respectively. The XCOM program is available online, while the Gent4 code for windows has been installed and the TestEM13 project was executed after setting the type of the particle and its energy. More details can be found in Ref. [24].

Results and Discussion

The theoretical μ_m values of the prepared glass samples have been evaluated at the photon energies ranging from 1 keV to 100 GeV using the XCOM program and the simulation code Geant4. To understand the change of the μ_m values with photon energy, the obtained results are plotted in Fig. 2 and compared to the experimental values. It is seen that μ_m decreases when the photon energy increases to 15 MeV and many peaks are observed in the low photon energy region (< 100 keV) due to the K–, L– and M–photoelectric absorption edges. The sudden increases in μ_m are due to photoelectric absorption of photons, which usually occurs at an energy just above the binding energy of the electron in the shell.

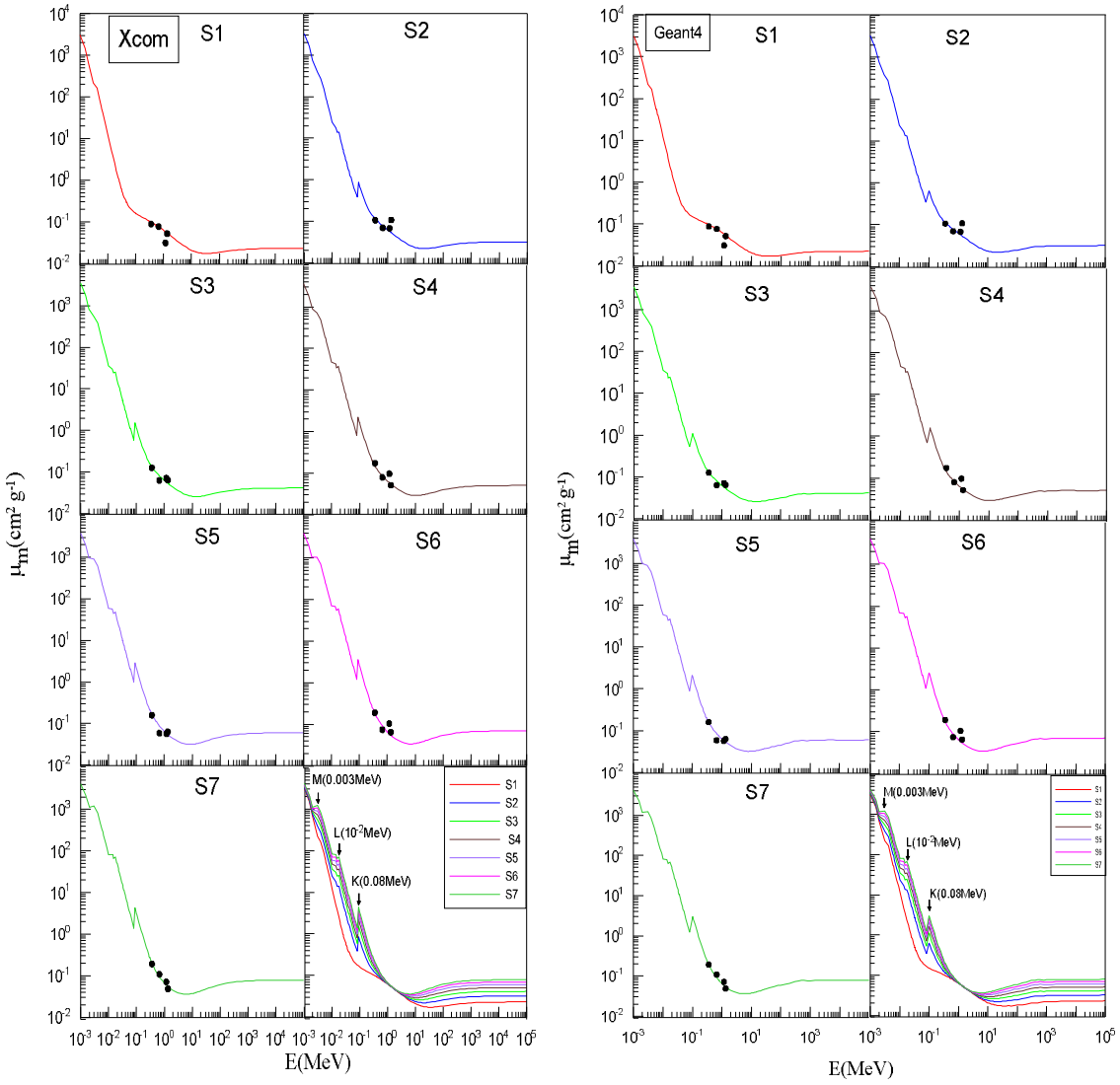

FIG. 2. Calculated μ_m values of the prepared glass samples in comparison with our experimental data.

As can be seen from Fig. 2, the behavior of μ_m against photon energy depends on the chemical composition of the prepared samples and on the nature of the photon interaction with the samples, which includes three main processes: photoelectric effect, Compton scattering and pair-production, where the effects of the three processes vary according to energies.

The values of μm, taken by using XCOM program, were slightly higher than Geant4 code values for low energies. The relative deviations between the calculated results of Geant4 and XCOM, defined as:

$$RD\% = ((\mu_m)_{XCOM} - (\mu_m)_{Geant4} / (\mu_m)_{XCOM}) \times 100),$$

are plotted in Fig. 3. There is a satisfactory agreement between experiment and theory. The experimental data was lower than the theoretical values; therefore, the Geant4 values are more close to the experiment.

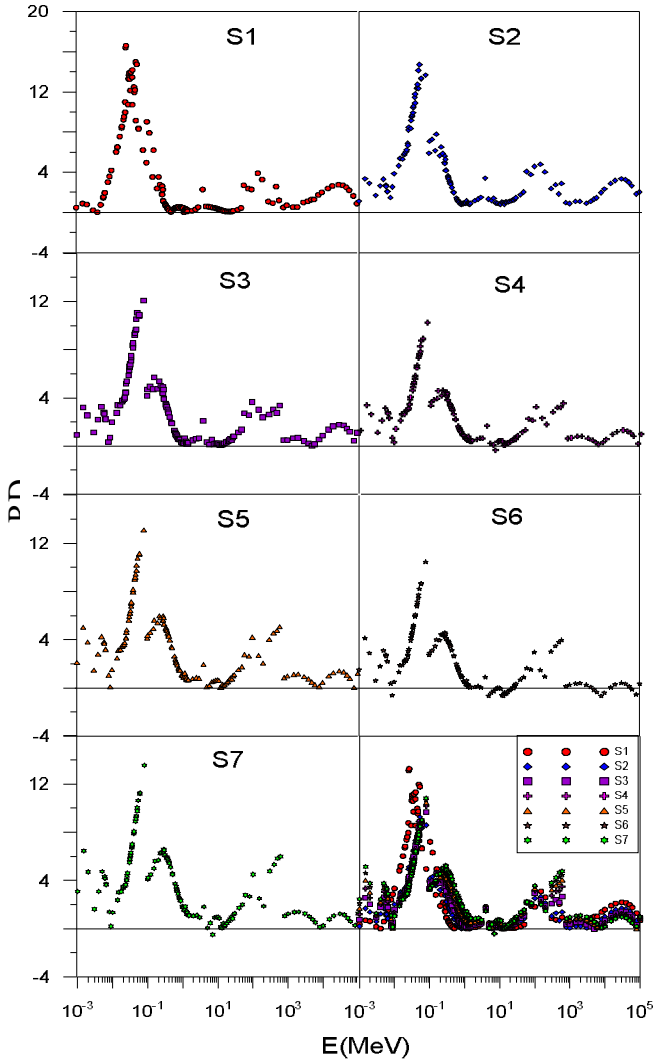

FIG. 3. Relative difference (RD%) between XCOM and Geant4 results of the investigated glass samples at the energy range (1 keV-100 GeV).

The radiation shielding features are observed to be significantly enhanced, by adding heavy elements to the prepared glass samples, as shown in Fig. 4. Although the increase in PbO concentration causes an increase in μ_m, yet the B_2O_3 concentration will decrease which will affect the transparency of the glass samples. The absorption edge increased with increasing the PbO concentration. Our results are compatible with the results of Refs. [16, 25], as illustrated in Table 2.

The variations of the half-value layers (HVLs) and the mean free path (MFP) of the investigated glass samples are illustrated in Figs. 5 and 6, respectively at photon energies varying from 1 keV to 100 GeV. It has been found that the HVL and MFP values are initially low and increase gradually with an increase in the incident photon energy up to 3 MeV. Above 3 MeV, the rate of decrease of HVL and MFP values is weak with the incident energy. It is clear that the increase in the PbO concentration leads to a decrease in the HVL and MFP values. Also, it was found that the absorption edges of

sample S7 are lower than the absorption edges of the other samples, as shown in Figs. 5 and 6. The radiation protection efficiencies (RPEs) of the prepared glasses are presented in Table 3, where sample S7 is observed to possess high values of RPE.

TABLE 2. Experimental values of μ_m of the investigated glass samples in comparison with those of Refs. [16, 25].

E (keV)	$10Li_2O.10K_2O.20Na_2O.0PbO.60B_2O_3$ Sample S1 of this work	$35PbO.25Li_2O.40B_2O_3$ Ref. [16]	$35Li_2O.10ZnO.55B_2O_3$+ $0MnO_2$wt% Ref. [25]
	μ_m (cm^2 g^{-1})	μ_m (cm^2 g^{-1})	μ_m (cm^2 g^{-1})
356.5	0.0875	0.2150	0.0962
662	0.0762	0.0968	0.0742
1173	0.0679	0.0589	0.0566
1333	0.0515	0.0539	0.0532
	$10Li_2O.10K_2O.20Na_2O.60PbO.0B_2O_3$ Sample S7 of this work	$60PbO.0Li_2O.40B_2O_3$ Ref. [16]	$35Li_2O.10ZnO.55B_2O_3$+ $2MnO_2$wt% Ref. [25]
356.5	0.1916	0.2400	0.0965
662	0.1082	0.1010	0.0744
1173	0.0713	0.0601	0.0568
1333	0.0646	0.0551	0.0534

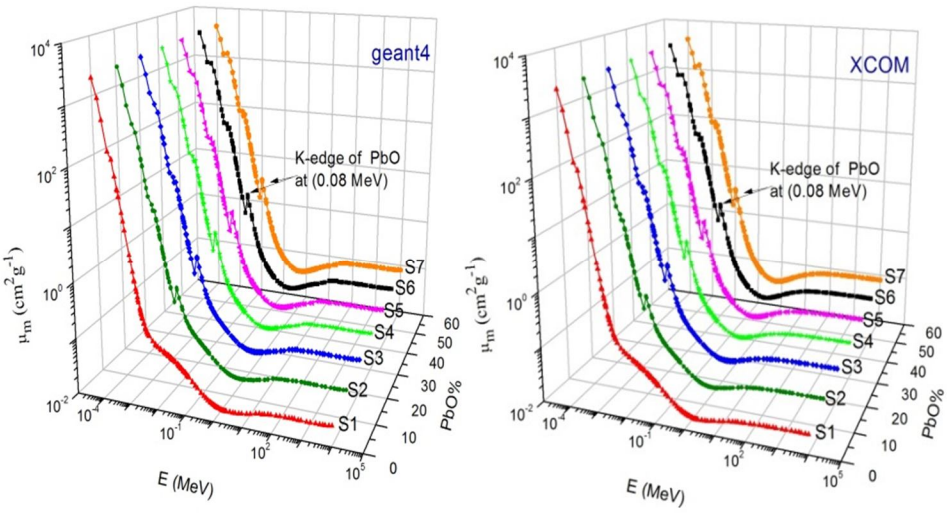

FIG. 4. XCOM and Geant4 mass attenuation coefficient values compared with PbO concentrations of the prepared samples.

TABLE 3. Radiation protection efficiency RPE of the investigated glass samples S1, S5 and S7.

E (keV)	RPE (%)		
	S1	S5	S7
356.5	13.13097	40.18667	54.51057
662	11.53693	17.26499	35.89933
1173	4.83808	16.67967	25.92019
1333	7.961957	18.50337	18.07065

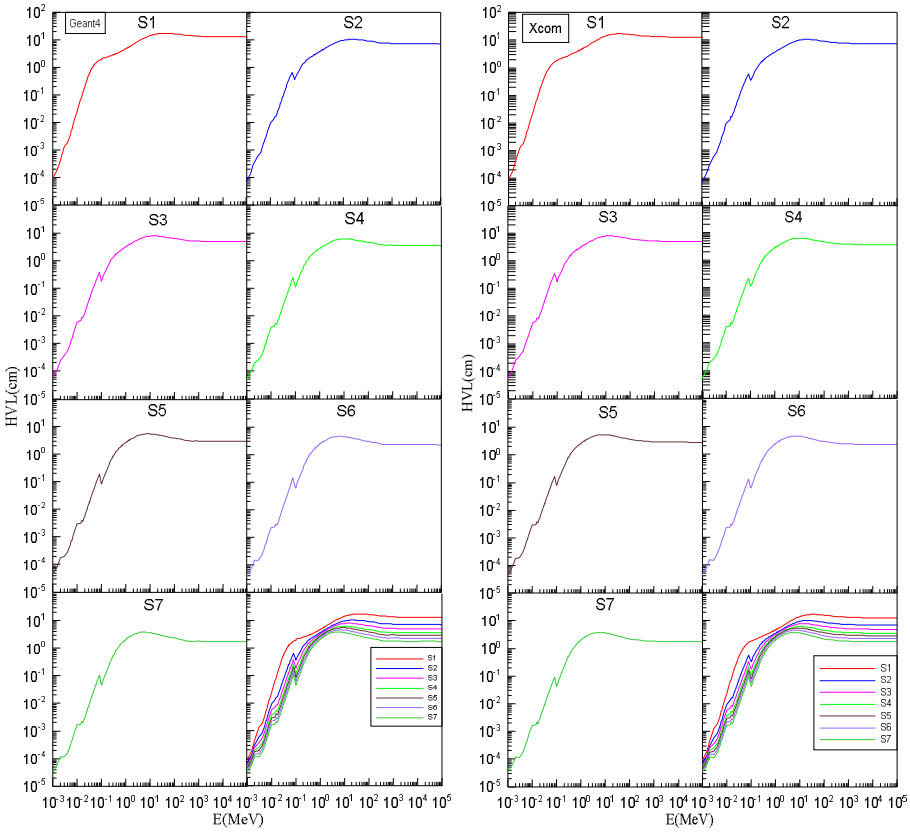

FIG. 5. Calculated half-value layers (HVLs) for the prepared samples against energy ranging from 1 keV to 100 GeV using the XCOM program and the simulation code Geant4.

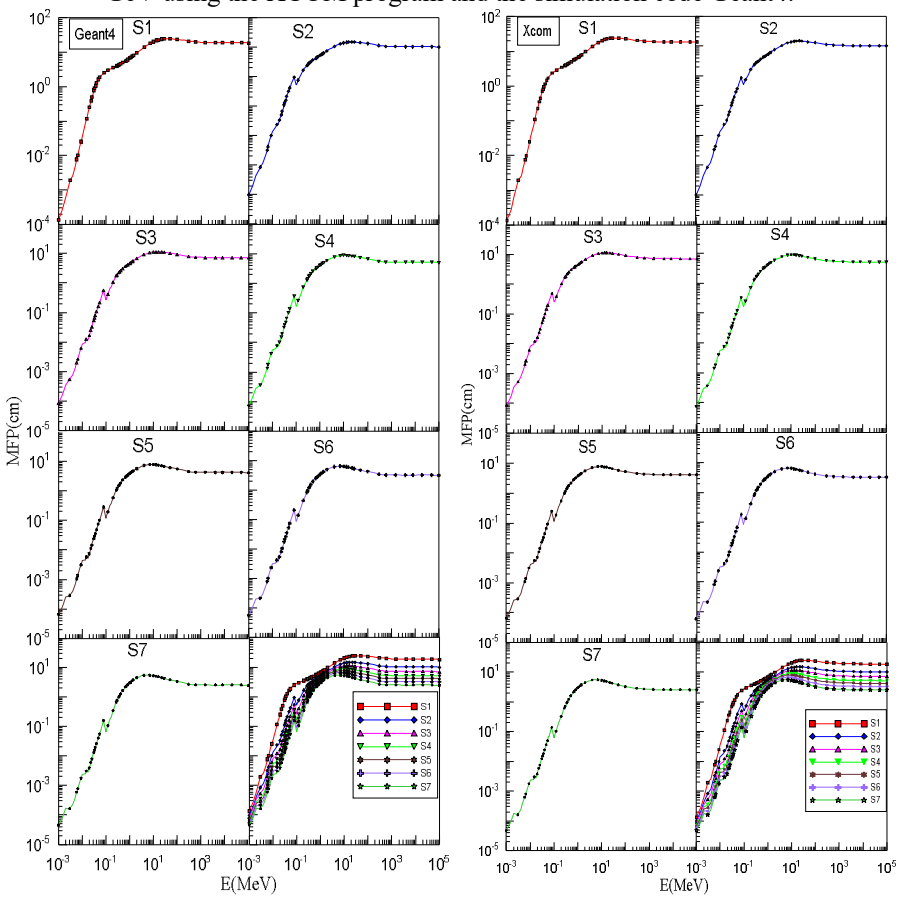

FIG. 6. Calculated mean free path (MFP) for the prepared samples against energy ranging from 1 keV to 100 GeV using the XCOM program and the simulation code Geant4.

The Geant4 and XCOM calculations of the atomic and electronic cross-sections (σ_a and σ_e) in the photon energy range (1 keV-100 GeV) are presented in Figs. 7 and 8. The results show that the cross-sections decrease with the energy of the incident photon for all the investigated samples and the cross-sections improved by increasing the PbO concentration over the energy range, due to high *A*. The photoelectric and pair production effects are dominant by high *A* of samples at low- and high-energy regions. The Compton effect predominates gradually and is almost independent of *A* of the constituent elements at the intermediate-energy region.

The Geant4 and XCOM calculations of the effective atomic number (Z_{eff}) and the effective electron number (N_{eff}) for the prepared glass samples in the photon energy range (1 keV-100 GeV) are illustrated in Figs. 9 and 10. Z_{eff} and N_{eff} values of the prepared samples increase with the increase of PbO concentration. The Z_{eff} and N_{eff} values show a broad peak and a maximum value at 0.01 MeV and a minimum at 1 MeV. Above 1 MeV, the values tend to be constant. The discontinuous jumps in Z_{eff} and N_{eff} for the low-energy region (< 100 keV) may be related to the photoelectric absorption edge of Pb, which is shown in Fig. 2, where the sharp peak is observed at 0.08 MeV due to K absorption edge. Also, the variations of Z_{eff} and N_{eff} with photon energy may be attributed to the relative domination of the photoelectric effect, Compton scattering and pair production, at different energy regions. The minimum Z_{eff} is found in the intermediate-energy region (around 1 MeV). In this region, Compton scattering is the dominant photon interaction process. Beyond 1 MeV, the Z_{eff} value increases because of the fact that the predominance of pair production ends to be constant. Our findings are consistent with those of Ref. [17].

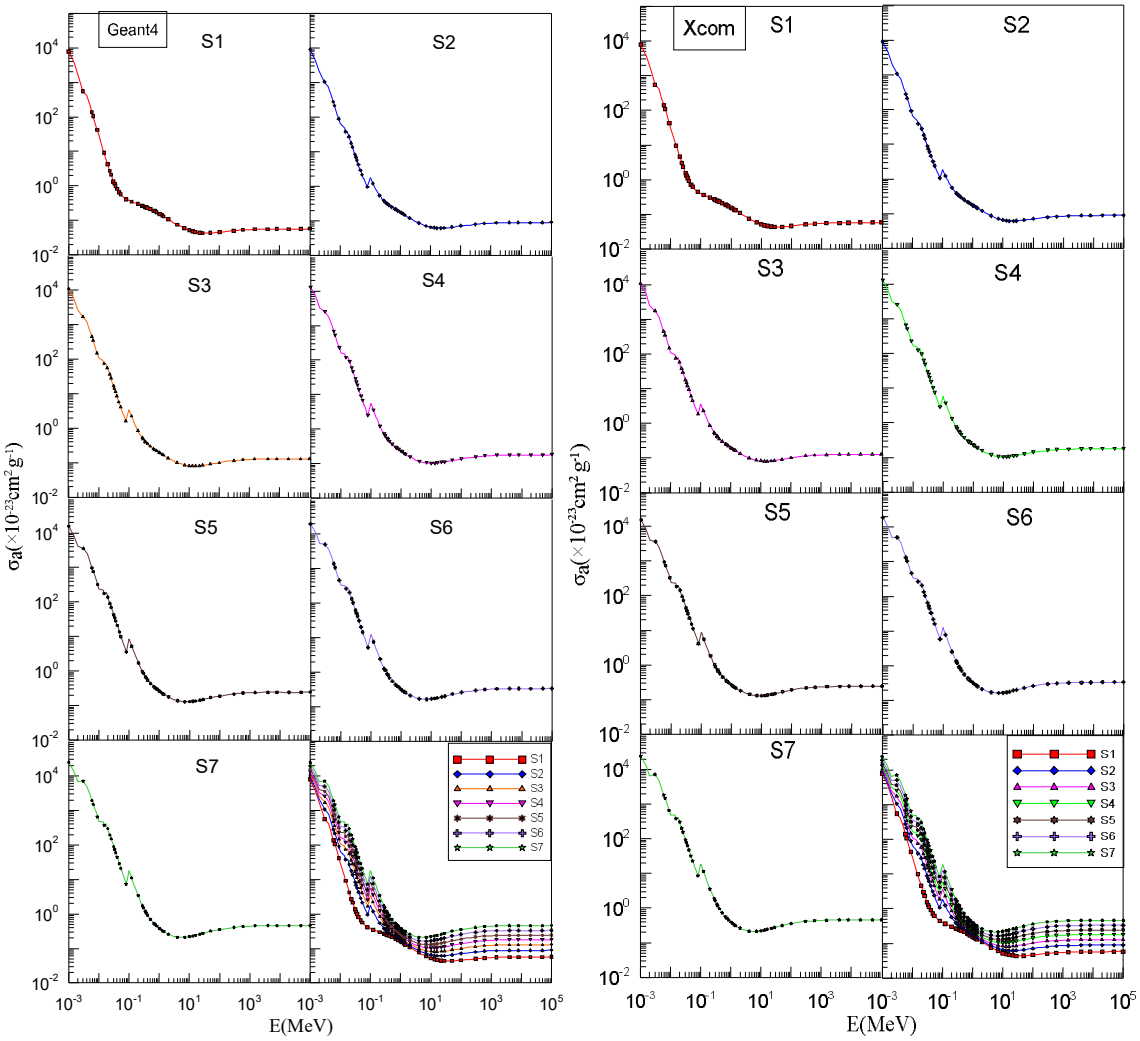

FIG. 7. Calculated atomic cross-sections (σ_a) for the prepared samples against energy ranging from 1 keV to 100 GeV using the XCOM program and the simulation code Geant4.

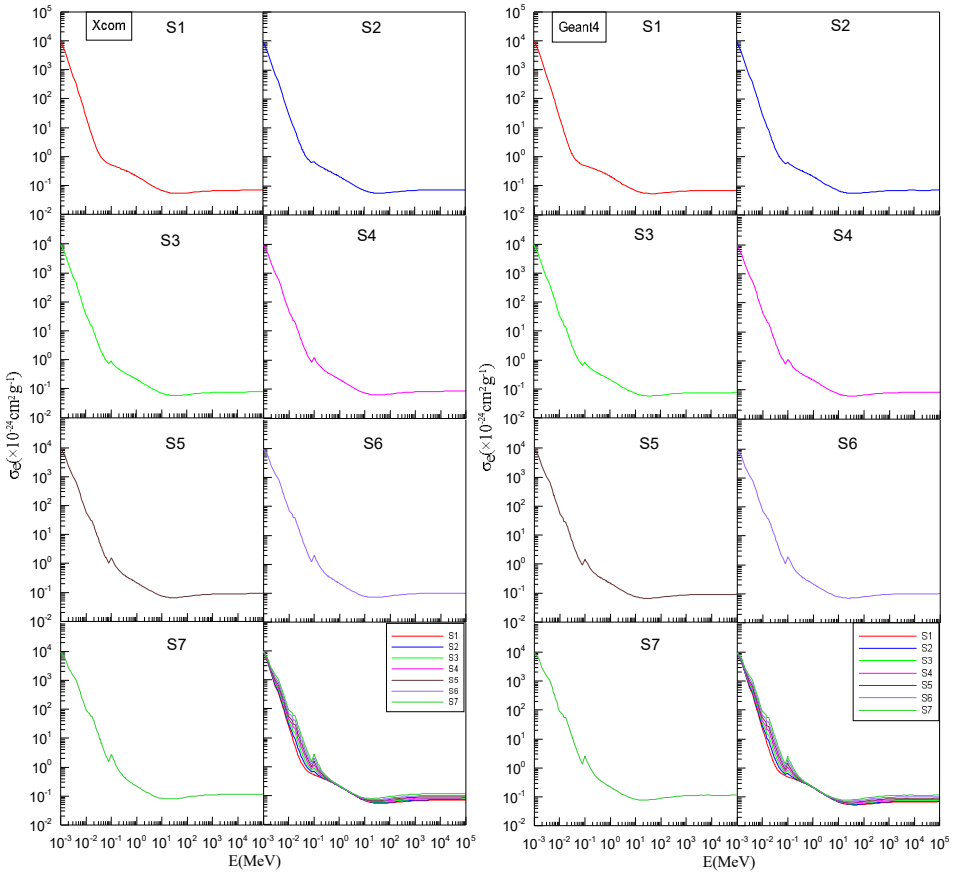

FIG. 8. Calculated electron cross-sections (σ_e) for the prepared samples against energy ranging from 1 keV to 100 GeV using the XCOM program and the simulation code Geant4.

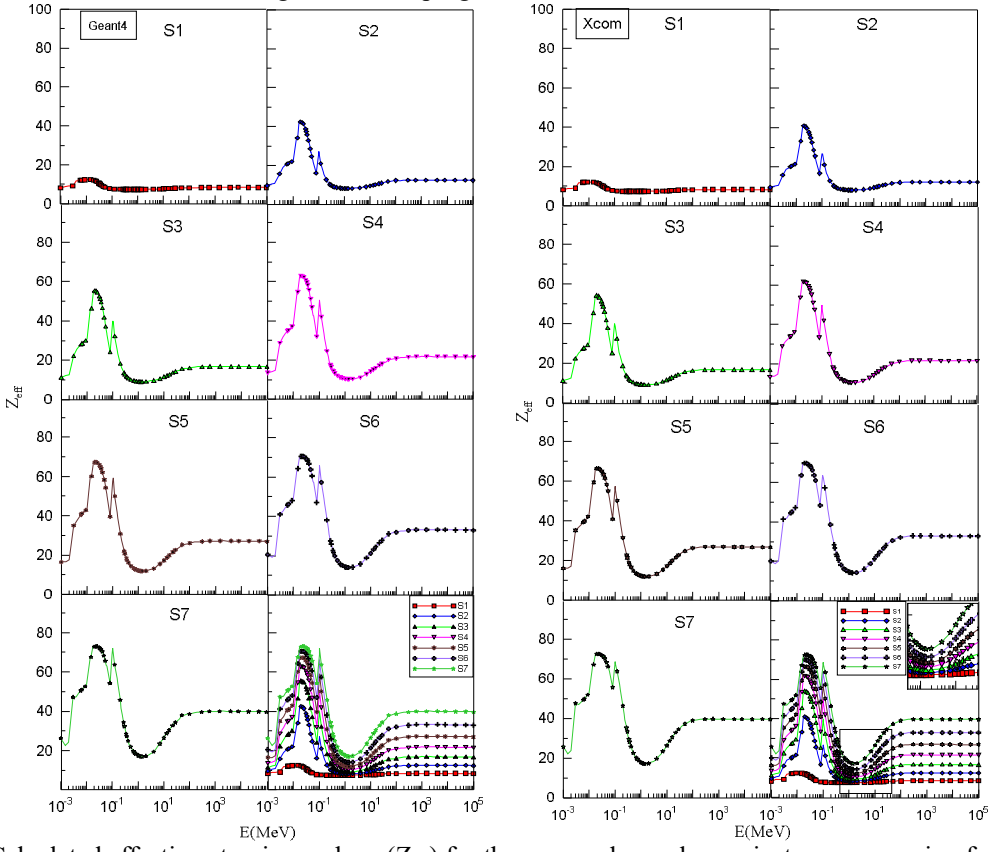

FIG. 9. Calculated effective atomic numbers (Z_{eff}) for the prepared samples against energy ranging from 1 keV to 100 GeV using the XCOM program and the simulation code Geant4.

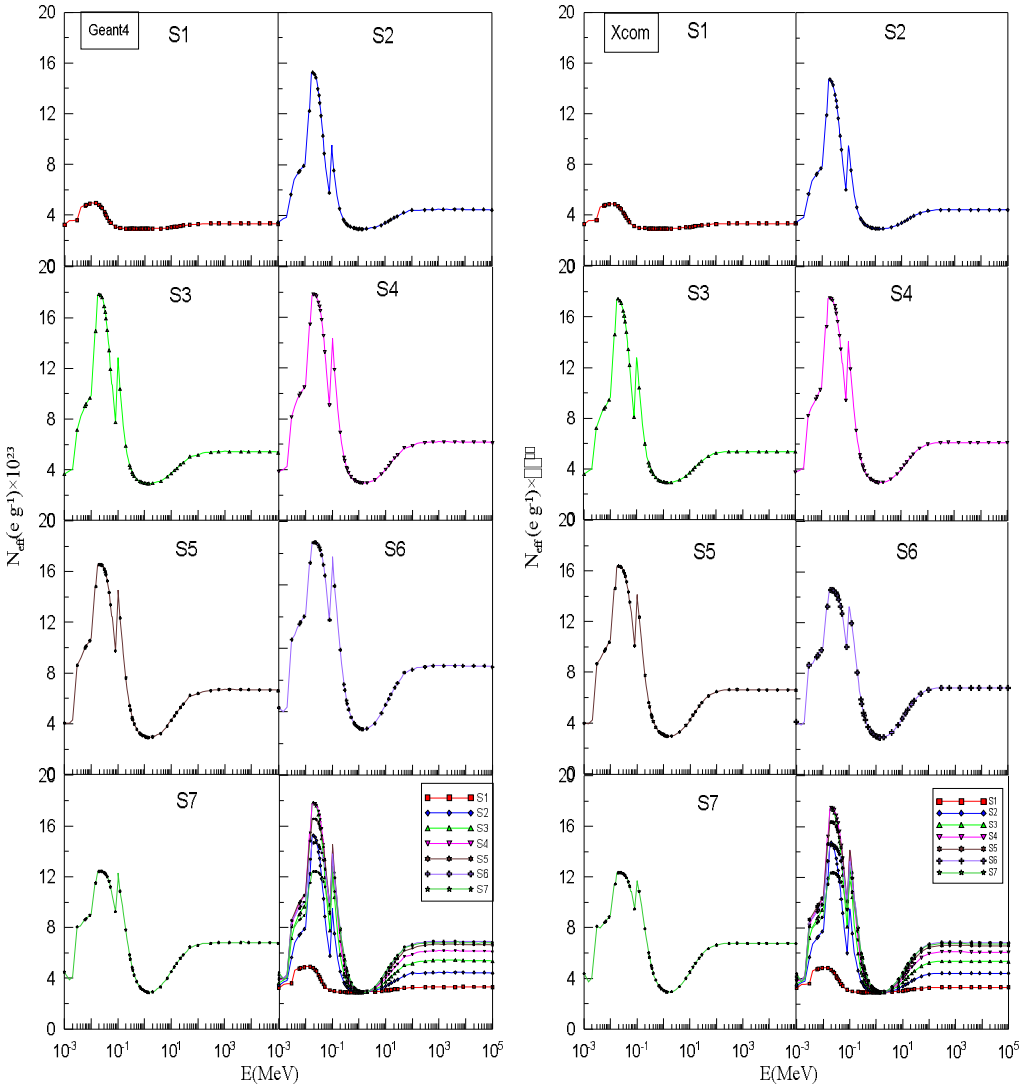

FIG. 10. Calculated effective electron numbers (N_{eff}) for the prepared samples against energy ranging from 1 keV to 100 GeV using the XCOM program and the simulation code Geant4.

Conclusions

The shielding parameters (μ_m, HVL, MFP, RPE, σ_a, σ_e, Z_{eff} and N_{eff}) of the investigated glass samples containing Li_2O, K_2O, Na_2O, PbO, and B_2O_3 have been calculated from 1 keV to 100 GeV as photon energy using the XCOM program and the simulation Monte Carlo code Geant4. The calculated results were compared with each other and with the experimental values at experimental data of 356.5, 662, 1173 and 1332 keV using a shielded Na(Tl) detector. Good agreement was obtained. It was found that the attenuation properties increased with the increase in the PbO concentration. The highest value of radiation protection efficiency was for sample S7 ($10Li_2O.10K_2O.20Na_2O.60PbO.0B_2O_3$), which has been found to be the most effective shielding material. The Z_{eff} and the N_{eff} values show a broad peak and a maximum value at 0.01 MeV and a minimum at 1 MeV. Above 1 MeV, the values tend to be constant. The used theoretical methods succeeded in describing the samples. Therefore, it will be preferable to obtain the photon shielding characteristics of the glass, particularly in cases where no experimental data exist. However, the XCOM program results were slightly higher than those given by the Geant4 code. Experimental data was lower than the theoretical values, where the Geant4 values are closer to the experiment.

References

[1] Ahmed, K.O., "Introduction to Health Physics", (Bookshop for Printing and Publishing, University of Mosul, 1993).

[2] Kaur, U., Sharma, J.K., Singh, P.S. and Singh, T., Applied Radiation and Isotopes, 70 (1) (2012) 233.

[3] Singh, C., Singh, T., Kumar, A. and Mudahar, G.S., Annals of Nuclear Energy, 31 (10) (2004) 1199.

[4] Bashter, I., Annals of Nuclear Energy, 24 (17) (1997) 1389.

[5] Wood, J., "Computational methods in reactor shielding", (Elsevier, Amsterdam, Netherlands, 2013).

[6] Krocher, J.F. and Browman, R.E., "Effects of Radiation on Materials and Components", Eds. Reinhold, (New York, 1984).

[7] Hubbell, J.H., International Journal of Applied Radiation and Isotopes, 33 (1982) 1269.

[8] Singh, K., Singh, H., Sharma, V., Nathuram, R., Khanna, A., Kumar, R. et al., Nuclear Instruments and Methods in Physics Research-Section B: Beam Interactions with Materials and Atoms, 194 (1) (2002) 1.

[9] Singh, K.J., Singh, N., Kaundal, R.S. and Singh, K., Nuclear Instruments and Methods in Physics Research B, 266 (2008) 944.

[10] Kirdsiri, K., Kaewkhao, J., Pokaipisit, A., Chewpraditkul, W. and Limsuwan, P., Annals of Nuclear Energy, 36 (2009) 1360.

[11] Kaewkhao, J. and Limsuwan, P., Nuclear Instruments and Methods in Physics Research A, 619 (2010) 295.

[12] Chanthima, N., Kaewkhao, J. and Limsuwan, P., Annals of Nuclear Energy, 41 (2012) 119.

[13] El-Kameesy, S.Y., Abd El-Ghany, S., Azooz, M.A. and El-Gammam, Y.A., World Journal of Condensed Matter Physics, 3 (2013) 198.

[14] El-Khayatt, A.M., Ali, A.M. and Singh, V.P., Nuclear Instruments and Methods in Physics Research A, 735 (2014) 207.

[15] Kaur, P., Singh, D. and Singh, T., Nuclear Engineering and Design, 307 (2016) 364.

[16] Kumar, A., Radiation Physics and Chemistry, 136 (2017) 50.

[17] El-Mallawany, R., Sayyed, M.I., Dong, M.G. and Rammah, Y.S., Radiation Physics and Chemistry, 151 (2018) 239.

[18] Shams, A.M.I., Tekin, H.O., Erguzel, T.T. and Susoy, G., Applied Physics A: Material Science and Processing, 125 (2019) 640.

[19] Shams, A.M.I., Yasser, B. Saddeek, M.I.S., Tekin, H.O. and Kilicoglu, O., Composites-Part B, 167 (2019) 231.

[20] Davisson, C.M., "Gamma-ray Attenuation Coefficients". In: Siegbahn (Ed.), Alpha-, beta- and gamma-ray spectroscopy (Vol. 1). (North Holland, Amsterdam, 1965).

[21] Taqi, A.H., Al Nuaimy, Q.A.M. and Gulalla, A.K., Journal of Radiation Research and Applied Sciences, 9 (2016) 256.

[22] Manohara, S.R. and Hanagodimath, S.M., Nucl. Instrum. Methods Phys. Res. B, 258 (2007) 321.

[23] Manohara, S.R., Hanagodimath, S.M., Thind, K.S. and Gerward, L., Nucl. Instrum. Methods Phys. Res. B, 266 (2008) 388.

[24] Taqi, A.H. and Khalil, H.J., Journal of Radiation Research and Applied Sciences, 10 (2017) 252.

[25] Rammah, Y.S., Abouhaswa, A.S., Salama, A.H. and El‐Mallawany, R., Journal of Theoretical and Applied Physics, 13 (2019) 155.

Volume 15, Number 4, 2022. pp. 343-352

Jordan Journal of Physics

ARTICLE

Comparing the Dielectric Properties of Papaya Oil with Mineral Insulating Liquid under Temperature Variation

Olatunde A. Oyelaran[a], **Faralu M. Sani**[b], **Kazeem A. Bello**[a], **James O. Abioye**[a] and **Olayinka E. Olumoko**[c]

[a] *Department of Mechanical Engineering, Federal University Oye-Ekiti, Nigeria.*
[b] *Department of Mechanical Engineering, Usumanu Danfodio University Sokoto, Nigeria.*
[c] *Heavy Equipment and Machinery Development Institute, Bauchi, Nigeria.*

Doi: **https://doi.org/10.47011/15.4.2**
Received on: 01/11/2020; *Accepted on: 01/03/2021*

Abstract: The world's energy requisite has been controlled by petroleum oil for a long time in transportation, household and power sectors. Mineral Transformation Oil (MTO), being an essential insulating material in transformers, has been used for over fifteen decades. MTO application in the power sector could be hazardous to the environment, especially during a transformer explosion which may cause a spill of oil to the soil or water stream. Owing to the threat of MTO to environment aspects, alternative insulating oil with biodegradable characteristics has attracted a lot of devotions in recent studies. To validate the aptness of using Purified Papaya Seed Oil (PPSO) as an insulating fluid in an electric transformer, it is vital to compare dielectric properties of PPSO with that of MTO insulating liquid. This study presents a comparison of temperature effect on dielectric properties of PPSO with the MTO insulating liquid. Breakdown voltage, dissipation factor (tan δ) and dielectric constant were measured by existing established testing standards. The breakdown voltage was determined by IEC 156 standard test method, whereas the dissipation factor and dielectric constant were determined based on IEC 60247 standard test method. The results revealed that the variation of dielectric properties of PPSO due to temperature change was similar to that of MTO. However, the dissipation factors and breakdown voltages of dielectric properties of PPSO were better when compared with those of MTO at higher temperatures, but with a slight decrease in dielectric constants with the increase in temperature.

Keywords: Papaya seed oil, Dissipation factor, Dielectric constant, Breakdown voltage, Temperature, Transformer.
PACS: 77.84. Nh, 88.05. Lg.

Introduction

Power transformers are indispensable fragments to power-transmission setups [1]. Most of the problems that arouse in them were associated with the weakness and defects of the insulation materials. About fifty percent of transformer failure's costs are initiated by dielectric, insulation and oil-associated faults [2]. The necessity for superior dielectrics and transformer oils for insulation is undisputable. For liquid-filter transformers, the insulating fluid plays a vital role by offering electrical insulation and transferring thermal losses to the cooling system. Insulating fluid in transformer must warrant the transfer of heat, which is achieved by thermal conductivity and convection [3]. Three types of insulating fluids are currently in use; namely, mineral oils, synthetic oils and natural esters [4]. The usage of each fluid type is

Corresponding Author: Olatunde A. Oyelaran **Email**: ajanioyelaran@gmail.com

stimulated by the area of application. In spite of the rising call for the utilization of environment-friendly materials, more researches are ongoing on developing especially natural esters for use as insulating fluids in power transformers.

Mineral oils produced from crude petroleum are the most utilized insulating and cooling fluids in electrical transformers. These oils are considered as flammable and since they are petroleum products, they cause harmful effects to the environment, particularly when there are incidents such as transformer explosions when operational, which might cause a spillage of oil to the soil or water stream. A good insulating oil must satisfy the following minimum requirements: being biodegradable, non-toxic, recyclable, thermally stable, readily disposable and not be listed as a hazardous fluid [5]. Mineral oils are acknowledged as possessing low biodegradability with high vulnerability to fire. These factors motivated many researchers to strive for alternative sources of transformer-insulating oils. According to many researches, vegetable oil is considered to be the most potential source to replace mineral oil. The merit of using vegetable oil, also called natural ester, is its non-toxic properties. The only products formed during the biodegradation process are water and carbon dioxide. Esters are also less flammable with about 300°C as minimum flash point. Banumathi and Chandrasekar [6] wrote that paper absorption of water in natural ester oils is significantly lower when compared with mineral oils. Natural ester oil also showed a better performance compared to mineral oil after accelerated aging test, which permits it to prolong the life time of natural ester than mineral oil immersed in the transformer [7, 8].

Papaya fruit is an edible fruit which is also used for the manufacture of cosmetics. Papaya fruit is a fruit available throughout the year with only a little fraction used as seed crop, leaving the rest to rot away as waste. Patel and Nayak [9] wrote that papaya fruit seeds are thrown away as a bad practice. Humans or animals consume about 15% of the fruit and the oil content in the seeds is about 30.7% [10]. Compared with 19.63% for soybean oil and 22.23% for sunflower seeds oil, papaya has a great prospect if developed as feedstock for bio-transformer production. Papaya is currently cultivated in Hawaii, Florida, Eastern British Africa, Sri-Lanka, South Africa, India, Malaysia, the Canary Islands and Australia. It is now present in every tropical and sub-tropical country of the world. Since the usage of papaya seed oil for cooking is not visible as a result of benzyl isothiocyanate carcinogenic compounds, its availability as an uneatable oil is an advantage, being not in competition with food. Insulating oil in transformers, undergoes temperature variations owing to the fluctuating nature of electricity consumption. Vegetable oil that will be used as a transformer oil should be capable of bearing the maximum tolerance level of temperature variation of 110℃ at the transformer windings [5], devoid of losing its dielectric properties for use in high-voltage transformers. To validate the appropriateness of using papaya oil as an insulating fluid, it is imperative to compare the dielectric properties of papaya oil with those of the frequently used insulating liquids that are mineral oils. This paper compares the dielectric properties of papaya oil with those of mineral oils, under temperature variation ranging from room temperature, 25℃ up to 100℃ or 120℃.

Material and Methods

Experimental Procedure

Papaya fruits were obtained from Ogbomoso, Nigeria. The fruits were cut into two halves and the seeds were removed, dried in an oven at 60ºC for 24 hours, ground into powder and the oil was extracted using the soxhlet extraction method with n-hexane as a solvent. A modified Dijkstra and Opstal purification method used by Abdelmalik et al., [11] and Oyelaran et al, [12] was adopted for the purification of the oil to obtain the refined papaya seed oil. An amount of 200 ml of papaya seed oil (PSO) was heated in a 500 ml conical flask to 70°C and 8 volume % of 64 volume % aqueous citric acid solution was gently added and mixed vigorously for 15 minutes with a magnetic stirrer. An amount of 4 ml of 8 volume % NaOH solution was gently added and stirred at 400 rpm for 15 min. The mixture was then dried for 30 minutes in a vacuum oven at 85°C to reduce the water content. To the mixture, an amount of 2 g of silica gel was added at 70°C and stirred at 300 rpm for 30 minutes to avert settling. Fuller's earth was again added and stirred continuously for 30 min at 8 wt %. The sample was then filtered in a vacuum oven at 85°C with filter paper.

Degumming Process

The degumming process was carried out using the method of Sutapa et al, [13] by adding 20% phosphoric acid at 0.5% (w/w) of oil. After heating for 15 minutes at 80 ºC, the oil was then separated from the phosphatide compound and washed with warm distilled water and the oil was then dried with a vacuum dryer to obtain purified papaya seed oil (PPSO).

Characterization of PPSO

Some of the physicochemical properties of PPSO were determined using methods described by the American Society for Testing and Materials. Properties, such as kinematic viscosity, flash and fire points and cloud point of PPSO, were ascertained following ASTM D445 and ASTM D93 standards, respectively.

Flash Point and Fire Point

Pensky-Martens closed-cup tester was used to measure the flash point in accordance to ASTM D 93 standard [14]. The brass test cup fitted with lid was filled with 50ml of the sample. The container with the sample was heated under stirring at specified rates with flame test carried out at regular intervals until a flash spreading inside the cup was realized for a second. The resultant temperature at which the flash spreads throughout the cup is the flash point of the sample. The fire point on the other hand is the temperature at which the flash is sustained for more than five seconds after ignition by open flame.

Viscosity Determination

Brookfield viscometer with the appropriate spindle was used to measure the viscosity of the liquid sample in accordance with ASTM D445 [15]. Viscosity aids in the heat-convection process in the transformer. The lesser the value of viscosity, the greater the heat-transfer rate in the transformer [12].

Breakdown Voltage

The measure of an insulating fluid capability of withstanding electric stress without failure is known as dielectric breakdown voltage. It is also an indication of the presence of contaminating agents, such as air bubbles, water, cellulosic fibers, dirt or conducting particles in the fluid. The IEC 60156 standard was used to measure the breakdown voltage with a kit voltage capacity of 60 kV. The experiment was carried out with spherical head electrodes of standard diameters and a gap of 2.5 mm between them. An amount of 500ml of the sample oil was filled up to 40mm level above the electrodes. Bubbles in the container were allowed to settle about 5 – 15 minutes after filling of the sample before increasing the test voltage at a rate of 2 kV/s. Application of voltage was started at least 5 minutes after pouring the mineral-oil sample into the test chamber [16] and about 15 minutes for papaya oil [5]. The delay time is required to guarantee that gas bubbles which formed during the pouring process have been expelled completely before the commencement of measurements. The measurements were performed six times with a time delay between two successive measurements of at least 2 minutes for mineral oil [16] and 6 minutes for papaya oil. The delay time after measurement was also carried out to allow breakdown of products to disperse and gas to expel, before succeeding measurement was conducted so that the later measurement was not influenced by the previous one [17]. The longer delay time for papaya oil was due to the higher viscosity of the oil than that of mineral oil.

In order to study the temperature effect on the breakdown voltage of oils, measurement was carried out at different temperatures. The temperature was raised up to 120℃ with 10℃ increment. The temperature was kept relatively constant using temperature sensors embedded on the oil chamber's wall, heater, blower, controller and contactor as a temperature-control system. The temperature of the liquid is detected by the temperature sensor. Upon receiving information sent by the temperature sensor, the controller commands the contactor to connect or disconnect the electric heater from the power supply. The blower helps reduce the temperature when the temperature is higher than required.

Dielectric Constant and Dissipation Factor Measurements

The IEC 60247 standard [18] with Schering circuit test and null indicator oscilloscope was used to measure the dielectric constant and dissipation factor of oils, as schematically shown in Fig. 1. The *Schering* circuit balance is shown by the presence of Lissajous curve as a straight-line display on null indicator. The oil sample from Tettex Instruments was poured into the test cell. The test cell is a three-terminal test cell that forms a capacitance system with liquids or gases

as dielectrics. To monitor the temperature, the test cell has an electric heater and a thermometer with it. Since the test cup is made of stainless steel, the mass of the test cell is relatively higher than that of the oil sample; hence, the temperature was varied in reverse order. After heating the oil to 100°C, the temperature of oil was allowed to decrease to each temperature level. After a reduction of 10°C, the capacitance and dissipation factor of oil were then measured.

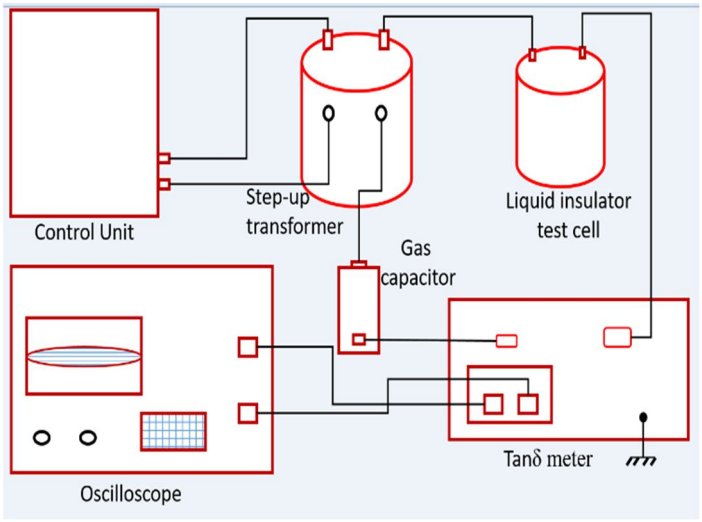

FIG. 1. Schematic diagram of dielectric constant and dissipation factor measurements.

Results and Discussion

Kinetic viscosity	3.57	mm^2/s	ASTM D445
Flash point	389	K	ASTM D93

Breakdown Voltage

Breakdown voltage of all tested oils was measured at 25℃ up to 120℃ with six measurements carried out at each temperature level. The mean values of the measurements are shown in Fig. 2. The breakdown value significantly increases with temperature rise up to 70℃. This is a result of the relative decrease in water content of oils. It is a known fact that the breakdown voltage of all insulating fluids is inversely proportional to their relative water content [19, 5]. The ratio between absolute water content (wt_{abs}) and water solubility (wt_l) of oil is the relative water content (wt_r) of oil, which is mathematically expressed by Eq. (1). The water solubility in oil on the other hand increases with temperature, as established in Eq. (2).

$$wt_r = \frac{wt_{abs}}{wt_l} \times 100\% \quad (1)$$

$$wt_l = wt_0 \exp\left(\frac{-H}{T}\right) \quad (2)$$

where, wt_0 and H are the oil parameters. The values of wt_0 and H for papaya oil and mineral oil are 2.61 x 10^5 and 1340 and 19.2 x 10^6 and 3805, respectively [18, 5]. The graphical relationship between water solubility and absolute temperature of papaya oil and mineral oil is shown in Fig. 3.

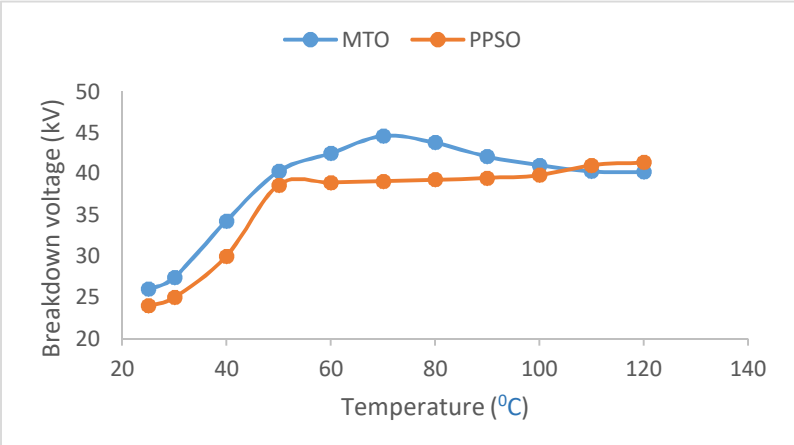

FIG. 2. The mean values of breakdown voltage of papaya oil and mineral oil as functions of temperature.

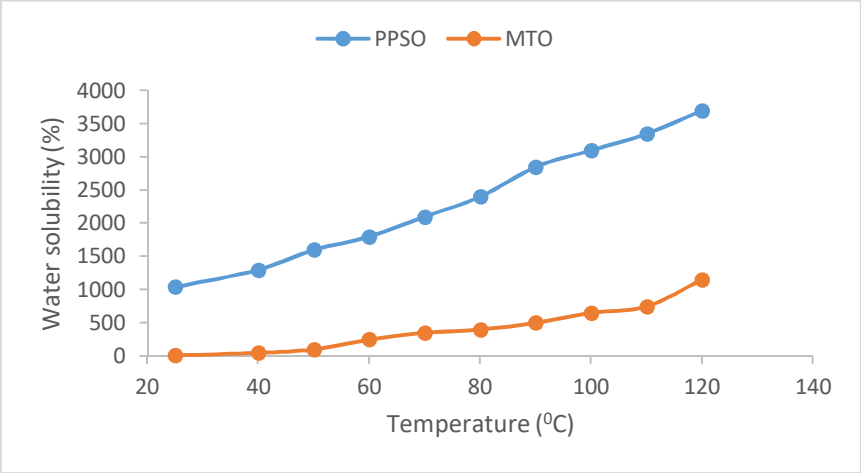

FIG. 3. Water solubility of papaya and mineral oils as a function of temperature.

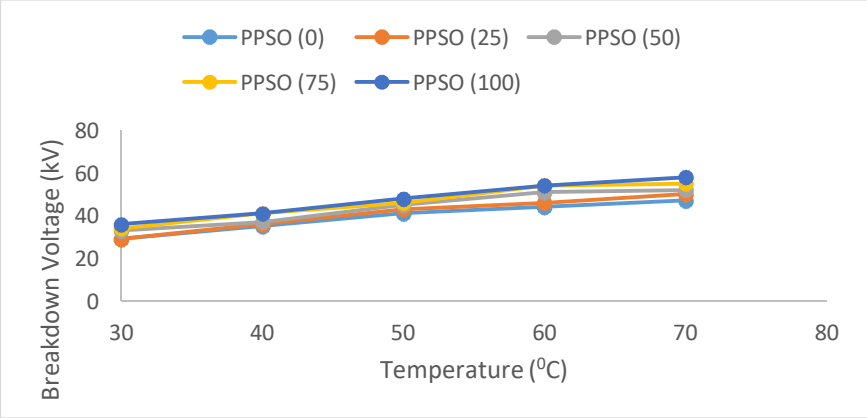

FIG. 4. Breakdown voltages of a mixture of papaya and mineral oils as a function of temperature.

Increasing the temperature causes a substantial reduction in the relative water content of the oil, resulting in raising the breakdown voltage of the oil. A similar trend was reported by Suwarno and Irawan [19] and Rajab et al. [5], who performed breakdown voltage measurements on a mixture of papaya and mineral oils under temperature variation, ranging from 30 to 70℃, as displaced in Fig. 4.

The existence of water in oil affects the breakdown voltage of oil in two ways; by forming water clusters and being absorbed by particles making them conductive particles [20]. As temperature increased, water in the form of water clusters in oil reduced due to increase in temperature, triggering a slow breakdown voltage increase in the oil. This was clearly revealed by papaya oil at temperatures up to about 50℃ and about 40℃ for mineral oil, as seen in Fig. 2. The relative water contents of papaya and mineral oils under temperature variation range of 25 to 120℃ are shown in Fig. 5. Additional rise in temperature resulted in water being absorbed by particles to reduce the substantial rise in the breakdown voltage of the oil. Between 50 and 70℃, papaya oil experienced changes, while mineral oil experienced changes between 40 and 70℃. However, breakdown voltage of dry liquid is relatively unaffected by temperature variation [5]. This was experimentally shown by mineral oil, as displayed in Fig. 2, which is relatively unaffected in the temperature range between 70 and 90℃. However, this happens for dry liquid at a temperature a little below the boiling point. Here, breakdown voltage of dry liquid begins to go down as a result of the formation and growth of vapor bubbles [5]. From Fig. 2, it can be seen that mineral oil experienced this stage, where its breakdown voltage begins to fall at 100℃. Owing to the higher boiling point of papaya oil, the oils need to be heated further to achieve this condition.

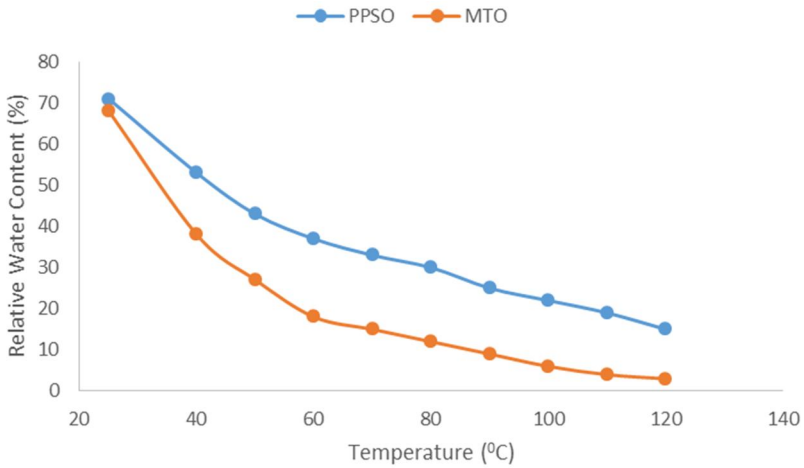

FIG. 5. Relative water content of papaya and mineral oils as a function of temperature.

From the results obtained, mineral oil is better for temperatures up to 100℃ from the breakdown voltage point of view. However, using PPSO appears to enable improving allowable temperature as its breakdown voltage appears to constantly rise up to the temperature of 120℃. At this point, breakdown voltage of papaya oil is higher than that of mineral oil. From the breakdown voltage trend of the tested oils, one can assume that beyond 120℃, the breakdown voltage of papaya oil will be considerably higher than that of mineral oil. However, the assumption cannot be proved experimentally now, as a result of the oil chamber design limitations.

Dielectric Constant

The dielectric constant of oil is the ratio of capacitance of oil-filled test cell to that of empty cell, as shown mathematically by Eq. (3) [19]. The results at different temperatures in the range of 25 up to 100℃ are shown in Fig. 5.

$$\varepsilon_r = \frac{C_x}{C_0} \tag{3}$$

where, $\boldsymbol{\varepsilon_r}$ is the dielectric constant of tested oil, C_x is the capacitance of the oil-filled test cell, and C_0 is the capacitance of empty cell. In this experiment, we take C_0 = 1.974 x 37.92 pF.

From Fig. 6, it can be seen that the variation of the dielectric constant of papaya and mineral oils due to temperature change is the same. The dielectric constant of papaya oil slightly decreased from 3.25 at 25℃ to 3.10 at 100℃, while the dielectric constant of mineral oil decreases from 2.35 to 2.22 for the same temperature range.

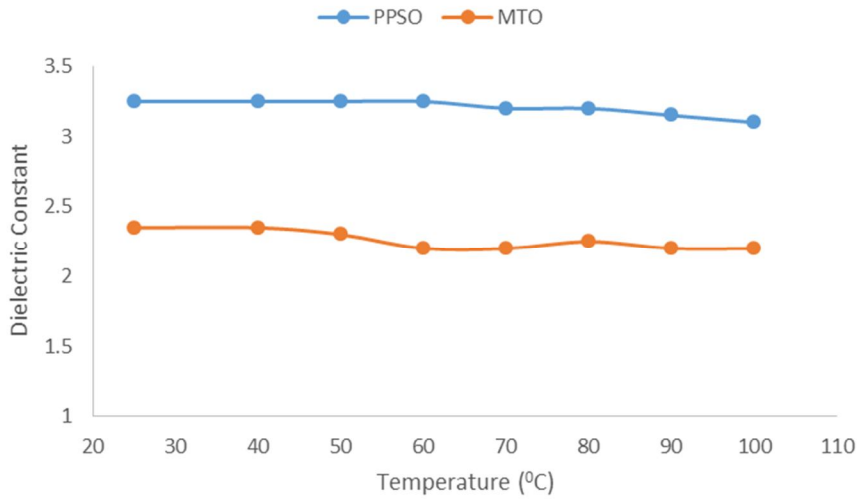

FIG. 6. Dielectric constants of papaya and mineral oils as functions of temperature.

The dielectric constant of any dielectric material refers to its susceptibility (Eq. 4), which is a measure of how easily a dielectric polarizes in reaction to an electric field, as shown mathematically in Eq. 5. Likewise, permittivity

is proportional to polarization as susceptibility [21].

$$\varepsilon_r = \chi + 1 \quad (4)$$

$$P = \chi\, \varepsilon_0 \mathrm{E} \quad (5)$$

where ε_r is the dielectric constant, χ is the susceptibility, P is the polarization and E is the electric field.

When an electric field is applied to a dielectric material, dipoles inside the material that are originally random are directed in the same direction of the applied electric field. Increasing the thermal agitation owing to the temperature increase will make it more difficult for the dipoles to orient [22]. The difficulty of polarization shows the decreases of permittivity and susceptibility based on Eq. 5 for a constant magnitude of electric field. Hence, we can agree that the dielectric constants of tested oils decreased slightly with the increase in temperature.

At the same temperature, papaya oil has a higher dielectric constant than mineral oil. This experimental proof shows a correlation between susceptibility, degree of polarity of the oil and its dielectric constant. Note that the degree of polarity of a fluid is determined by the vector summation of all bond moments comprising the molecule of the fluid; hence, the higher the unbalance level of geometrical chemical structure of the molecule, the higher its degree of polarity. It is easier for papaya-oil molecules to form dipoles compared to mineral oil as a result of its highest degree of unbalance, leading to the highest degree of polarity; hence, it is easier for papaya oil molecules to form dipoles compared to mineral oil molecules. Therefore, papaya oil is more susceptible to polarize under the effect of an electric field, making its dielectric constant higher than that of mineral oil.

The higher value of papaya oil dielectric constant is a merit for a better uniform electric field. When two dielectric materials are connected in series, the electric field is inversely proportional to their dielectric constants. The dependence of electric field E on the dielectric constants ($\varepsilon_1$and ε_2) of two dielectrics connected in series is expressed by Eqs. 6 and 7.

$$\boldsymbol{E_1} = \frac{V}{\varepsilon_1 \left(\frac{d_1}{\varepsilon_1} + \frac{d_2}{\varepsilon_2}\right)} \quad (6)$$

$$\boldsymbol{E_2} = \frac{V}{\varepsilon_2 \left(\frac{d_1}{\varepsilon_1} + \frac{d_2}{\varepsilon_2}\right)} \quad (7)$$

where, V is the applied voltage, while d_1 and d_2 are the thickness of dielectric 1 and dielectric 2, respectively.

Dissipation Factor (Tan δ)

Fig. 7 shows the results of dissipation factor of papaya and mineral oils. From the results obtained, all oils show a similar trend of dissipation factor with temperature variation. From 25 to 100℃, there is an increase in the dissipation factor of all oils. For papaya oil, the increase is from 0.013 to 0.033 and for mineral oil, the dissipation factor changes from 0.025 to 0.035. Dissipation factor (tan δ) refers to the dielectric losses owing to an AC electric field application. Electric conductivity in insulating liquids denotes a substantial part of their dielectric losses, besides the hysteresis losses owing to the polarization of oil molecules. Dissipation factor (tan δ) is proportional to electric conductivity, as shown in Eq. 8.

$$\tan\delta = \frac{\sigma}{\omega\varepsilon} \quad (8)$$

where σ is the electric conductivity, ω is the angular frequency,and ε is the permittivity of oil. The change in dissipation factor due to temperature variation will depend on the change of the electric conductivity when the angular frequency and permittivity of oil and test cell system are considered constants.

The electric conductivity considerably increases with increasing temperature due to decreasing oil viscosity and increasing dissociation of oil molecules. The electric conductivity of oil owing to the oil molecule dissociation is mathematically expressed in Eqs. 9, 10 and 11, as shown below [23]:

$$\sigma = ne(\mu_+ + \mu_-) \quad (9)$$

where σ is the electric conductivity, n is the number of dissociated molecules per unit volume, e is the electronic charge and μ is the ion mobility (subscripts + and – indicate the positive and negative charges). The number of dissociated molecules increase exponentially with temperature as expressed by Eq.10.

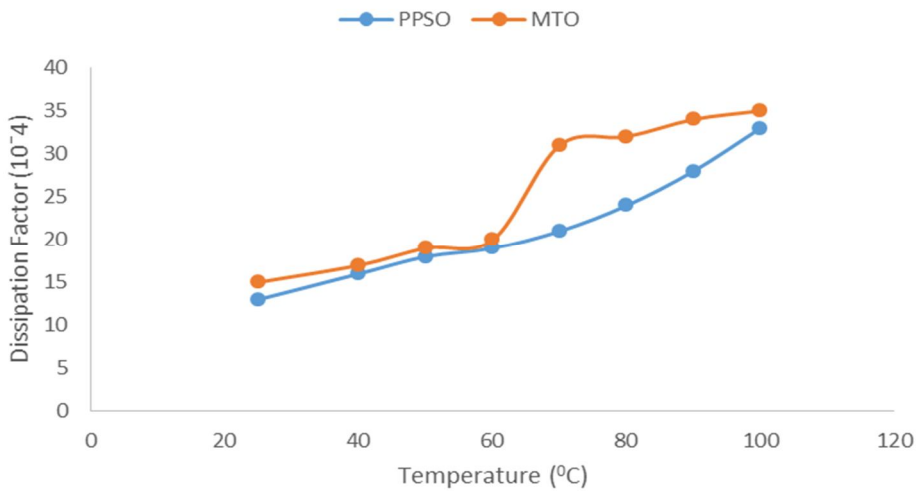

FIG. 7. Dissipation factor (tan δ) of papaya and mineral oils as functions of temperature.

$$n = Nex\left(\frac{-W}{kT}\right) \quad (10)$$

where N is the number of molecules per unit volume of oil, W is the dissociation energy, k is the Boltzmann's content and T is the temperature. Therefore, temperature dependent of electric conductivity might be mathematically expressed as in Eq. 11.

$$\sigma = e(\mu_+ + \mu_-)\, Nexp\left(\frac{-W}{kT}\right). \quad (11)$$

Furthermore, established on Eq. 12, the decrease in viscosity also has an impact on the increase of electric conductivity of the oil:

$$\sigma = \frac{2ZC_0}{a<R>\eta} \quad (12)$$

where σ is the electric conductivity, Z the ionic valance, usually set to unity, α is a constant with reasonable value of 4π, <R> is the size of charged molecule and η is the viscosity. As a result, decreasing viscosity with the increase of temperature is shown mathematically in Eq. 13.

$$\eta = Aex\left(\frac{-B}{T - T_0}\right). \quad (13)$$

When A and B are constants, the change of electric conductivity due to the viscosity variation mechanism can be mathematically expressed in Eq. 14. [24].

$$\sigma = \frac{2ZC_0}{a<R>\eta} exp\left(\frac{-B}{T - T_0}\right). \quad (14)$$

If all variables are constants and only electric conductivity of a liquid is variable only with temperature (where T_0 = 273°C), then Eqs. 11 and 14 can be expressed in a modified form as Eqs. 15 and 16, respectively. By changing the constants' values of K1 and K2 with the combination of 100-100, 100-50, 50-100 and 50-50, the theoretical graphs of the electric conductivity of the liquid as shown in Fig. 8 and Fig. 9 can be developed.

$$\sigma = K_1 \exp\left(\frac{-K_2}{T}\right) \quad (15)$$

$$\sigma = K_1 \exp\left(\frac{-K_2}{T - T_0}\right). \quad (16)$$

From the theoretical graphs of the electric conductivity as a function of temperature shown in Fig. 8 and Fig. 9, it can be seen that the variation of curve shape is determined by the values of K1 and K2. Choosing the 100-100 (blue color) or 50-100 (green color) as the values for K1-K2, it can be expected to get similarity between the theoretical graphs of electric conductivity and the experimental results for papaya and mineral oils. Over all the testing temperature range, the dissipation factor of papaya oil is lower than that of mineral oil. This is an advantage as the papaya oil possesses the lowest dielectric losses. Fig. 8 and Fig. 9 show the theoretical graphs of electric conductivity of PPSO as functions of temperature based on Eq. 10 and Eq. 11, respectively, taking all variables as being constant except temperature.

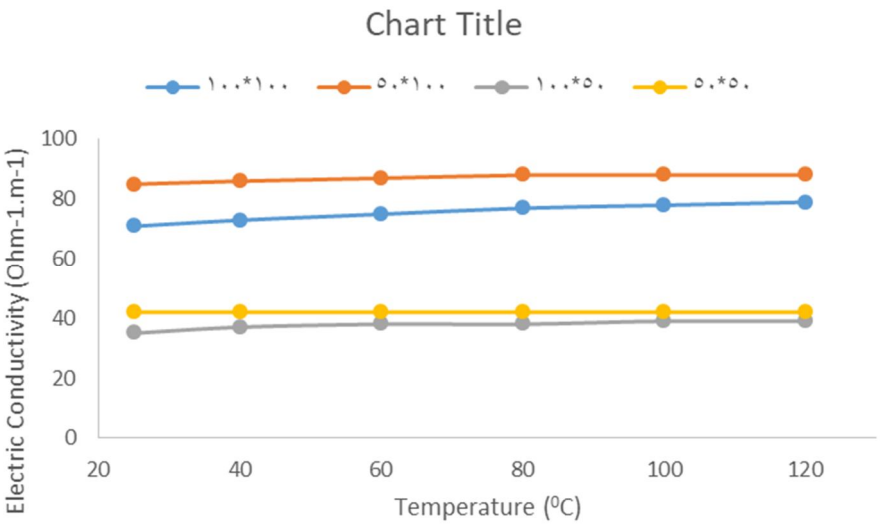

FIG. 8. Theoretical graphs of electric conductivity of insulating liquid as a function of temperature based on Eq. 10, taking all variables as being constant except temperature.

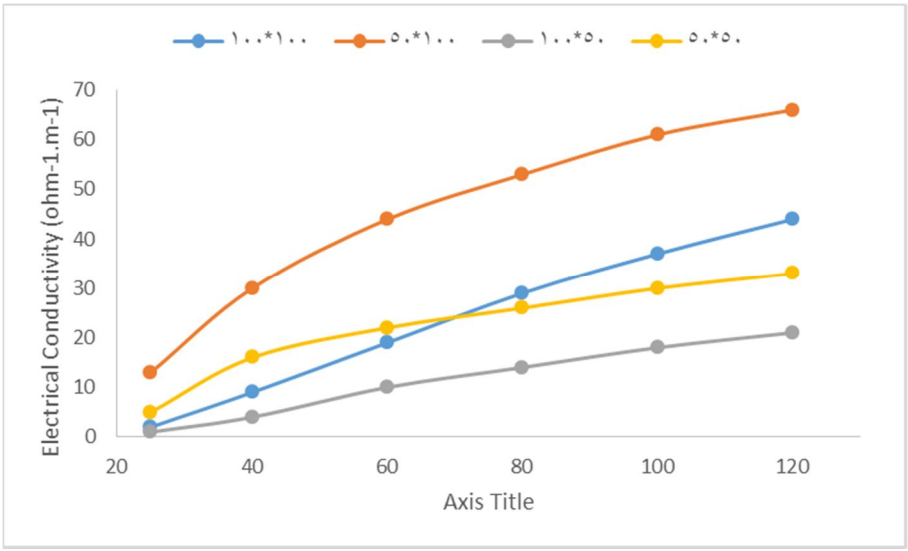

FIG. 9. Theoretical graphs of electric conductivity of insulating liquid as a function of temperature based on Equation 11, taking all variables as being constant except temperature.

Conclusions

Dielectric characteristics of papaya oil and mineral oil have been investigated and compared under temperature variation. The results reveal that both oils have the same variation tendency of dielectric properties under temperature change. Mineral oil possesses better breakdown voltage properties for temperatures up to 100°C. However, the use of papaya oil appears to boost permissible temperature loading of transformers, as the papaya oil breakdown voltage tends to increase continuously up to 120°C, while that of mineral oil starts to fall at 100°C, becoming lower than that of papaya oil at 120°C. For the same temperature level, papaya oil possesses the higher dielectric constant than mineral oil at the same temperature. This is a benefit, since papaya oil will be experiencing lower electric field stress if used as an impregnation to paper insulation for transformer applications. Papaya oil possesses the lowest dielectric losses, since it possesses lower dissipation factor than mineral oil over all temperatures tested. As seen in this research, the low breakdown voltage of papaya oil at low temperatures was due to the high content of water in it. Hence, reducing water content to the barest minimum is a future task.

References

[1] Zhang, J., Wang, F., Li, J., Ran, H., Li, X. and Fu, Q., Energies, 10 (2017) 1411.

[2] Tanteh, D.N., Al-Liddawl, S.Y. and Ssekasiko, D., "Properties of Transformer Oil That Affect Efficiency", (Department of Electrical Engineering, Bleking Institute of Technology, 2014).

[3] Paris, P.M., "Silicone oils for transformers" (in French), E.O.F. Bulletin des e'tudesetrechesche-series B, (Reseanxelec-frigues, Materials Electrigues, N., 1987), pp. 5-13.

[4] Darwin, A. and Follist, C.P., "The Use of Natural Ester Fluids in Transformers", (Mat past Avera T. and N., UK, 2007).

[5] Rajab, A., Sulaeman, A., Sudirham, S. and Suwarno, I.T.B., J. Eng. Sci., 43 (3) (2011) 191.

[6] Banumathi, S. and Chandrasekar, S., Journal of Advances in Chemistry, 12 (16) (2016) 4902.

[7] McShane, C.P., "Vegetable Oil-based Dielectric Coolants", (IEEE Industry Applications Magazine, May/June, 2002).

[8] McShane, C.P., Proceedings of IEEE/PES Transmission & Distribution Conference & Exposition, Atlanta GA, Oct. 28 - Nov. 02, (2001).

[9] Patel, K.A. and Nayak, M.G., International Journal of Advance Engineering and Research Development, 4 (1) (2017) 2348.

[10] Wong, C.S. and Othman, R., International Journal of Engineering and Technology, 6 (6) (2015) 2773.

[11] Abdelmalik, A.A., Abolaji, P.A. and Sadiq, H.A., Journal of Physical Science, 29 (1) (2018) 1.

[12] Oyelaran, O.A., Bolaji, B.O. and Samuel, O.D., Journal of Chemical Technology and Metallurgy, 55 (2) (2020) 307.

[13] Sutapa, I.W., Bandjar, A., Latupeirissa, J. and Toesik, M.M.A.F., Journal of Physics: Conf. Series, 1463 (2020) 012010.

[14] ASTM D93, "Standard Test Methods for Flash Point by Pensky-Martens Closed-cup Tester", (2012).

[15] ASTM D 445, "Standard Method of Test for Viscosity of Transparent and Opaque Liquids (Kinematic and Dynamic Viscosities)", (2021).

[16] EC-156 International Standard, "Insulating Liquids – Determination of the Breakdown Voltage at Power Frequency – Test Method", Second Edition, (1995).

[17] Cooper Power System, "Envirotemp FR3 Fluid Testing Guide", Section R- 900-20-12, July, (2004).

[18] IEC-60247 International Standard, "Insulating Liquids – Measurement of Relative Permittivity, Dielectric Dissipation Factor (tan δ) and D.C. Resistivity", Third Edition, (2004).

[19] Suwarno and Darma, I.S., Journal of WSEAS Transactions on Power Systems, 3 (2) (2008) 37.

[20] Yeckel, C., Curry, R.D. and Norgard, P., Journal of IEEE Transactions on Dielectrics and Electrical Insulation, 14 (4) (2007) 820.

[21] Hayt, W.H.Jr. and Buck, J.A., "Engineering Electromagnetics", (McGraw-Hill, 1989).

[22] Roju, G.G., "Dielectrics in Electric Field", (Marcell Dekker, Inc., 2003).

Volume 15, Number 4, 2022. pp. 353-360

Jordan Journal of Physics

ARTICLE

Natural Radioactivity Levels in Healthy and Groundwater Samples of Al-Manathera Region of Al-Najaf, Iraq

Ali A. Abojassim[a], **Qusay B. Muhamad**[b], **Noor Ali Jafer**[c], and **Hassan A. Mohammed**[b]

[a] *Department of Physics, Faculty of Science, University of Kufa, Al-Najaf, Iraq.*
[b] *Department of Physics, Directorate of Education Najaf, Al- Najaf, Iraq.*
[c] *Radiology Techniques Department, College of Medical Technology, The Islamic University, Najaf, Iraq.*

Doi: **https://doi.org/10.47011/15.4.3**

Received on: 05/11/2020; *Accepted on: 01/03/2021*

Abstract: In this study, the specific activity of the radionuclides 238U, 232Th and 40K was determined in groundwater samples and potable water in Al-Manathera, Al-Najaf governorate, Iraq. The study was carried out using an NaI(TI) scintillation detector of gamma spectroscopy of "3×3" dimensions. The concentrations in Bq/l of 238U, 232Th and 40K have average values of 8.3±1.2, 1.9±0.4 and 57.4±5.7 for the groundwater and 0.6±0.10, 0.07±0.02 and 2.7±0.50 for the potable water. At the same time, another effective dose of ingested water (EDIW) was also calculated in three age groups for the current study. These groups of age include infants (≤ 1 y), children (2 – 17y) and adults (> 17y). As for the comparison with global standards and international limits by WHO2011, ICRP 1991 and WHO 2000, we found that the calculated values for groundwater were over the standardized global limits, but those for potable water were within those limits. This is to say that the EDIW, in addition to the activity concentrations that are within the international limits, were set by the previously mentioned organizations and can be safely consumed. Their consumptions, however, do not pose a threat or a biohazard to their respective cities. On the other hand, consuming groundwater can negatively affect the city's population where the study was conducted.

Keywords: Radionuclide, Effective dose, Drinking water, Al-Manathera.

1. Introduction

Humans can be exposed to any ionizing radiation from all sorts of sources throughout the lifetime, whether they are natural or artificial. Therefore, gaining further knowledge about the general levels and distribution of radionuclides and radiations is essential to measuring the impact of these radiations on living beings. Such radiations can also be of terrestrial or extraterrestrial sources. Of these two mentioned sources of radiation, terrestrial sources constitute the main source of radiation to which the human body is exposed. Such sources of radiation may include cosmic gamma rays, gamma ray emitted from soil particles, building materials, water and even air itself [1]. One of the sources of this radioactivity is the radionuclides, which, with their habit of emitting radiation for thousands of years, represent a daily-life experience for humans. Gamma rays as well as alpha and beta particles are some of the most common radiations that are considered ionizing. Radiations, however, can also be emitted from sources made by mankind. Some of the characteristics of these radiations were applied for different purposes, such as medicine, biology, industry, agriculture, as well as generating electric power. This resulted in the fact that such man-made utilization of radioactivity was the reason for that humans can be exposed to higher rates of radioactivity that is

Corresponding Author: Ali Abid Abojassim **Email**: ali.alhameedawi@uokufa.edu.iq

emitted from different sources in the surrounding environment. However, not all of the human populations around the world are exposed to equal amounts of radioactivity. For instance, patients who are treated with medical irradiation or members of staff who work in nuclear industries may receive higher radiation exposure levels than members of general public [2]. NORM, Naturally Occurring Radioactive Materials, are simply part of our soil on earth. Majorly Radium and Radon, the highest amount of radionuclides in NORM are a result of the decay both Uranium and Thorium naturally have. Exposure to radionuclides from Radon can be higher due to the increasing domesticated and industrial activities in the human life that include the burning of fossil fuel, mineral extraction and the application of fertilizers. Industrial practices involving natural resources often concentrate radionuclides to a degree that may pose a risk to humans and the environment [3]. The most essential and valuable natural source is water, which is supposed to be free of pollutants. It cannot be stressed enough that measuring the naturally emitted radioactivity can be a crucial element in deducing an accurate assessment of the amount of radiation to which people are exposed. The appearance of natural radionuclides in water originates from human activities within the area, such as fertilizers used in agriculture, where water is found [4]. Since the population, especially in Al-Najaf city of Iraq, depend on the Euphrates river in consuming water which originates from Turkey, it's far feasible to have reached radioactive forcing into waterways and eventually to the people. So, it became necessary to accurately ingest the correct amount of water into the machine to be measured by gamma-ray spectroscopy. The related dangers of contaminated drinking water have been expected in steps with their human nature and dwelling standard. As for the ingestion of radionuclides applicable to nuclear emergencies, it is the most important participant to have committed internal doses and consequently long-term health effects. Therefore, it became essential to generate a final analysis of Uranium radionuclide ingestion statistics in consuming water. Many studies have been performed to investigate and measure radioactive elements' concentrations in water samples using different techniques [5-8]. The present study aims to measure natural radioactivity, such as Uranium-238, Thorium-232 and Potassium-40 in healthy and groundwater samples located in Al-Manathera regions in Al-Najaf, Iraq, using gamma-ray spectroscopy with NaI(Tl) detector. In this study, we calculate EDIW due to natural radioactivity in samples under study to warn people of the danger of this pollution in order to use special tools to work during the access to this area to reduce the risk of harmful diseases.

2. Area of Study

About 100 miles to the south of Baghdad, Iraq's capital, lay Al-Najaf province at 19 degrees and 44 minutes longitude, 31 degrees and 59 minutes latitude and 70 meters above sea level [9]. Al-Najaf province has four constituents: Najaf, Kufa, Al-Meshkhab and Al-Manathera, which are the province districts in Al-Najaf. The centre of Al-Najaf consists of a number of residency quarters, such as Al-Zahraa, Al-Askari, Al Shuhadaa, Al-Jamyia, Al-Jumhury, Quirink and others. Two suburbs are officially run by Al Manathera district; these are Al-Hera and Al-Qadissia suburbs. As for the study in hand, the studied water samples were taken from Al-Manathera, as illustrated in Fig. 1.

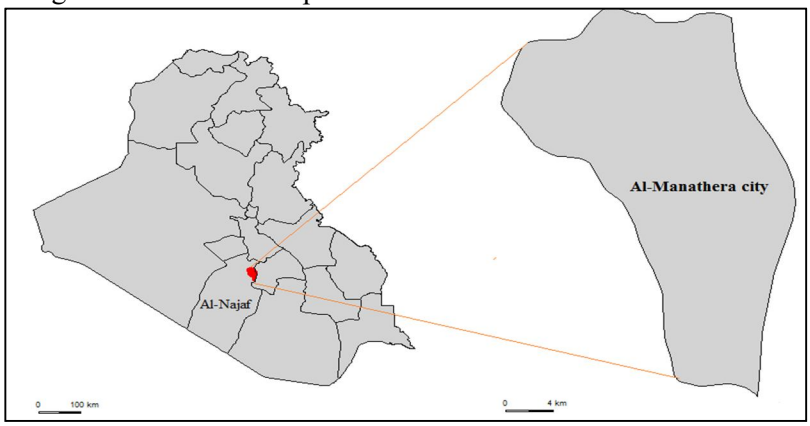

FIG. 1. Area of study.

3. Materials and Methods

3.1 Sampling and Sample Preparation

In the meantime, about ten (10) wells are still used that are over 20 m in depth in Al-Manathera, which are also possible to be utilized to supply the area with drinking water. Ten (10) other locations are also used to produce industrial drinking water. In order to conduct the study, during the summer of 2019, a total of 20 water samples were carefully collected from 20 collection locations in the municipality of Al-Manathera. These locations included groundwater and healthy-water samples, at a rate of 10 samples each, as displayed in Tables 1 and 2.

TABLE 1. Locations and coordinates of groundwater.

Location name	Sample code	Coordinate	
		N	E
Jawad Farm well	G1	31.922391°	44.460966°
Mohammed Farm well	G2	31.928780°	44.460975°
Town Hall Street Farm well	G3	31.930566°	44.461216°
Hameed Farm well	G4	31.921119°	44.458167°
Town Hall Garage Farm well	G5	31.901565°	44.469009°
Fadhil Street Farm well	G6	31.896874°	44.453000°
Mahmoud Street Farm well	G7	31.905357°	44.465250°
Jawad Shiltagh Farm well	G8	31.913906°	44.460501°
Jabour Farm well 1	G9	31.910876°	44.450022°
Jabour Farm well 2	G10	31.903201°	44.450114°

TABLE 2. Locations and coordinates of industry-product healthy drinking water.

Industry name	Sample code	Coordinate	
		N	E
Ahmed Ali Factory	H1	31.910922°	44.469668°
Karar Ibrahim Factory	H2	31.902272°	44.461886°
Said Salim Factory	H3	31.895500°	44.497645°
Hassein Factory	H4	31.899110°	44.485500°
Al-Manathera Factory 1	H5	31.923050°	44.477651°
Al-Manathera Factory 2	H6	31.896070°	44.489810°
Al Jamiya Factory	H7	31.895701°	44.490058°
Al Burkat Factory	H8	31.902812°	44.475007°
Al Askari Factory 1	H9	31.891997°	44.499003°
Al Askari Factory 2	H10	31.894814°	44.490025°

Using polyethelene containers, the collected samples were approximately 5 litres of water. In order to maintain the elements in water from going missing or being deficient, nitric acid was used in the method of sampling that was adopted in this research [10, 11]. Through the process of evaporation, water samples were processed accordingly. Using washed 1 litre of Marinelli beaker that was previously rinsed with dilute sulphuric acid and dried up in order not to contaminate it, they were loaded with a certain amount of random water samples, then sealed firmly. Then, the samples were put on the shelf in order to establish secular equilibrium between ^{226}Ra and ^{238}U with their results and in order to allow the equilibrium of ^{226}Ra-^{222}Rn prior to analyzing them radiometrically [8].

3.2 Gamma Counting

Gamma counting was conducted at the advanced laboratory of the nuclear department of physics, University of Kufa. The measurements of the natural radioactivity experiments of both healthy and groundwater utilized the spectroscopy system of gamma-ray that uses the scintillation detector of Sodium Iodine. Gamma-ray spectrometer consists of a scintillation detector NaI(Tl) system of (3"×3") crystal dimensions (supplier: Alpha Spectra, Inc.-12I12/3) (see Fig. 2) combined with an analyzer of multi-channels (MCA) (ORTEC -Digi Base) that, through its interface, has 4096 channel-connecting units called ADC (Analog to Digital Converters). Using the PC software

(MAESTRO-32) of the lab, the spectroscopic measurements were carried out as the system is connected to parts of the measurement system. Water samples were shielded environmentally using the cylindrical chamber (ORTEC). The components of this shielding process consist of two separate place segments. The upper part consists of lead with (5 cm) thickness and (20cm) length surrounding the crystal with a cover with (5cm) thickness and a diameter of (22 cm). The detector was placed in the center of the chamber to reduce the effect of the scattered radiation from the shield. The detector has an energy resolution of 8.9 at 661.2 keV gamma energy. In this work, the energy calibrations of the gamma-ray spectra were done using standard radioactive sources of ^{137}Cs, ^{60}Co and ^{152}Eu. Counting was done for 24 hours because of the low natural activities of radionuclides in water. The spectrum was measured and the area under the photo-peaks was computed using the algorithm of the MCA. The prominent photo-peaks observed in the spectra of the samples were identified as those of the radionuclides in the natural decay series of ^{238}U, ^{232}Th and the non-series ^{40}K. Subsequently, the transition lines of 1460 keV of ^{40}K, 1764.5 keV of ^{214}Bi, 2614.7 keV of ^{208}Tl were used to determine the ^{238}U and ^{232}Th, as well as the non-series ^{40}K, respectively [12].

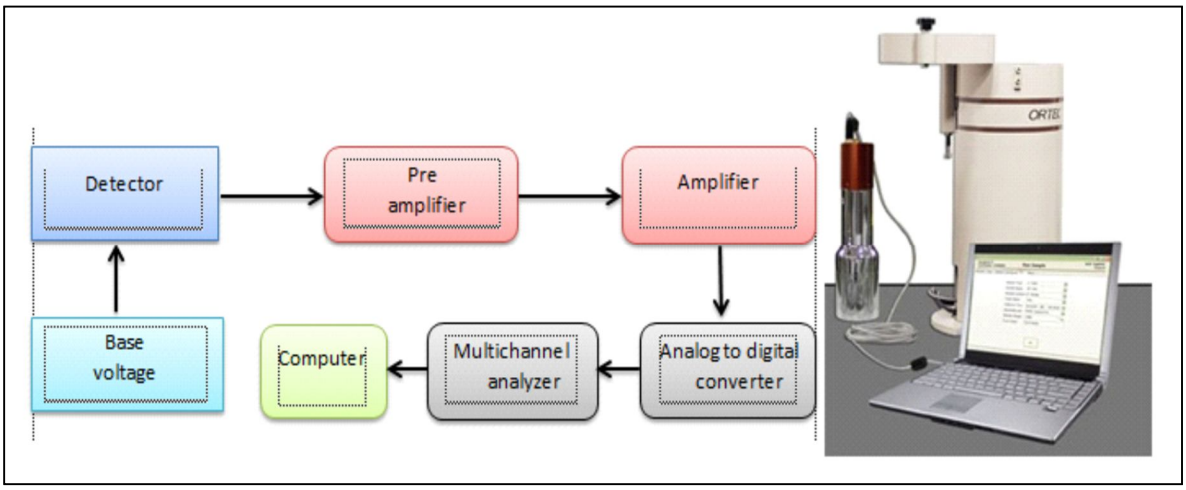

FIG. 2. Diagram of an NaI(Tl) system.

3.3 Concentrations of Activity Effective Dose of Radiation Due to Ingested Water Computation

The concentration C of the radionuclide, in every single sample of water, has been evaluated by the use of the relation [7, 13]:

$$A = \frac{N(E_\gamma)}{\varepsilon(E_\gamma).I_\gamma.V.t_c} \quad (1)$$

where $N(E_\gamma)$ is the net peak area of the radionuclide of interest, $\varepsilon(E_\gamma)$ is the efficiency of the detector for the energy E_γ, I_γ is the intensity per decay for the energy E_γ, V is the volume of the water sample and t_c is the total counting time in seconds (86400 s).

Effective dose of ingested water (EDIW) was calculated (in mSv/y) using the expression in [14-16]:

$$EDIW = \sum_{i=1}^{3} A_i \times C_i \times D_i \quad (2)$$

where A_i refers to the activity concentrations of the identified radionuclides (^{238}U, ^{232}Th and ^{40}K), C_i is the annual intake of sachet drinking water calculated for the age groups ≤ 1y, 2 – 17y and > 17y with an annual average water intake of 230, 330 and 730 litres per year, respectively [17]. D_i is the ingestion dose coefficients for ^{238}U, ^{232}Th and ^{40}K which are 2.8×10^{-7}, 6.9×10^{-7} and 6.2×10^{-9} Sv/Bq, respectively [14].

4. Results and Discussion

Table 3 displays the activity concentrations of ^{238}U, ^{232}Th and ^{40}K of the samples that were taken from the groundwater of Al-Manathera districts. In addition to that, Table 4 presents the same concentrations of activity for the same elements, but in the healthy drinking water samples taken from the same area. Table 3 shows the concentrations of activity in Bq/l for ^{238}U that ranged from 11.26±0.77 to 15.22±0.89 and had an average value of 8.3±1.2. The Table shows the same measurements for ^{232}Th, which

also ranged from 0.55±0.10 to 3.85±0.27 and had an average value of 1.9±0.4, while ^{40}K went from 26.90±1.24 to 91.71±2.29 with an average value of 57.4±5.7. On the other hand, Table 4 shows the same measurements, but with potable water and found the following Bq/l values that ranged from 0.11±0.02 to 1.25±0.08 with an average of 0.6±0.1o for ^{238}U, for ^{232}Th from 0.002±0.002 to 0.183±0.019 with an average of 0.07±0.02 and from 0.71±0.06 to 6.27±0.19 with an average of 2.7±0.5 for ^{40}K.

TABLE 3. Results of activity concentrations in groundwater samples in the present study.

Sample code	Activity concentrations (Bq/l)		
	^{238}U	^{232}Th	^{40}K
G1	9.12±0.69	1.08±0.14	52.15±1.72
G2	1.94±0.31	3.06±0.24	26.90±1.24
G3	10.41±0.73	2.24±0.20	50.74±1.70
G4	11.26±0.77	0.55±0.10	62.58±1.89
G5	4.33±0.47	0.59±0.11	69.75±1.99
G6	7.30±0.61	1.49±0.17	34.17±1.39
G7	3.66±0.43	2.18±0.20	48.17±1.65
G8	10.85±0.75	3.85±0.27	73.35±2.04
G9	8.51±0.66	0.66±0.11	91.71±2.29
G10	15.22±0.89	3.38±0.25	64.65±1.91
Average ± S.D.	8.3±1.2	1.9±0.4	57.4±5.7

TABLE 4. Results of activity concentrations in healthy drinking water samples in the present study.

Sample code	Activity concentrations (Bq/l)		
	^{238}U	^{232}Th	^{40}K
H1	0.12±0.02	0.130±0.016	2.21±0.11
H2	0.65±0.06	0.024±0.007	3.70±0.14
H3	0.61±0.06	0.056±0.010	6.27±0.19
H4	0.68±0.06	0.055±0.010	2.68±0.12
H5	1.25±0.08	0.164±0.018	2.87±0.13
H6	0.58±0.05	0.002±0.002	2.85±0.13
H7	0.97±0.07	0.183±0.019	1.11±0.08
H8	0.11±0.02	0.009±0.004	0.71±0.06
H9	0.63±0.06	0.023±0.007	4.15±0.15
H10	0.40±0.01	0.008±0.004	0.79±0.07
Average ± S.D.	0.6±0.10	0.07±0.02	2.7±0.50

WHO, World Health Organization, had previously set the recommended standards for the allowed limits of radionuclides in drinking water in 2008. These levels were updated in 2011. Such standardized limits were set in accordance with the possible effects that such levels of radionuclides may have on the health of human beings and they were confirmed by a number of experiments of mammals. Results obtained from worldwide averages were compared with the standardized limits recommended by WHO in 2011, which are 1, 1 and 10 Bq/l for ^{238}U (^{226}Ra), ^{232}Th (^{228}Ra) and ^{40}K, respectively [17]. Results showed that groundwater levels of ^{238}U has concentrations of activity that are higher than the internationally allowed levels, whereas the same concentrations of activity for the drinking water were within the allowed limits, except for ^{238}U in H5 sample. The activity concentrations of ^{232}Th in most of groundwater samples are higher than the global average limitations (1 Bq/l), while all values of activity concentrations in healthy drinking water were lower than worldwide average limitations [17]. For ^{40}K as in Tables 3 and 4, it is clear that all values of activity concentrations in groundwater samples are found to be higher than the worldwide average, while healthy drinking water samples had lower concentrations than the worldwide average (10 Bq/l) [17]. According to WHO 2011, Fig. 3 compares the current-work average values and the international average values for water samples. According to the measurements conducted for both drinking water and groundwater samples, it can be observed that the concentrations of activity for Potassium are

greater than those of Uranium and those of Thorium are lower than those of Uranium for the two types of samples. The concentrations of ^{238}U, ^{232}Th and ^{40}K in the groundwater samples are greater than in healthy drinking water. High levels of ^{40}K were also detected in the groundwater samples, which are a function of the geological formation of the area [18]. ^{40}K is the principal naturally occurring source of internal radiation despite its low isotopic abundance [10]. Also, this probably reflects the abundance of Uranium-bearing minerals associated with granite rocks commonly found in the investigated sectors.

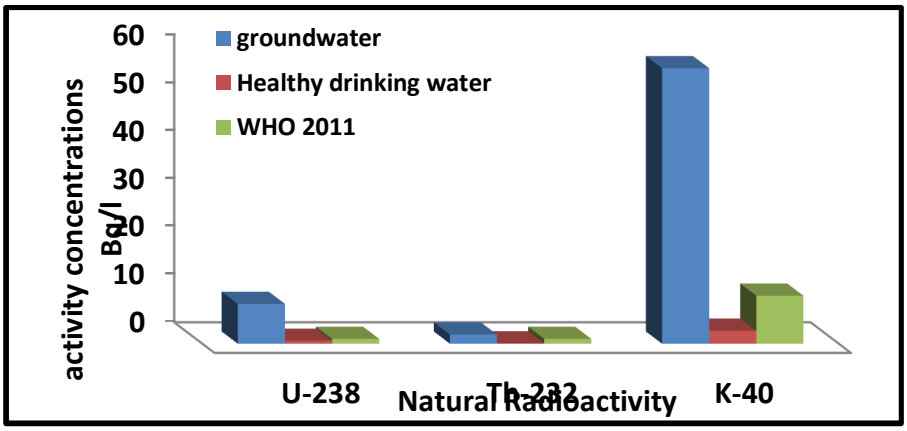

FIG. 3. Comparison of the average of activity concentrations in groundwater, healthy drinking water and WHO 2011.

Tables 5 and 6 present the EDIW consumed by the people, as a result of the absorption of ^{238}U, ^{232}Th and ^{40}K in both the groundwater and healthy drinking water of the three age groups (infants (≤ 1y), children (2 – 17y) and adults (> 17y)), respectively.

TABLE 5. Results of EDIW in groundwater.

Sample code	EDIW (mSv/y)		
	≤ 1 y	2 – 17y	≥ 17y
G1	0.83	1.19	2.64
G2	0.65	0.93	2.06
G3	1.10	1.57	3.49
G4	0.90	1.29	2.86
G5	0.47	0.67	1.50
G6	0.76	1.08	2.40
G7	0.65	0.93	2.06
G8	1.41	2.02	4.49
G9	0.78	1.12	2.49
G10	1.61	2.30	5.11
Average ± S.D.	0.9±0.10	1.3±0.15	2.9±0.3

TABLE 6. Results of EDIW in healthy drinking water.

Sample code	EDIW (mSv/y)		
	≤ 1y	2 – 17y	≥ 17y
H1	0.03	0.05	0.10
H2	0.05	0.07	0.16
H3	0.06	0.08	0.18
H4	0.06	0.08	0.18
H5	0.11	0.16	0.35
H6	0.04	0.06	0.13
H7	0.09	0.13	0.30
H8	0.01	0.01	0.03
H9	0.05	0.07	0.16
H10	0.03	0.04	0.09
Average ± S.D.	0.05±0.008	0.08±0.01	0.17±0.02

The EDIW based on ^{238}U,^{232}Th and^{40}K in groundwater samples for infants (≤ 1y), children (2 – 17y) and adults (> 17y) varied from 0.47 to 1.61 mSv/y with an average of 0.9±0.10 mSv/y, from 0.67 to 2.30 mSv/y with an average of 1.3±0.15 mSv/y and from 1.50 to 5.11 mSv/y with an average of 2.9±0.3 mSv/y, respectively (See Table 5). The EDIW of healthy drinking water samples ranged from 0.01 to 0.11 mSv/y with an average value of 0.05±0.008 mSv/y, from 0.01 to 0.16 mSv/y with an average of 0.08±0.01 mSv/y and from 0.03 to 0.35 mSv/y with an average of 0.17±0.02 mSv/y for infants, children and adults, respectively. In both of Tables 4 and 5, the dosage consumed by adults for groundwater and healthy water EDIW was found to be higher than that of children and infants. The reason behind this difference is that these age groups have variable consumption coefficients as well as different water consumption rates. This leads us to believe that EDIW of samples of groundwater was larger than the acceptable level of 1 mSv/y when comparing the public and general exposure of people and the recommended ICRP 1991 [19] and over 1000% over the recommended level of WHO of 0.1 mSv/y for drinking water. However, the EDIW of all healthy drinking water samples was less than 1 mSv/y [20] although these samples were approved with 0.1 mSv/y drinking water. The current study illustrated that consuming water from groundwater of the study area may be risky due radioactivity that is higher than what is internationally recommended. Studying and measuring radioactivity in drinking water are generally considered means to assess the potentially risky water consumption of groundwater within the study area that may pose further health side-effects to all consumers. The study recommends procedures to be conducted to avoid further health complications to the local population. Healthy drinking water, as shown previously in this study, can be safely consumed and used for daily domestic activities in Al-Manathera district of Al-Najaf city. The study also recommends that similar studies need to be regularly conducted in boreholes, wells and tap water, at least twice a year.

Conclusion

Activity concentrations of (^{283}U, ^{232}Th and ^{40}K) in the taken samples from Al-Manathera show that in the potable water samples were less than those in the groundwater. Furthermore, this study illustrated that the groundwater samples revealed activity concentrations of natural radionuclides (^{238}U, ^{232}Th and ^{40}K) higher than the globally permitted values (1, 1 and 10) Bq/l data from the recommended reference, WHO 2011. However, when the drinking-water samples were tested, it was found that their results were within the internationally allowed limit values. As a result of the combined absorption of each of ^{283}U, ^{232}Th and ^{40}K in groundwater, the average EDIW that people receive within the area of study for the current research is higher than the allowable amount of 1 mSv/y set by ICRP 1991 and 0.1 mSv/y set by WHO, 2000. However, most of the studied samples taken from drinking water contained allowed levels of radioactivity. The study further asserted that, concerning radiological activities, it is risky to consume water from the groundwater sources of the study area, as they exceed the internationally allowed limitations. On the other hand, consuming water from potable-water sources within the same study area poses no health threats to the population according to this study and for the different age groups included in this study.

References

[1] Alaamer, A.S., Turkish J. Eng. Env. SCI, 32 (2008) 229.

[2] United Nations Environmental Programme (UNEP), "Radiation Doses, Effects and Risks", (United Nations, Vol. 13, 1985), pp. 21-40.

[3] Ojovan, M.I. and Lee, W.E., "Naturally Occurring Radionuclides", In: "An Introduction to Nuclear Waste Immobilization", Second Edition, (2014), pp. 31-39.

[4] Pujol, L.I. and Sanchez-Cebeza, J.A., J. Environ. Radioact., 51 (2) (2000) 181.

[5] Ahmed, N.K., Turkish J. Eng. Env. Sci., 28 (2004) 345.

[6] Fatima, I., Zaidi, J.H., Arif, M. and Tahir, S.N.A., Radiation Protection Dosimetry, 123 (2) (2006) 234.

[7] Lydie, R.M. and Nemba, R.M., The South Pacific Journal of Natural Sciences, 27 (1) (2009) 61.

[8] Abojassim, A.A., Iranian Journal of Medical Physics, 16 (1) (2019) 1.

[9] Cooperation with the Local Government, "Development Strategy for the Holy Province of Najaf", Report, Holy Najaf Province Council, (2008).

[10] International Atocmic Energy Agency, Summary report on the post-accident review meeting on the Chernobyl accident. Safety Ser. 75-INSAG-1, IAEA, Vienna, (1986).

[11] ICRP, Ann. ICRP, 26 (1) (1996) 1.

[12] Abojassim, A.A., Al-Gazaly, H.H., Obide, E.S. and Al-Jawdah A.M., International Journal of Environmental Analytical Chemistry, 100 (1) (2020) 99.

[13] Nwankwo, L.I., West African Journal of Applied Ecology, 21 (1) (2013) 111.

[14] ICRP, ICRP Publication 68, Ann. ICRP, 24 (4) (1994).

[15] Enyinna, P.I. and Uboh, U.G., Journal of Radiological Protection, 37 (1) (2016) 97.

[16] Abojassim, A.A., Al-Gazaly, H.H. and Kadhim, S.H., International Journal of Food Contamination, 1 (1) (2014) 6.

[17] World Health Organization. "Guidelines for drinking-water quality: Second addendum". Vol. 1, Recommendations, (World Health Organization, 2011).

[18] Watson, J.E., Hlth. Phys., 52 (1986) 361.

[19] ICRP, ICRP Publication 60. Ann. ICRP, 21 (1-3) (1991).

[20] World Health Organization (WHO), "Guidelines for drinking-water quality", 4th Edn., (WHO. 2000).

Volume 15, Number 4, 2022. pp. 361-368

Jordan Journal of Physics

ARTICLE

Dynamic Stability of Al-Glass/ Ceramic Composites

Nancy O. Olumese and **Olutayo W. Abodunrin**

Department of Mathematical and Physical Sciences, Afe Babalola University, Ekiti State, Nigeria.

Doi: **https://doi.org/10.47011/15.4.4**

Received on: 08/01/2021; *Accepted on: 19/04/2021*

Abstract: The effects of compaction pressure and particle size on the mechanical properties of Al-Glass/ ceramic-based samples are reported in this study. The samples were of a cross-sectional area of 34.0 x 35.0 mm^2 with varying thicknesses of 20.8-22.10 mm. The particle size of 26.5 nm was used for glass, ceramic and aluminum powders. The samples were made into solids by pressing the materials together at a pressure of 30 MPa. Results showed that ceramic/glass addition and particle size greatly influenced the mechanical stability of the samples. Regarding the particle size, it was revealed that the samples were dynamically stable between 0-20 and 40-60 % weights of glass in the composites. The findings showed maximum strength for 40 % weight of glass or 30 % weight of ceramic in composites in the compression test analysis.

Keywords: Pressure, Particle size, Dynamic stability, Compressive stress, Strain, Yield point.

Introduction

Aluminum known for high ductility was reported to have successfully influenced the structural stability of an amorphous material, like glass. The examination of stress–strain relationship showed the smooth display of stress with corresponding strain points. The samples did not accommodate fracture due to rupture along the curve up to the yield point. This was affirmed in the research work [1]. Subsequently, there was a further study into the stress stability of Al-glass composites in which it was recorded that the stress stability has a specific aluminum composition range [2].

The strain uniformity of Al-glass at the nanometer level was also observed at some specific composition ranges of aluminum in composites [3]. The nanoparticle size of choice has a narrow band gap which enhances fast conduction. The pressure of 30 MPa and the particle size in nanometers were reported in the literature to have supported the dynamic stability of iron-ceramic composites and the temperature stability of Al-glass composites [4, 5].

Dynamic stability is the ability of a system to restore itself to an initial stable state after being perturbed. In other words, it is the ability of a system to regain steady state at the moment of any restrain. Dynamic stability of a compacted material could also imply an increase in stress which corresponds to an equal increase in strain [6]. In such compacted materials, the stress / strain relationship does not accommodate points of fracture and rupture up to the yield point [7]. The fracture toughness is thus improved by the contribution of dynamic stability and maximum compressive strength.

The choice of aluminum is a result of its strength, making it widely used in most construction works. Ceramic/glass has a low ductility [8] with the need for reinforcement by a material of high ductility, particularly when wear resistance is considered. This material in

Corresponding Author: Olutayo W. Abodunrin **Email**: tayoabodunrin@yahoo.com

composites displays mechanical and structural stabilities, which increases the level at which breakage may be experienced during the impact or compression test. Much is yet to be done in the direction of compressive strength by combining metallic elements with ceramic/glass to form composites. Therefore, attention in this study is geared towards determining the dynamic stability at a constant pressure and same particle size. Moreover, Al-glass/ ceramic composites were proposed for industrial and domestic purposes.

Experimental Procedure

The materials used for this study include aluminum powder of a purity level of 95.50 % and sodium silicate liquid obtained from the British Drug House (BDH), England. The tiles and specimen slides were boiled in chromic acid and agitated in trioxoethelene for 30 minutes to remove unwanted particles on their surfaces. Ceramic and glass powders of a particle size of 26.5 nm, which had earlier been crushed and pulverized before sieving with a mechanical mesh at the Center for Energy Research and Development (CERD) in Obafemi Awolowo University, Ile-Ife, Nigeria, were used. Weighing was carried out with a digital weighing balance (Model BT 200) of a sensitivity of 0.001g. Sodium silicate liquid was added in few drops.

A manual press capable of producing one composite at a time with an average thickness of 21.5 mm and a cross-sectional area of 1156 mm^2 was used for molding the samples. The formula for mixing percentages is $Al_{30}Glass_xCeramic_{70-x}$, X= 0, 10.0, 20.0, 30.0, 40.0...70.0. The aluminum, glass and ceramic powders were mixed together in different ratios to form eight samples. Sodium silicate liquid added was between 12.5 -14.5 % of Al-glass/ceramic mixture. Mixing was carried out in a mixer for one hour and the powders were pressed together at 30 MPa. The samples were subjected to the same moisture condition for four weeks in an open atmosphere in the laboratory. The stress, strain and other relevant quantities of the samples were measured with a compressive test machine when subjected to loading from CERD.

Results and Discussion

Mechanical Properties of Al-Glass / Ceramic Composites

In Table 1, the strain has the highest value for 10 % weight of glass in the composite at a pressure of 30 MPa. The stress has the highest value for 40 % weights of glass in the composite at a pressure of 30 MPa. As for the lowest value, strain was noted at 60 % weight of glass in the composite for 30 MPa. Stress has the lowest value at 70 % weight of glass. The bulk modulus has the highest value at 30 % weight ceramic or 40 % weight glass in the composites. In Figs. 1-2, the bulk modulus of 30 % wt. Al with 70 % wt. ceramic (O % wt. glass) indicates that Al-ceramic composites have a modulus of 68.26 MPa compared with Al-glass composites with 65.79 MPa, implying substantial differences in bulk moduli. Although the bulk modulus of Al-ceramic composites is lower than in Al-glass composites, yet the maximum compressive strength of $Al_{30}ceramic_{70}$ of 28.78 MPa is higher than the maximum compressive strength of $Al_{30}glass_{70}$ with 24.81 MPa. The combination of Al with glass and ceramic (Al-glass/ceramic) has generated a very high bulk modulus of 137.31 MPa which is twice the value in each case. In addition, the maximum compressive strength of 71.4 MPa at 40 % wt. glass or 30 % wt. ceramic was also recorded, which doubles the two categories of combination; i.e., Al-glass and Al-ceramic.

TABLE 1. Mechanical properties of samples at room temperature of 27°C, particle size of 26.5 nm and pressure of 30 Mpa.

S/No.	% Al	% Glass	% Ceramic	Compressive Stress (MPa)	Compressive Strain (mm/mm)	Bulk Modulus (MPa)
1		0.00	70.00	28.68	0.42	68.26
2		10.00	60.00	32.44	0.62	52.32
3		20.00	50.00	47.28	0.46	102.78
4	30.00	30.00	40.00	55.15	0.52	106.06
5		40.00	30.00	71.40	0.52	137.31
6		50.00	20.00	53.60	0.60	89.33
7		60.00	10.00	43.70	0.37	118.11
8		70.00	0.00	25.07	0.38	65.97

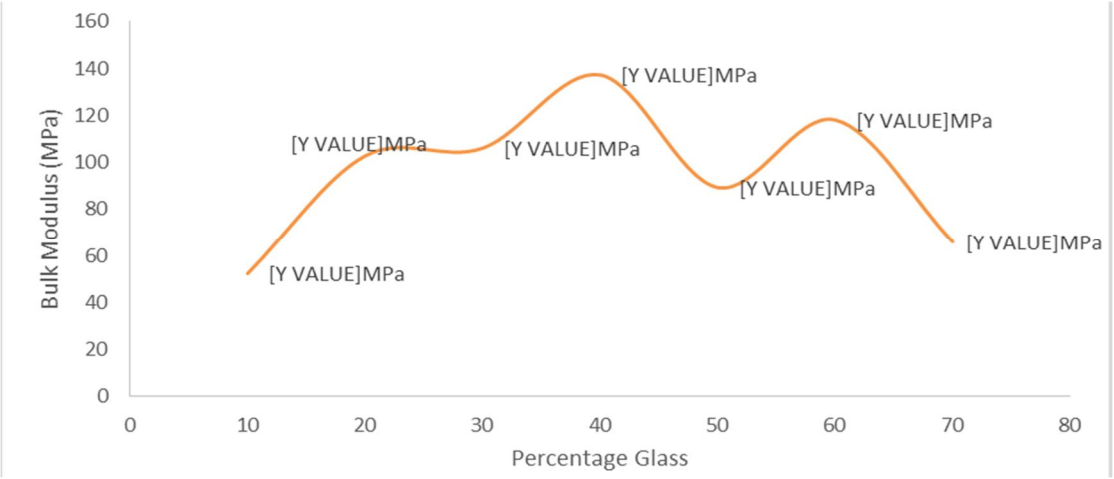

FIG. 1. Bulk modulus *versus* % glass of 26.5 nm at 30 MPa for all samples.

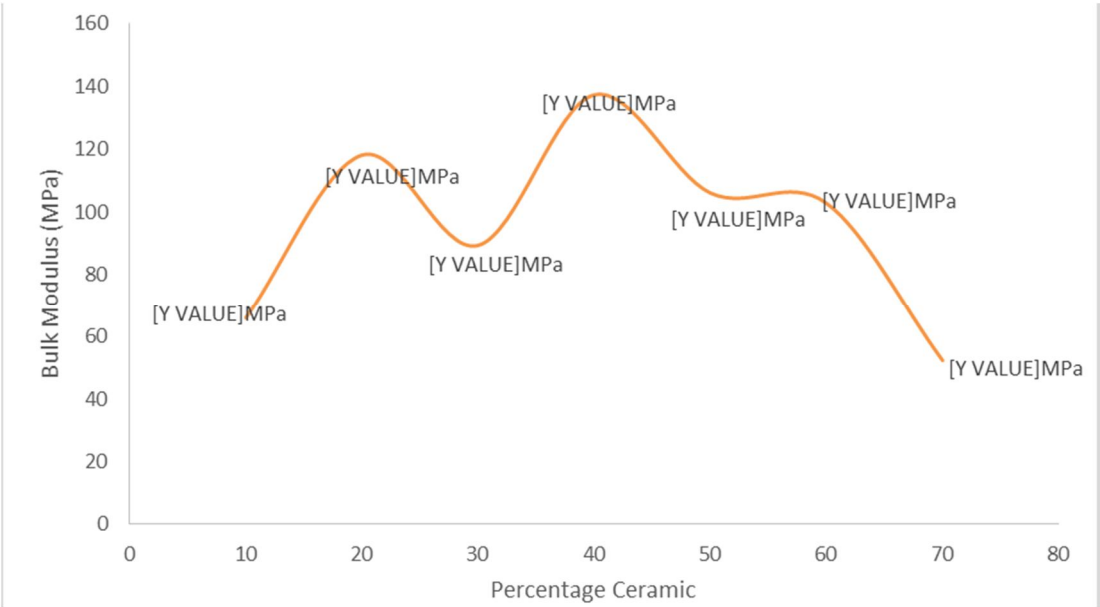

FIG. 2. Bulk modulus *versus* % ceramic of 26.5 nm at 30 MPa for all samples.

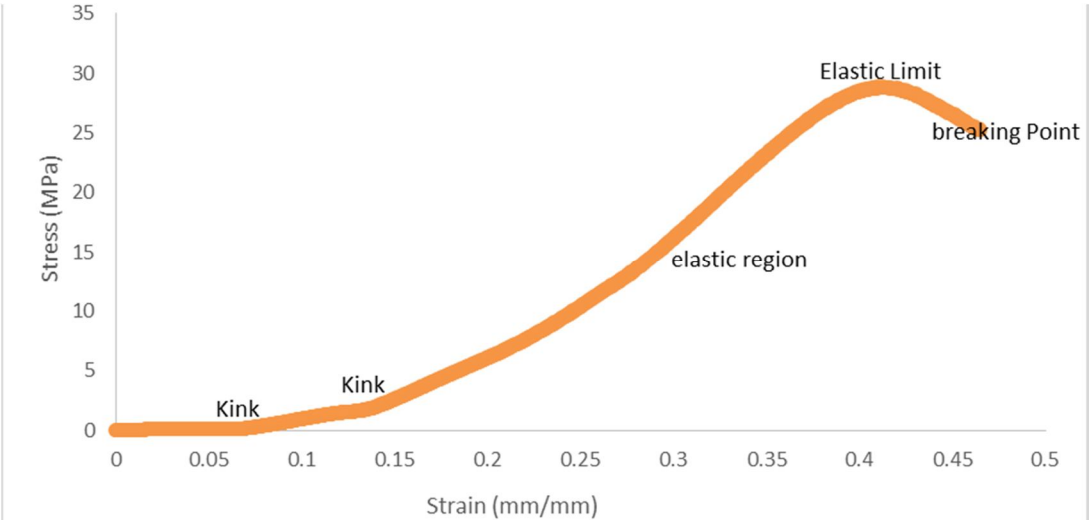

FIG. 3. Compressive stress *versus* strain of 26.5 nm at 30 MPa for $Al_{30}Glass_0Ceramic_{70}$.

The sample in Fig. 3 has its point of breakage at 25.20 Mpa. The maximum compressive stress is also noted at 28.8 Mpa. This implies that the strength of 30 % weight aluminum and 70 % weight ceramic is still low. The curve is smooth with slight kinks at the initial stages. This composite is in one of the categories of dynamic stability. It is in the second class category of dynamic stability because of some noticed kinks.

In Fig. 4, the sample displayed no kinks, no ruptures and no fractures. It is a first-class candidate of dynamic stability. This is because of the perfect smooth curve shown without flaws. The ten-percent addition of glass in the composite of Fig. 3 and the reduction by the same amount in ceramic composition have shown that the maximum compressive strength has received a slight increase to 32.5 Mpa. This was discovered in Fig. 4. From the literature review, it was revealed that samples are noted with dynamic stability at this constant pressure irrespective of various kinks. This might be one of the factors that contributed to the smoothness of the curve. There was an increase in the point of breakage to 28.8 Mpa. This has shown a slight difference compared to the point of breakage of the previous sample of Fig. 3.

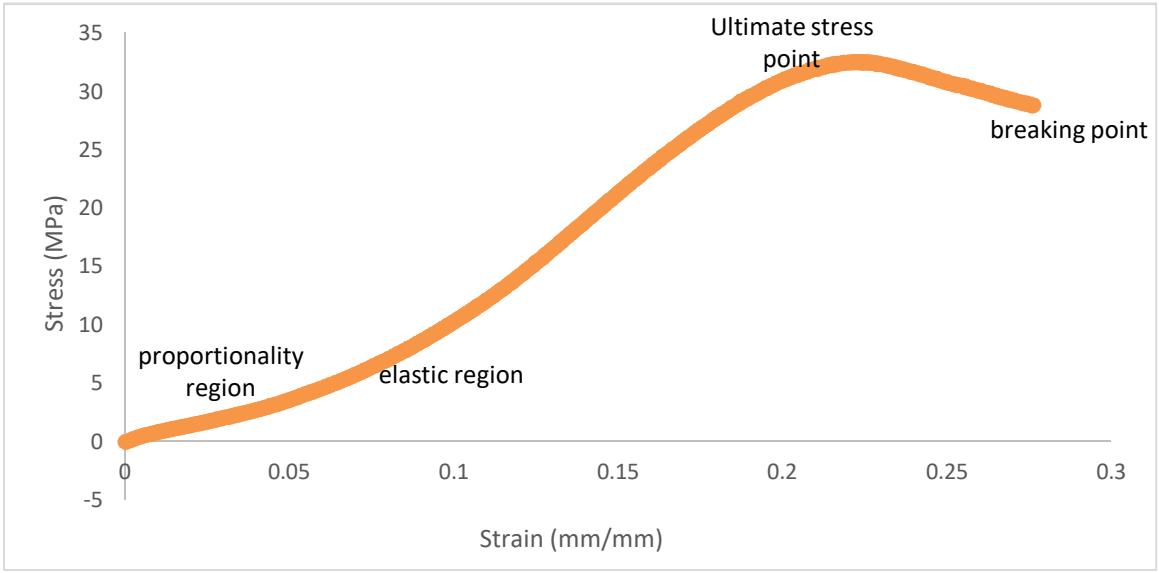

FIG. 4. Compressive stress *versus* strain of 26.5 nm at 30 MPa for $Al_{30}Glass_{10}Ceramic_{60}$.

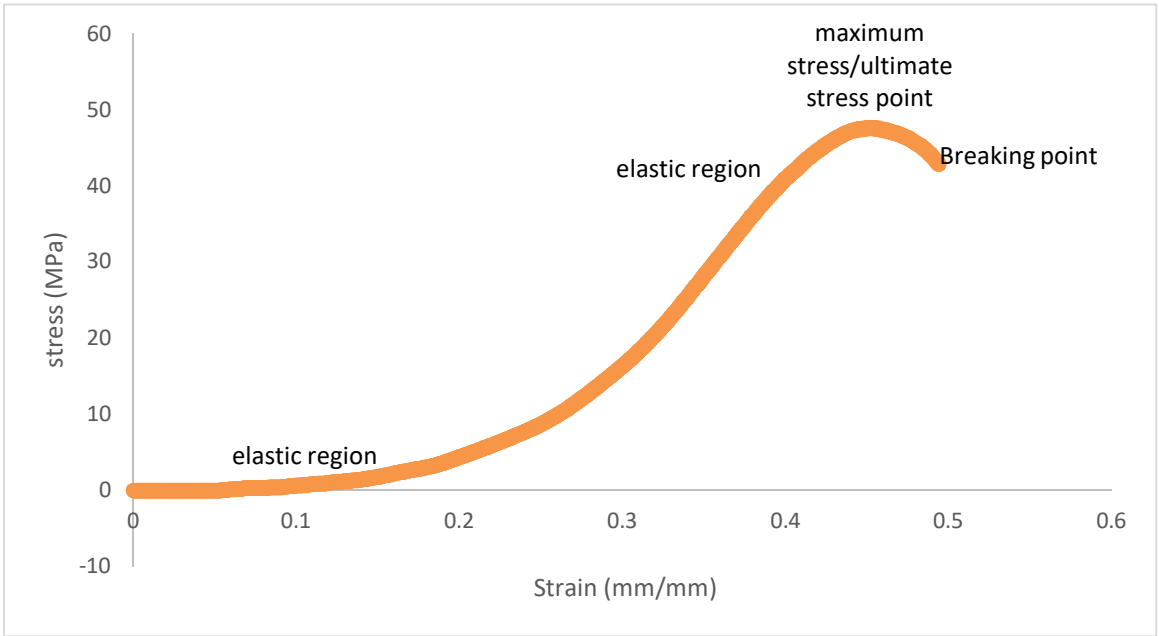

FIG. 5. Compressive stress *versus* strain of 26.5 nm at 30 MPa for $Al_{30}Glass_{20}Ceramic_{50}$.

The composite of Fig. 5 has displayed a higher maximum compressive strength and a higher point of breakage. The curve of this Figure is also known to be in the first-class category of dynamic stability. One can observe the perfect curve without any trace of flaws. Interestingly, this sample is close to the new sample at a reasonable low percentage of glass, but with the highest maximum compressive strength.

In Fig. 6, it has been shown that the maximum compressive strength and the point of breakage coincide at 55.15 MPa. The curve of this Figure is also known to be in the second-class category of dynamic stability because of some regions of plasticity. One can observe the curve with an elastic limit. Moreover, this sample is very close to the new sample at equal percentage of glass or ceramic, but with the highest maximum compressive strength of 71.4 MPa and the highest point of breakage of 68.2 MPa.

Fig. 7 is in the category of second class of dynamic stability. The starting point of the curve to the point of breakage is smoothly captured, but some plastic and elastic regions at the initial stage were embedded in the curve if this smooth display would not have been in the first category of dynamic stability. This has given the impression of a perfect display with the highest point of breakage and the highest maximum compressive strength. The sample is recorded at forty percent weight glass in the composite. The findings have related the preferable combination needed to fabricate or mold any object. The sample with the formula $Al_{30}Glass_{40}Ceramic_{30}$ takes the lead in the investigation carried out, because it does not have fractures or ruptures.

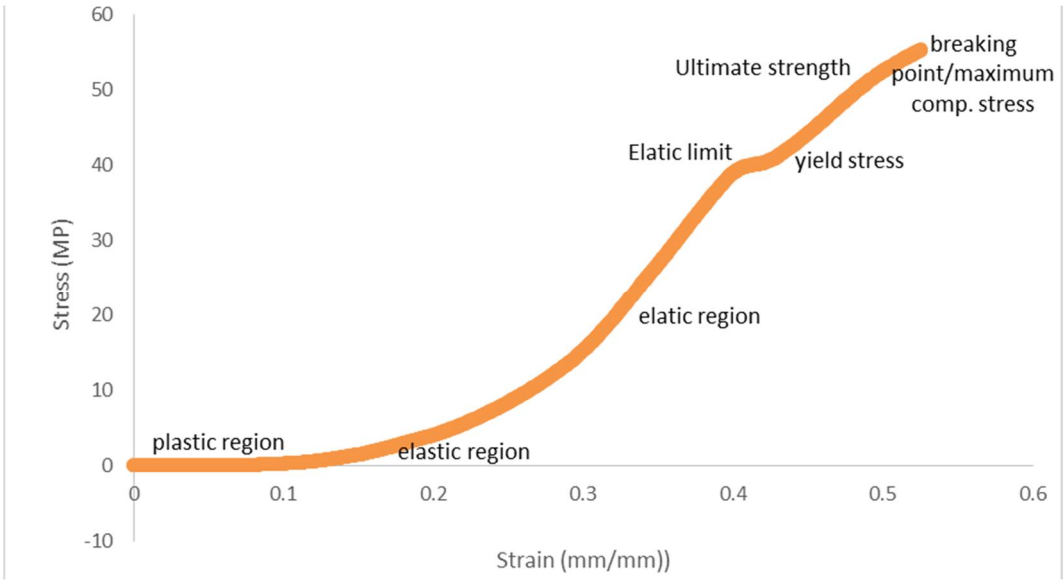

FIG. 6. Compressive stress *versus* strain of 26.5 nm at 30 MPa for $Al_{30}Glass_{30}Ceramic_{40}$.

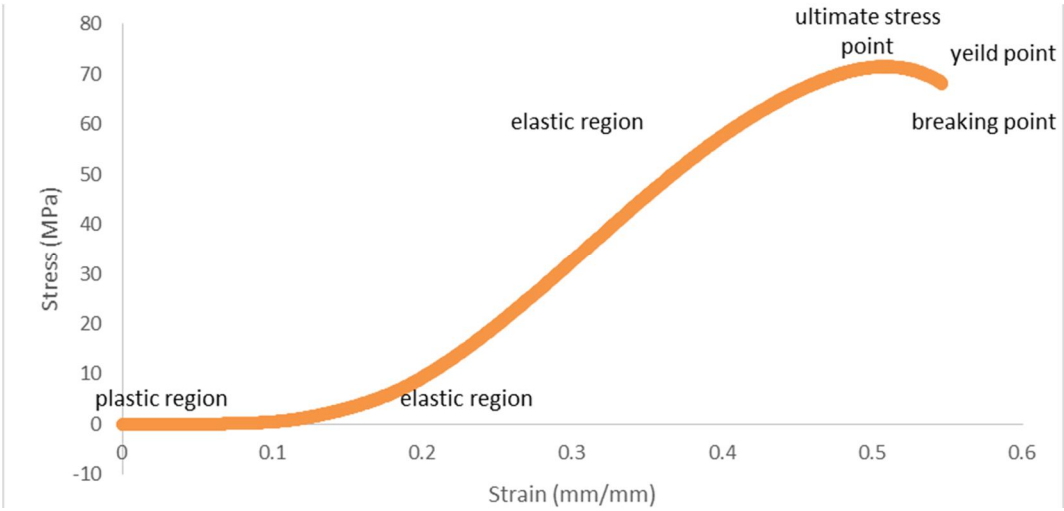

FIG. 7. Compressive stress *versus* strain of 26.5 nm at 30 MPa for $Al_{30}Glass_{40}Ceramic_{30}$.

The composite in Fig. 8 is in the division of the second class of dynamic stability. The inscriptions of many plastic regions and kinks along the curve are indications of dynamic stability in the second category. The point of breakage and the maximum compressive strength were found to be reduced compared to the previous values. The kink is a short depression along the curve which is minor compared to the fracture or rupture.

The sample in Fig. 9 is also in the second category of dynamic stability. The strength has dropped from what is being recorded from the latter figure to 43.7 MPa. This implies that further increase in glass reduces both the strength and the point of breakage. The trend is showing no further increase in this work.

The sample of Fig. 10 does not show the complete dynamic stability, because at the end of the curve, there is rupture. Part of the curve portrays the dynamic stability in the plastic region, while the remaining part towards the end of the curve is noted with stress point and elastic limit. This is a sample of dynamic stability in the second category.

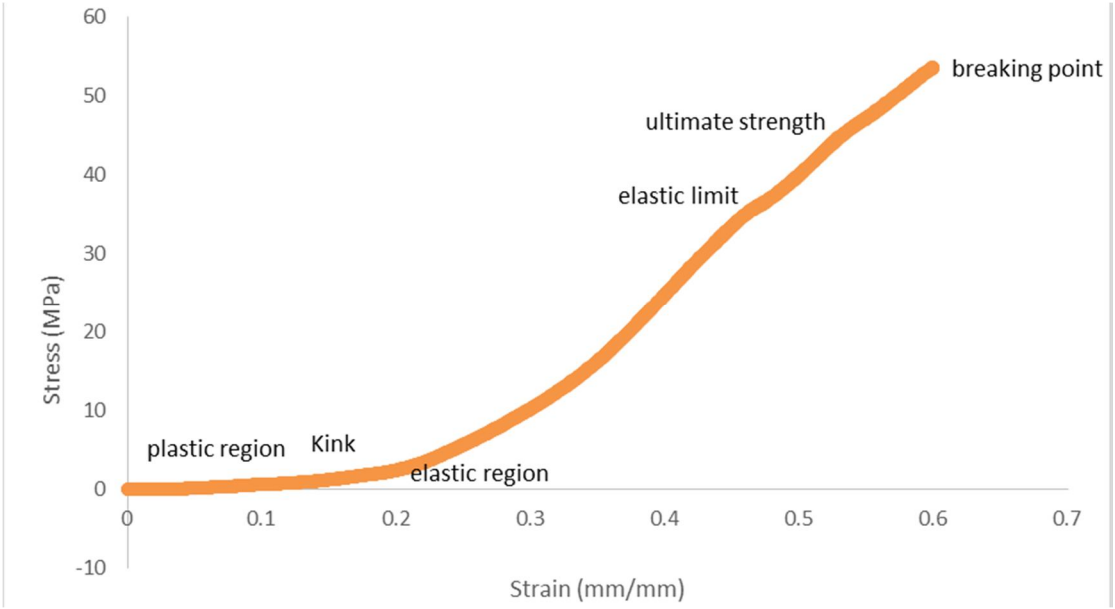

FIG. 8. Compressive stress *versus* strain of 26.5 nm at 30 MPa for $Al_{30}Glass_{50}Ceramic_{20}$.

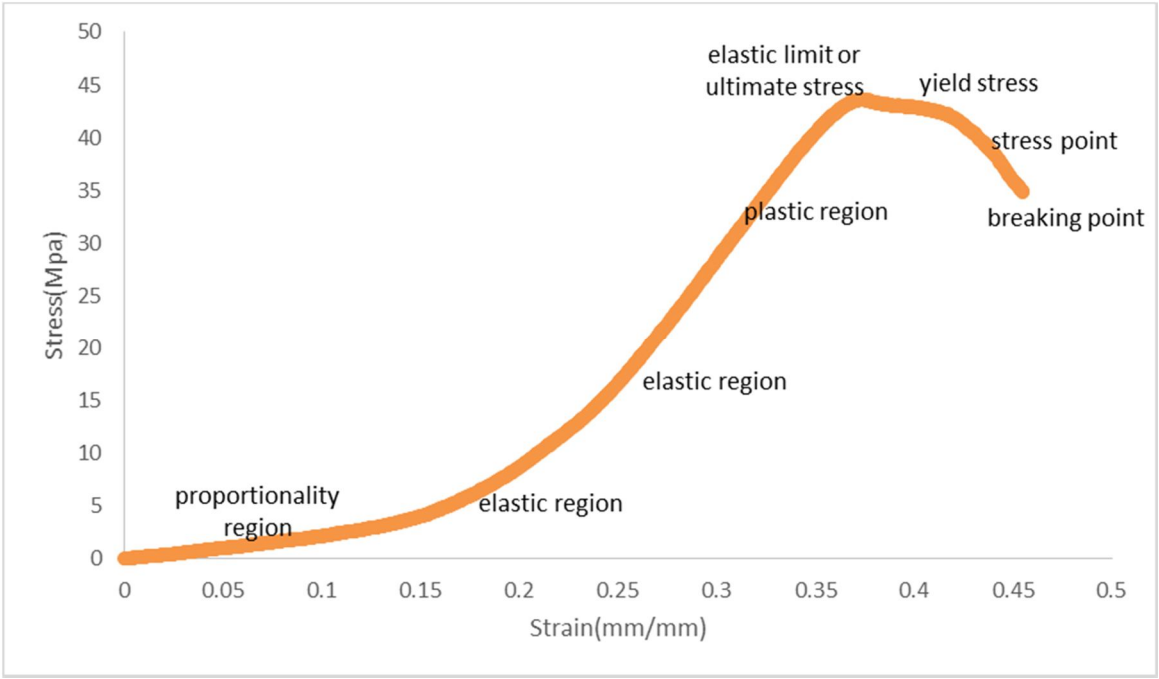

FIG. 9. Compressive stress *versus* strain of 26.5 nm at 30 MPa for $Al_{30}Glass_{60}Ceramic_{10}$.

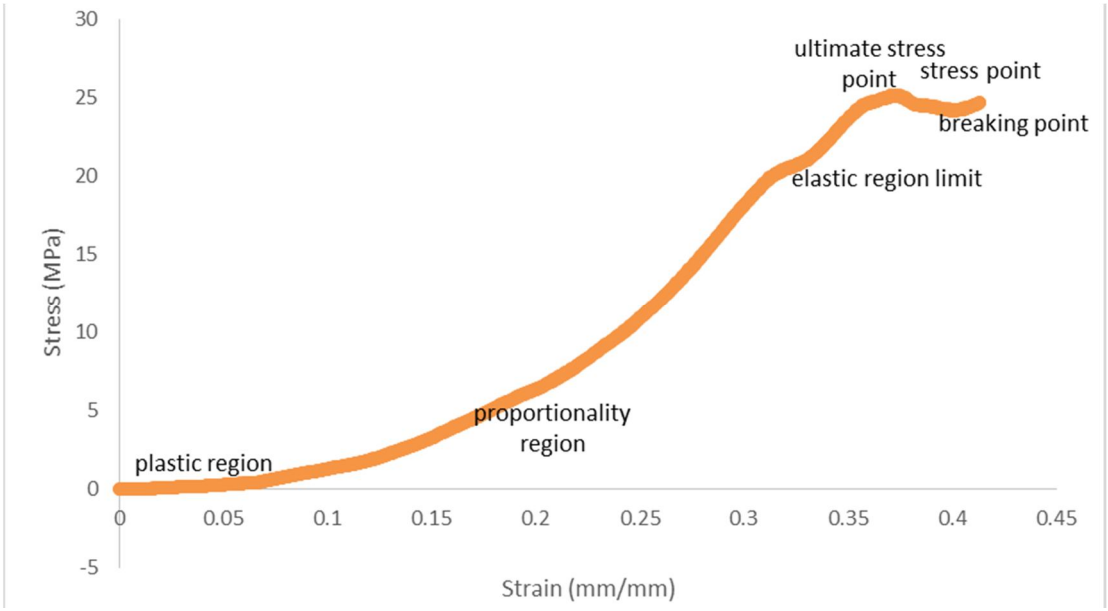

FIG. 10. Compressive stress *versus* strain of 26.5 nm at 30 MPa for $Al_{30}Glass_{70}Ceramic_{0}$.

Maximum Compressive Stress / Strain of Al-Glass / Ceramic Composites

Composites were subjected to increasing load and the values of stress monitored until reaching the maximum value. Beyond this point, distortion sets, which may cause breakage. The relationships between maximum compressive stress and strain and percent weight of glass in the composites at 26.5 nm are shown in Figs. 3 – 10. The results reveal that stress is at its maximum in the case of $Al_{30}Glass_{40}Ceramic_{30}$ with a value of 71.4 MPa, which gives the highest stress obtainable. The compressive stress increases gradually to maximum for $Al_{30}Glass_{40}Ceramic_{30}$ and further decreases gradually to minimum for $Al_{30}Glass_{70}Ceramic_{0}$. It was noted however that at a pressure of 30 MPa, a significant first-class dynamic stability at 26.5 nm for $Al_{30}Glass_{10}Ceramic_{60}$ and $Al_{30}Glass_{20}Ceramic_{50}$ was recorded, while $Al_{30}Glass_{30}Ceramic_{40}$, $Al_{30}Glass_{40}Ceramic_{30}$, $Al_{30}Glass_{50}Ceramic_{20}$ and $Al_{30}Glass_{60}Ceramic_{10}$ were observed with second-class dynamic stability. The results reveal that the Al-Glass/Ceramic composites have improved strength as a result of the nano-particle size of the samples and the constant pressure.

Strength and Dynamic Stability of Al-Glass/Ceramic Composites

Figs. 3 - 10 display a pressure value of 30 MPa and 26.5 nm particle size, whereby the stress–strain relationships were found to be stable over specified ranges, indicating that the materials have the tendency of having dynamic stability.

The results show that as the strain increases, the stress increases gradually without rupture along each of the curves. The increase in strain - stress became noticeable for these composites without fracture along the curves. All these samples are generally classified as being dynamically stable. The variation of stress - strain / time for all samples and their results at 26.5 nm particle size depicts gradual increase in stress - strain along the curve with no ruptures up to the point of breakage. These are indications of dynamic stability of the materials just before the point of breakage.

It should be noted that samples that contain points of rupture and fracture do not have dynamic stability. Samples with dynamic stability must not display the above mentioned flaws. In other words, samples in the category of dynamic stability must exhibit a gradual increase in stress - strain with time. The point of breakage may not necessarily coincide with the maximum compressive stress. The samples have different ranges of values for stability in the region of dynamic stability.

There is an improvement in the composites considered, since ordinary glass has a maximum compressive stress of 30.32 MPa at a particle size of 26.5 nm and a pressure of 30 MPa from the literature, while Al-glass/ceramic composites

in the current study have a maximum compressive stress of 71.4 MPa at a particle size of 26.5 nm. The implication of this is that a new composite that can withstand stress up to 71.4 MPa depending on the particle size is obtained. The sample that can withstand minimum stress is $Al_{30}Glass_{70}Ceramic_{0}$, while that for maximum stress is $Al_{30}Glass_{40}Ceramic_{30}$.

Conclusion

The combination of glass with ceramic had been noted to generally improve the performance in various device applications and utilizations. Therefore, the mechanical properties of aluminum of a specific composition could be adjusted for suitable application and utilization with appropriate reinforcement of glass with ceramic.

In this study, Al-glass/ceramic composites were molded by applying compaction pressure using sodium silicate as the binder. The variation in composition of glass in composites was found to influence the area of the Al-glass/ceramic composites for constant pressure. Improved mechanical strength of pure aluminum from 1.3 MPa of 26.5 nm from the literature to 71.4 MPa depending on the particle size was obtained, while first-class dynamic stability is obtained from 10-20 % weight of glass and second-class category is observed from 30-70 % weight glass in composites at 26.5 nm particle size. The sample was found to have maximum strength for 40 % weight of glass or 30 % weight of ceramic in composites in the compression test analysis.

The material obtained could also be useful for decoration, such as flower vase, and other house hold aesthetics.

References

[1] Abodunrin, O.W. and Oluyamo, S.S., (IOSR) Journal of Applied Physics, 9 (1) (2017) 96.

[2] Abodunrin, O.W. and Alao, F.I., Mechanics, Material Science and Engineering, 11 (2017) 67.

[3] Abodunrin, O.W., Mechanics, Material Science and Engineering, 19 (2019).

[4] Abodunrin, O.W., Mechanics, Material Science and Engineering, 17 (2018) 77.

[5] Abodunrin, O.W. and Abejide F.H., Mechanics, Material Science and Engineering, 16 (1) (2018) 96.

[6] Ferreira et al., J. of Material Research, 20 (2017) 102.

[7] Miracle, D.B. and Senkov, O.N., Acta Materialia, 122 (2017) 448.

[8] Zhang, R.Z. and Reece, M.J., Journal of Material Chem. A, 7 (2019) 22148.

Volume 15, Number 4, 2022. pp. 369-376

Jordan Journal of Physics

ARTICLE

Structural and Dielectric Investigations on Pure and Doped Triglycine Sulfate (TGS) Crystals

Adel Shaheen[a], **Mohammad Aljarrah**[b], **Morad Etier**[b], **Amjad H. El-Sheikh**[c] and **Fathy Salman**[d]

[a] *Department of Physics, Faculty of Science, The Hashemite University, P.O. Box 330127, Zarqa 13133, Jordan.*

[b] *Department of Industrial Engineering, Faculty of Engineering, The Hashemite University, P.O. Box 330127, Zarqa 13133, Jordan.*

[b] *Chemistry Department, Faculty of Science, The Hashemite University, P.O. Box 330127, Zarqa 13133, Jordan.*

[b] *Physics Department, Benha University, Benha, Egypt.*

Doi: **https://doi.org/10.47011/15.4.5**

Received on: 15/01/2021; *Accepted on: 22/03/2021*

Abstract: In this paper, a single crystal triglycine sulfate (TGS) doped with copper sulfate was synthesized using the slow evaporation technique. Structural characterization was carried out using X-ray diffraction and FTIR techniques. Thermal studies revealed that the addition of copper sulfate did not affect the thermal stability of the TGS. In addition, intensive dielectric investigation has been carried out, which showed that the addition of copper sulfate enhances the dielectric permittivity. A change in Curie temperature has been observed upon doping TGS with copper sulfate.

Keywords: TGS doping, Copper sulfate, Dielectrics, Cole-Cole plot.

1. Introduction

Triglycine sulfate (TGS) has good pyroelectric and ferroelectric properties at room temperature. The material is crucial in fabricating electromechanical transducers and infrared sensors [1–4]. Hoshino *et al*. [5] reported that TGS crystallizes with monoclinic structure at room temperature with space group P21. On the other hand, polarization of TGS disappears above its Curie temperature (320K), where the material undergoes second-order phase transition and its space group changes to P21/m.

Horiuchi *et al*. [6] and Rai *et al*. [7] reported that the Curie temperature of TGS is 322 and 323 K, respectively. The structure of TGS ($(NH_2CH_2COOH)_3.H_2SO_4$) is composed from $2(N^+H_3CH_2COOH)$, $N^+H_3CH_2COO^-$ and tetrahedron SO_4^{-2} that are held together with hydrogen bonds [8]. When TGS is exposed to polarized water, the hydrogen bonds break and TGS dissolves into the aqueous phase [8]. Ćwikiel *et al*. [9] studied nuclear magnetic resonance (NMR) of TGS crystal and found a decrease in the dielectric properties after twelve hours of applying, a DC field on the TGS crystal.

Several studies [10-12] reported that undoped TGS crystals have disadvantages over doped ones, like the easiness of depolarization and the high mobility of ferroelectric domains. Dielectric properties of TGS are associated with its domain structure which plays an important role in the function of pyroelectric detectors [10-12].

Corresponding Author: Adel Shaheen **Email**: adel_shaheen@hu.edu.jo

Many researchers have studied the effect of different dopant materials to enhance the pyroelectric and ferroelectric properties of TGS crystals [13–20]. To the best of our knowledge, doping TGS with copper sulfate has not been done so far. The aim of the current work is to investigate the electric and dielectric properties of pure TGS and doped TGS with copper sulfate. Doped and undoped TGS crystals were prepared by using the solution method with slow evaporation.

2. Experimental Work

2.1 Synthesis of Triglycine Sulphate (TGS) Crystals

The undoped TGS crystal and $CuSO_4$-doped TGS crystal were grown by the slow evaporation technique in an aqueous solution. The slow evaporation method is a common one in preparing such materials, snice it is an easy method and enough to obtain a single crystal material. Pure TGS salt was synthesized by mixing 75.07 g of analaR glycine (≥99.5%) with the formula of (NH_2CH_2COOH) and 17.7 mL concentrated sulphuric acid (H_2SO_4, 98%), which corresponds to the molar ratio 3:1. The mother solution was prepared by dissolving the synthesized salt of TGS in de-ionized water. After that, the mother solution was constantly stirred for two hours using a magnetic stirrer to obtain a homogenous solution.

Glycine reacts with sulphuric acid as follows [12, 21]:

$$3(NH_2CH_2COOH) + H_2SO_4 \rightarrow (NH_2CH_2COOH)_3 \cdot H_2SO_4 \ . \quad (1)$$

This solution was filtered out to remove the undissolved particles. The filtered solution was covered with perforated sheet and kept for slow evaporation at room temperature for 28 days. Optically transparent crystals (Pure TGS) were obtained as shown in Fig. 1(a). 1 mol% of $CuSO_4$ was added to the pure TGS to prepare $CuSO_4$-doped TGS. Although all growth parameters were kept the same as for pure TGS, transparent and good-quality crystals of $CuSO_4$-doped TGS were achieved in approximately 15 days, as shown in Fig. 1(b).

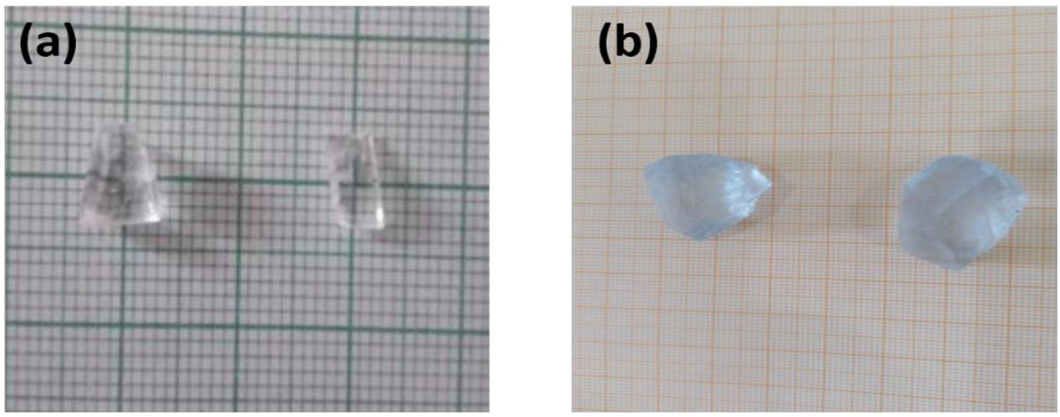

FIG. 1. The synthesized samples of (a) Un doped TGS crystal and (b) $CuSO_4$-doped TGS crystal.

2.2 Characterization Techniques

The TGS single crystals were ground to powder form and then subjected to X-ray diffraction (XRD) with Cu-Kα radiation (λ = 1.54056 A°) [22]. The morphologies of the studied samples were characterized using scanning electron microscopy (SEM). Thermal history during heating and cooling was measured using differential scanning calorimetry (DSC). FTIR spectra were measured using a Vertex 70 FT-IR spectrometer (Bruker, Ltd., USA). Crystal samples for dielectric measurements were polished and their opposite faces were coated with high-grade silver paste (this is to form two electrodes) to obtain a good conductive surface layer. The dielectric data was calculated in terms of the real and imaginary parts Z' and Z" of the impedance Z that was measured using a Solarton-1260 Impedance /Gain Phase analyzer in the frequency range of 1 Hz to 1MHz. The dielectric constant is calculated from [23]:

$$\varepsilon` = \frac{C}{\varepsilon_o} \times \frac{t}{A} = \frac{1}{\omega z`` \varepsilon_o} \times \frac{t}{A} \quad (2)$$

where C is the capacitance, t is the thickness of the sample (t=1mm), ε_O=8.854∗10^{-12} F/m is the permittivity and A is the cross-sectional area of the sample (the radius of the sample was 0.5cm).

The dielectric loss (tan δ) was calculated using the following equation [24-25]:

$$an\delta = \frac{z`}{z``}. \quad (3)$$

The dielectric loss (ε') was calculated using the following equation [22]:

$$\varepsilon'' = \varepsilon' \tan\delta. \quad (4)$$

3. Results and Discussion

3.1 XRD, SEM and DSC

The grown crystals have been characterized by powder X-ray diffractometer. Fig. 2(a,b) represents the powder X-ray pattern of the grown TGS. The system is found to exhibit a monoclinic structure with the space group P2 and the lattice parameters of pure TGS crystal are a=9.601 Å, b=12.650 Å and c= 5.450 Å, which are in good agreement with the literature [7]. It is observed that doping of Cu in TGS crystals had no significant effect on XRD peak positions (i.e., 2θ values), but the relative intensity of the peaks varied due to Cu doping, which may be due to the change in the electronic density in the crystallographic position of the TGS crystal. On the other hand, the X-ray diffraction shows identified peaks to the structure $C_6H_{15}N_3O_6{*}H_2SO_4$ and other phases appeared related to the chalcanthite $CuSO_4{\cdot}5H_2O$. Fig. 2 (c) shows the SEM micrograph for the doped sample. A very smooth surface appeared in the graph without any evidence of cracks or impurities.

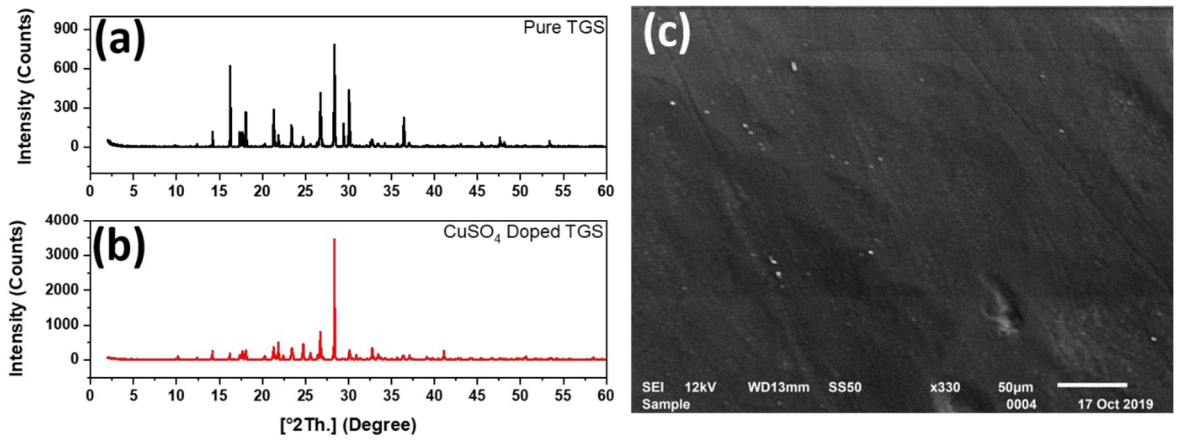

FIG. 2. X-ray diffraction pattern for (a) Pure TGS sample and (b) $CuSO_4$ doped TGS crystal (c) Scanning electron microscopy surface for the $CuSO_4$-doped TGS crystal.

DSC analysis of pure TGS and $CuSO_4$-doped crystals is shown in Fig. 3. The melting point of TGS during heating was 230°C, which is in accordance to that reported by Sinha *et. al* [21] and Mahendra *et al*. [24]. The melting temperature of $CuSO_4$-doped TGS crystal was found to be 230°C. Therefore, doping TGS with $CuSO_4$ does not indicate any change in the thermal stability of TGS.

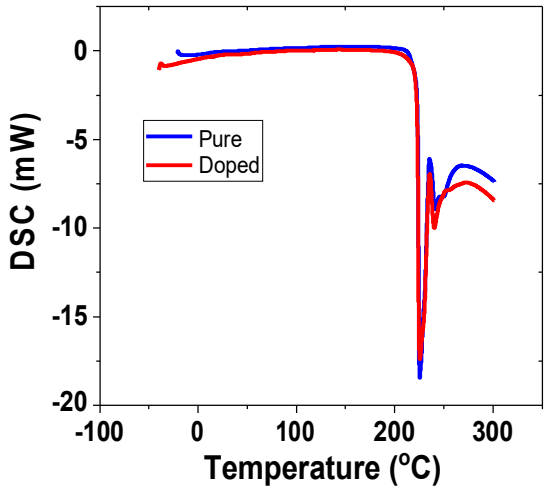

FIG. 3. DSC analysis for pure TGS and TGS doped with $CuSO_4$ crystal.

The FTIR spectra were recorded for pure TGS and $CuSO_4$-doped TGS within the wavenumber range 400-4000 cm^{-1}. The spectra are shown in Fig. 4, while detailed assignments are given in Table 1. A comparison between our results and those previously reported in the literature [11, 21] was conducted in Table 1. Raja *et al.* (2017) [10] prepared an aluminum sulfate-doped TGS, while Sinha *et al.* (2015) [11] prepared a crystal violet-doped TGS. It was noted that the characteristic IR absorption bands of pure TGS were very similar to those reported by Raja *et al.* (2017) [10]. They stated that doping TGS with aluminum sulfate did not affect the IR absorption bands for doping levels up to 1 mol%. A similar conclusion was obtained in this work where the doping of TGS with $CuSO_4$ did not significantly influence the IR absorption bands.

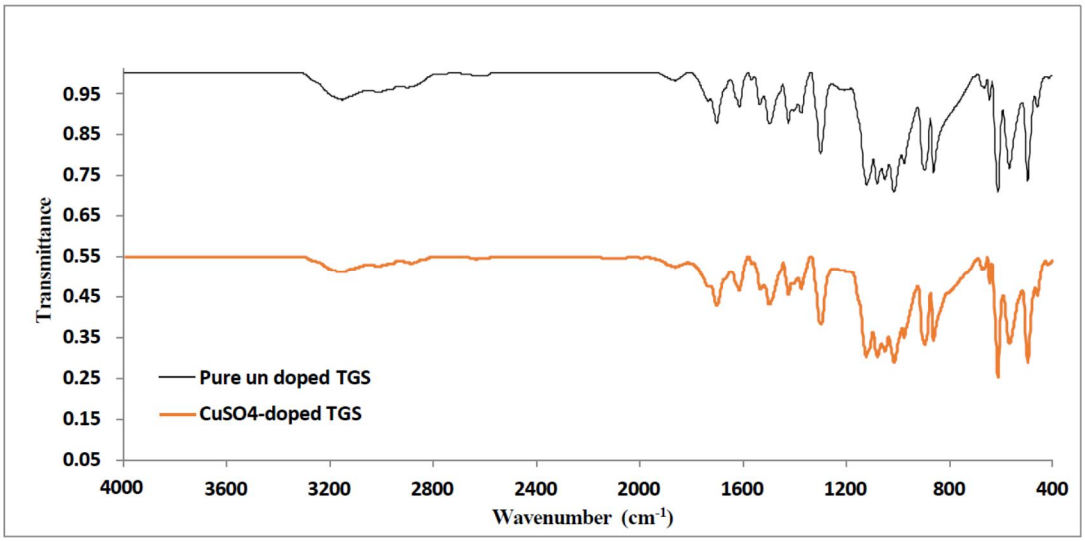

FIG. 4. Overlaid FTIR spectra of pure TGS crystal and $CuSO_4$-doped TGS crystal.

TABLE 1. FTIR vibrational absorption bands (cm^{-1}) of pure and $CuSO_4$-doped TGS, their assignments and comparison with previous works.

Present work (pure and $CuSO_4$-doped TGS)		Comparison with aluminum sulfate-doped TGS [11]		Comparison with crystal violet-doped TGS [21]	
Pure TGS	$CuSO_4$-doped TGS	Band (cm^{-1})	Assignment	Band (cm^{-1})	Assignment
Broad band (2800-3350) with distinguished bands at 3154, 3020, 3007, 2961, 2901	Broad band (2800-3350) with distinguished bands at 3156, 3008, 2882			2800-3350	Asymmetric and symmetric N-H stretching of NH_3^+, C-H stretching of CH2, O-H stretching of H-bonded COOH
2637	2632	2638	CH2 stretching		
1865	1861	1859	NH_3^+ asymmetric bending		
1702	1702	1712	Overtones and combinations	1706	C=O stretching
1615	1615	1627	C=O stretching of COOH	1567-1623	Antisymmetric and symmetric stretching of COO^-
1567	1565				
1536	1533			1501-1538	Bending vibrations of NH_3^+
1499	1497	1496	NH_3^+ asymmetric bending		
1425	1425	1419	NH_3^+ asymmetric bending		

Present work (pure and $CuSO_4$-doped TGS)		Comparison with aluminum sulfate-doped TGS [11]		Comparison with crystal violet-doped TGS [21]	
Pure TGS	$CuSO_4$-doped TGS	Band (cm^{-1})	Assignment	Band (cm^{-1})	Assignment
1300	1298	1303	Asymmetric S=O stretching / CO_2 symmetric stretching + CH_2 twisting		
1122	1123	1126	NC α stretching + NC α 2 3 stretching	977-1127	2- SO_4
1081	1080				
1016	1015	1018	SO_4 vibrations		
976	976				
897, 863	896, 863	902, 856	C-C stretching		
613	613			501-615	NH^+_3 oscillations
569	568	570	NH^+_3 torsional oscillations		
498	498	501	NH^+_3 oscillation		

The broad band between 2800 and 3350 cm^{-1} in the spectra indicates asymmetric and symmetric N-H stretching of NH_3^+, C-H stretching of CH_2, O-H stretching of H-bonded COOH. Multiple combinations and overtone bands of CH_2 have been observed in the region 2300-2650 cm^{-1}. The C=O stretching of carbonyl groups displayed its characteristic peak around 1712 cm^{-1}.

The absorption in the region 1750-1550 cm^{-1} is assigned to antisymmetric and symmetric stretching of C=O in COOH group. The peaks between 1530 and 1300 cm^{-1} in the FTIR spectra can be assigned to NH_3^+ asymmetric bending, asymmetric S=O stretching, CO_2 symmetric stretching and CH_2 twisting. The CH_2 bending modes of glycine are located at 1300 cm^{-1} and 1425 cm^{-1}. The NH_3^+ displays its characteristic bending modes at 1425, 1499 and 1536 cm^{-1}. The peak position between 950 and 1080 cm^{-1} is assigned to stretching modes of carboxyl and sulfate ions.

The peaks due to NH_3^+ oscillations are seen at 896, 569 and 498 cm^{-1}. The assignments showed that the hydrogen bonding extends throughout the TGS mixed $CuSO_4$ molecules. Some of the bands of the copper sulfate-doped TGS samples are either broadened or narrowed, which indicates the presence of copper sulfate in the doped TGS crystal.

3.2 Temperature Dependence of Dielectric Constant ε' and Dielectric Loss ε''

The dielectric constant of the TGS crystals was calculated as a function of temperature at different frequencies, as shown in Fig. 5(a). The magnitude of the dielectric constant increases with temperature till 53°C (Curie temperature), then it decreases for all studied frequencies. The decrease in the dielectric constant above Curie temperature is in accordance with Weiss law [13]. The rapid increase of the dielectric constant may be due to space-charge polarization of thermally generated carriers and the existence of impurities in the TGS lattice [26]. Moreover, the increase of the dielectric constant with temperature – at a certain frequency – as shown in Fig. 5(a) is due to the contribution from the four types of polarizations (i.e., orientation, electronic, ionic and space charge). The decrease in the dielectric constant when the temperature is increased (Fig. 6) may be due to that the orientation polarization varies inversely with temperature [27] or because of the relaxation time which has been found to be fast at high temperatures and increases dramatically at low temperatures, suggesting a freezing of electric dipoles at low temperatures [28]. The temperature dependence dielectric loss of TGS crystals is shown in Fig. 5(b). It can be noticed that temperature has no significant effect on the dielectric loss.

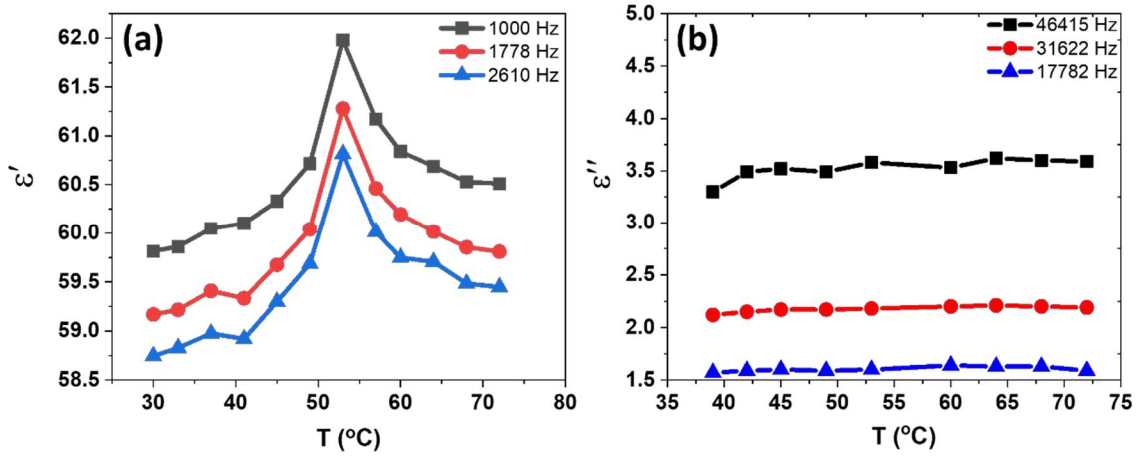

FIG. 5. Frequency dependence of (a) dielectric constant $\varepsilon'$and (b) dielectric loss ε'' for pure TGS sample.

The obtained results of frequency dependencies of the real $\varepsilon'$and the imaginary ε'' parts of the complex dielectric permittivity in single crystal TGS at different temperatures are shown in Fig. 6. The values of both the real ε' and the imaginary ε'' parts are monotonically decreased with increasing frequency. The decrease in the dielectric constant as the frequency increases (Fig. 6) is due to the fact that at higher frequency, only ionic and electronic polarizations contribute. The loss factor, on the other hand, has a small value at low frequency and increases to reach its maximum value as the frequency increases (see Fig. 6). This behavior exhibited by the loss factor may be due to the contributions from all the four types of polarization [29-30].

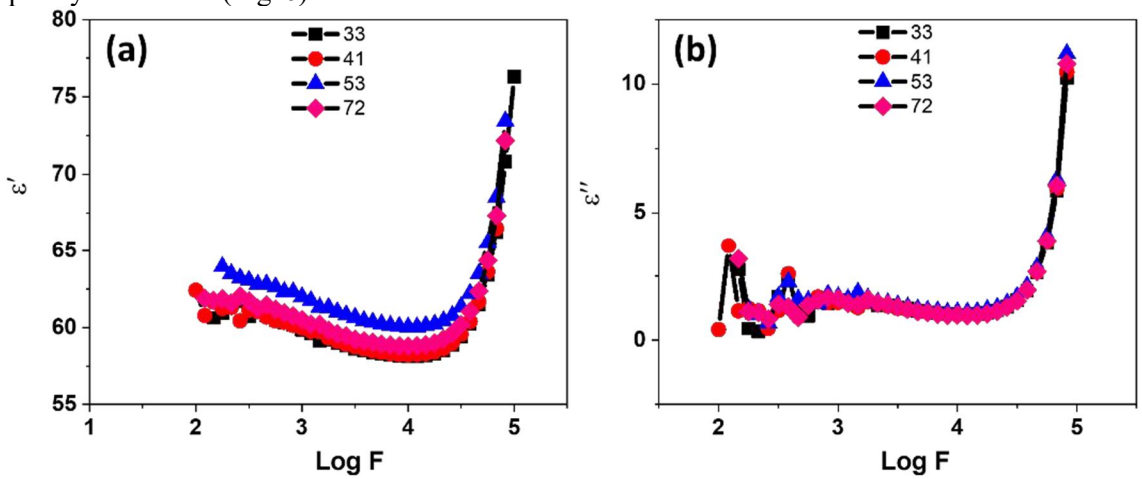

FIG. 6. Dielectric constant ε' and dielectric loss ε" *versus* log f for the pure TGS sample.

3.3 Effect of $CuSO_4$ Doping

Variation of dielectric permittivity as a function of temperature (30-75ºC) for both pure TGS and $CuSO_4$- doped TGS samples is shown in Fig. 7. The Curie temperatures for the pure sample and the doped one were observed to be 53ºC and 55 ºC, respectively. The dielectric constant increases up to the Curie temperature and then decreases obeying Curie-Weis law [13]. Adding $CuSO_4$ caused an increase in the dielectric permittivity. The incorporation of $CuSO_4$ in the structure can force the domains to fritter, which increases the value of permittivity [26]. Also, it is known that a multi-domain structure (e.g $CuSO_4$-doped TGS) exhibits higher spontaneous polarizing and dielectric constant than a single-domain structure.

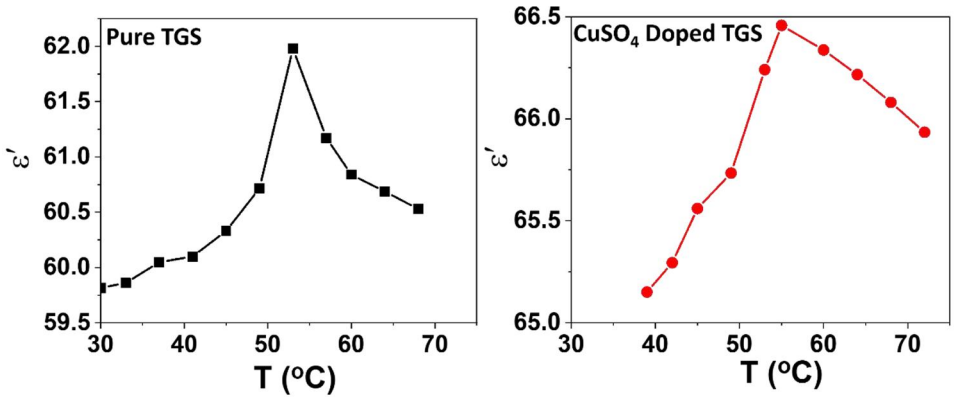

FIG. 7. Temperature dependence of dielectric permittivity of the pure and the doped TGS samples at f=1 kHz.

3.4 COLE- COLE Plots

The Cole–Cole diagrams for TGS crystal at different temperatures in the frequency range (1kHz-1MHz) are shown in Fig. 8. Each plot appeared as a semicircle arc, intersecting the real axis at the values of ε_∞ and ε_S with its center being a part below the real axis and a straight line in the lower-frequency region. The values of ε_S, ε_∞, α and τ were determined at different temperatures by a fitting circuit and are shown in Table (2). These values for pure TGS crystal were found to be similar to those of doped TGS crystal.

Relaxation time τ is a measure of the mobility of the molecules (dipoles) that exist in a material. The movement of dipoles under the field causes collisions and hence internal friction, so that the molecules turn slowly until reaching the final state of orientation polarization with relaxation time constant τ. The obtained values of τ calculated from fitting parameters, in general, are attenuated with increasing temperature.

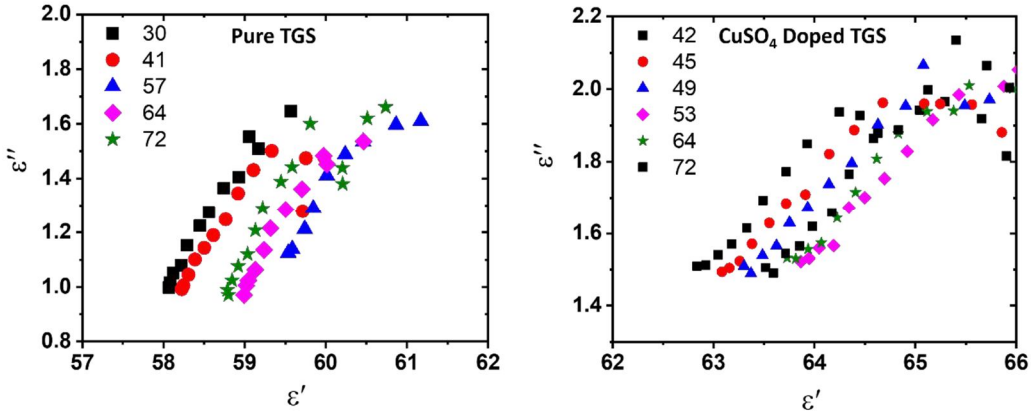

FIG. 8. The Cole-Cole plots for pure TGS and doped TGS samples at different temperatures.

TABLE 2. Infinite and static dielectric permittivity and relaxation time.

T (°C)	ε_∞	ε_S	τ
30	55.97	66.281	3.31E-06
33	56.655	69.516	2.16E-06
37	57.588	61.382	4.15E-05
41	57.427	61.878	0.000119
45	57.259	66.615	8.95E-05
49	57.67	66.187	8.95E-05
53	58.833	66.772	0.000256
57	58.041	65.433	0.000131
60	58.314	63.52	0.000181
64	58.345	62.396	0.000121
68	58.071	62.94	0.000159
72	58.018	64.416	8.95E-05

4. Conclusions

In this paper, TGS single crystal was successfully doped with copper sulfate. Doping TGS is still an area of interest due to the interesting output properties. It was observed that the addition of copper sulfate changes the Curie temperature of the TGS and an enhancement in dielectric permittivity was also observed. The dielectric constant increased up to the Curie temperature and then decreased, thus Curie-Weis law was obeyed. Moreover, the Cole–Cole diagrams for doped and un-doped TGS crystals at different temperatures in the frequency range (1kHz-1MHz) showed similar behaviors.

References

[1] Hang, T., Zhang, W., Ye, H.-Y. and Xiong, R.-G., Chemical Society Reviews, 40 (7) (2011) 3577.

[2] Trybus, M., Proszak, W. and Woś, B., Infrared Physics and Technology, 54 (4) (2011) 326.

[3] Novotný, J., Podvalová, Z. and Zelinka, J., Crystal Growth and Design, 3 (3) (2003) 393.

[4] Sessler, G.M., The Journal of the Acoustical Society of America, 70 (6) (1981) 1596.

[5] Hoshino, S., Okaya, Y. and Pepinsky, R., Physical Review, 115 (1959) 323.

[6] Horiuchi, S. and Tokura, Y., Nature Materials, 7 (5) (2008) 357.

[7] Rai, C., Byrappa, K. and Dharmaprakash, S.M., Physica B: Condensed Matter, 406 (17) (2011) 3308.

[8] Balakumar, S. and Zeng, H.C., Journal of Materials Chemistry, 10 (3) (2000) 651.

[9] Ćwikiel, K., Medycki, W. and Stankowski, J., Solid State Nuclear Magnetic Resonance, 25 (1-3) (2004) 125.

[10] Whatmore, R.W., Reports on Progress in Physics, 49 (12) (1986) 1335.

[11] Raja, R., Santhanam, V., Vedhavalli, D. and Nathan, P.K., International Journal of Materials Science, 12 (2) (2017) 185.

[12] Shanthi, N.T., Selvarajan, P. and Mahadevan, C.K., Current Applied Physics, 9 (5) (2009) 1155.

[13] Bye, K.L., Whipps, P.W. and Keve, E.T., Ferroelectrics, 4 (1972) 253.

[14] Lal, R.B. and Batra, A.K., Ferroelectrics, 142 (1993) 51.

[15] Aravazhi, S., Jeyavel, R. and Subramanian, C., Ferroelectrics, 200 (1997) 390.

[16] Gaffar, M.A. and Al-Fadl, A.A., Cryst. Res. Technol., 34 (7) (1999) 915.

[17] Sun, D., Yu, X. and Gu, Q., Cryst. Res. Technol., 34 (10) (1999) 1255.

[18] Su, G., He, Y., Yao, H., Shi, Z. and Eu, Q., J. Cryst. Growth, 209 (2000) 20.

[19] Biedzycki, K., Solid State Commun., 118, (2001) 141.

[20] Alexandru, H.V., Berbecaru, C., Stanculescu, F. Pintile, L., Matei, I. and Lisca, M., Sensors and Actuators A, 113 (2004) 387.

[21] Sinha, N., Bhandari, S., Yadav, H., Ray, G., Godara, S., Tyagi, N., Dalal, J., Kumar, S. and Kumar, B., Cryst. Eng. Comm., 17 (2015) 5757.

[22] Ayesh, A.I., Abu Haija, M., Shaheen, A. and Banat, F., Applied Physics A, 123 (2017) 682.

[23] Alkhazali, A., Etier, M., Aljarrah, M., Alsukker, A. and Salman, F., World Journal of Engineering, 16 (4) (2019) 477.

[24] Ragahvan, C.M., Sankar, R., Mohankumar, R. and Jayavel, R., Mater. Res. Bull., 43 (2008) 305.

[25] Shaheen, A., Abu Haija, M., Chamakh, M., Assayed, G.A.I., Banat, F. and Ayesh, A.I., Journal of Applied Polymer Science, 137 (24) (2019) 48821

[26] Mahendra, K., Kumar, H.K.T. and Udayashankar, N.K., Appl. Phys. A, 125 (2019) 228.

[27] Banan, M., Lal, R.B. and Batra, A., Journal of Materials Science, 27 (1992) 2291.

[28] Gregory, A.P. and Clarke, R.N., NPL Report MAT, (2012) 23.

[29] Salman, F., Khalil, R. and Hazaa, H., Adv. J. Phys. Sc., 3 (1) (2014) 1.

[30] Maheshwari, P., "Electronic components and processes", (New Age International Publishers, 2008), p. 60.

[31] Ahmad, M.M. and Yamada, K., Appl. Phys. Lett., 19 (5) (2007) 052912-13.

Volume 15, Number 4, 2022. pp. 377-381

Jordan Journal of Physics

ARTICLE

Improved Structural Bonding, Morphology and Mechanical Properties of Poly (Methy Methacrylate) (PMMA) Thin Film Induced by Chloroform Solvent Casting

N. Jamsuzazilawati[a], **C. K. Sheng**[a] and **W. M. Z. Yunus**[b]

[a] *Faculty of Science and Marine Environment, Universiti Malaysia Terengganu, 21030 Kuala Nerus, Terengganu Darul Iman, Malaysia.*

[b] *Centre for Tropicalization, National Defence University of Malaysia, Sungai Besi Camp, 57000, Kuala Lumpur, Malaysia.*

Doi: **https://doi.org/10.47011/15.4.6**

Received on: 20/01/2021; *Accepted on: 15/03/2021*

Abstract: The purpose of this study is to investigate the role of chloroform solvent in improving the structural bonding, surface morphology and mechanical strength of poly (methy methacrylate) PMMA thin film *via* casting method. The functional group of this material was determined using the Fourier transform infrared (FTIR) spectroscopy and the surface morphology was examined by scanning electron microscopy (SEM). The mechanical properties were further characterized using the tensile testing machine and the hardness tester. SEM images reveal that the PMMA film surface exhibits a large and smooth homogeneous surface area, indicating the formation of a clear and highly transparent optical film. FTIR spectra demonstrate a slight band shift and enhanced intensity of C–O and C-H bands for the PMMA thin film as compared to the one in powder form. The mechanical strength of the present PMMA thin film was found to be much higher than that of the commercially available plastic and PMMA thin films, in which this finding could convey a significant insight in order to boost the availability and functionality of the current polymer applications.

Keywords: PMMA thin film, IR spectra, Young's modulus, Mechanical stretching, Hardness.

Introduction

The use of polymers has been expanding in various fields today, such as in medicine, industry and microelectronic and nanotechnology applications. Polymers have profound interest in society. Also, they are increasingly used in many industries as a metal replacement in diverse fields of life. They can also be further modified according to modern applications. Polymers have highly stress and strain rate-dependent properties and show substantially different properties when being produced under different conditions [1-5]. Nowadays, different types of solvents used for polymer dissolution are practiced to modify the properties of polymers to meet the desired requirements for specific applications. Polymers have many applications in industry, such as microlithography, membrane science, plastics recycling and drug delivery [3, 7].

Poly (methy methacrylate) (PMMA) belongs to one of the acrylic glasses, which is a versatile optical material. PMMA has been widely used in the fabrication of optical devices, residential windows and commercial aquariums. This is due to its excellent optical properties and flexible processability as compared to ordinary glass. PMMA offers a high and clear light transmittance. It can be easily formed without loss of optical clarity. Also, it is widely utilized in consumer products due to its unique

Corresponding Author: C. K. Sheng **Email**: chankoksheng@umt.edu.my

mechanical properties and performances under various processing conditions. Besides that, PMMA has a good degree of compatibility with human tissue. Hence, it is widely used in medicine for orthopedic surgery to fix the prosthetic components [3-8]. In this study, we have carried out a novel characterization on the physical properties of a PMMA transparent thin film prepared by solvent casting at room temperature. Chloroform was firstly employed as solvent for PMMA powder dissolution and its role in improving thin film formulation is thoroughly elucidated. The structural and morphological properties of PMMA were identified by Fourier transform infrared spectroscopy (FTIR) and scanning electron microscopy (SEM), respectively. The mechanical properties were characterized *via* hardness and tensile testing machines.

Materials and Methods

PMMA (Sigma-Aldrich) in the powder form and chloroform (Merck) were used as received without further purification. Chloroform was used as solvent for thin-film preparation and to study the effect on the physical properties of PMMA thin film. Firstly, a desired quantity of PMMA powder was dissolved in the chloroform solution. The solution was vigorously stirred in a volumetric flask to obtain a viscous homogeneous mixture and it was then poured into a petri dish and dried at room temperature for 24 hours in a vacuum chamber [6]. Finally, the solid thin film was peeled off from the petri dish and cut into the desired pieces for further characterization. Fig. 1 shows the image of as-received PMMA powder and the PMMA thin film.

The mechanical properties of tensile strength and Young's modulus were characterized using the M350-5 CT universal testing machine and the samples hardness was measured by AFFRI hardness tester, Series 206 EX. On the other hand, the scanning electron microscope (SEM) model JEOL JSM-6360 LA was used to examine the surface morphology and the Fourier transform infrared (FTIR) Thermo Nicolet Alvatar 380 spectroscopy was used to identify the infrared spectral functional groups of the samples.

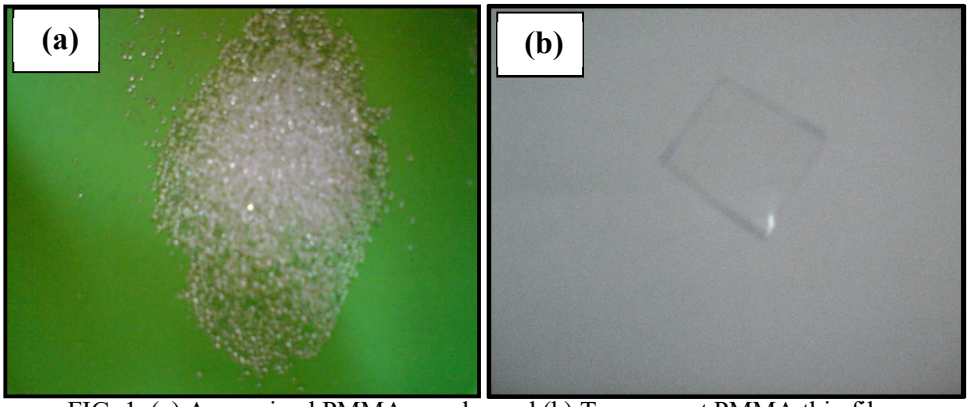

FIG. 1. (a) As-received PMMA powder and (b) Transparent PMMA thin film.

Results and Discussion

A scanning electron microscope (SEM) is capable of producing high-resolution surface morphological images of a studied material. Figs. 2(a), (b) and (c) show the plan-view surface morphology of the PMMA thin film examined by SEM at different magnifications of ×500, ×1000 and ×2000, respectively. From the figures, a smooth, dense and high film uniform surface area is formulated for the present sample, which could signify an optically clear and transparent homopolymer thin-film formulation. Furthermore, there are some small white dots distributed on the sample surface with a size of around 120 nm, which could be responsible for facilitating a high-quality film structure. Chloroform has been reported to serve as a good solvent for most of the polymers/co-polymers and to initiate the dispersion of PMMA nanoparticle residues after solvent evaporation. Furthermore, the homogeneous distribution of the white dots represents the possible presence of quantum dots to improve the structural bonding between the molecules according to Liu et al. [9]. Therefore, it is worth to mention that the present chloroform might play a vital role for nanoparticle dispersion in the polymeric solid film.

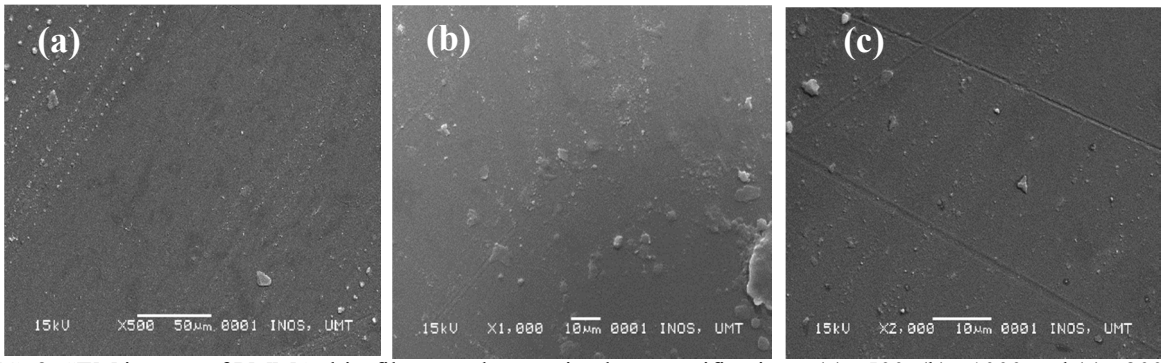

FIG. 2. SEM images of PMMA thin-film sample examined at magnifications: (a) x500, (b) x1000 and (c) x2000.

Almost any organic or inorganic compound that contains covalent bonds would absorb various frequencies of electromagnetic radiation in the infrared region. Hence, the FTIR spectroscopy is a versatile and well-established optical method to study the physical interaction and vibrational mode of the functional group in a material. The IR radiation within the studied energy region corresponds to the range encompassing the stretching and bending vibrational frequencies of the bonds in most covalent molecules. Fig. 3 shows the FTIR spectra of the as-received PMMA powder and thin film produced by evaporation casting. The characteristic bands of the neat PMMA occurred at positions of 679, 752, 842, 988, 1148, 1192, 1240, 1386, 1435, 1726, 2951 and 3728 cm^{-1}. The small band located at 2951 cm^{-1} can be assigned to C-H stretching mode, while two strong sharp peaks observed at 1726 cm^{-1} and 1148 cm^{-1} correspond to the C=O and C–O stretching vibrations, respectively [10]. Relatively, a small sharp peak observed at 1192 cm^{-1} belongs to $–OCH_3$ stretching vibration. Moreover, the intense sharp bands that appeared at 1435 cm^{-1} and 752 cm^{-1} are attributed to C-H bending in CH_3 and CH_2 groups, respectively. Thereafter, it is interesting to note that all the respective bands shift to higher wavenumber when the PMMA powder is transformed into the thin-film phase. This phenomenon indicates that an interactive-bonding reaction occurs between the molecules in the PMMA thin film, as initiated by the chloroform solvent used in the present study. Furthermore, the intensity of the bands assigned for C–O stretching and C-H bending becomes stronger, which might contribute to the improved tensile properties and hardness of the PMMA thin film as compared to the commercially available polymeric films [10].

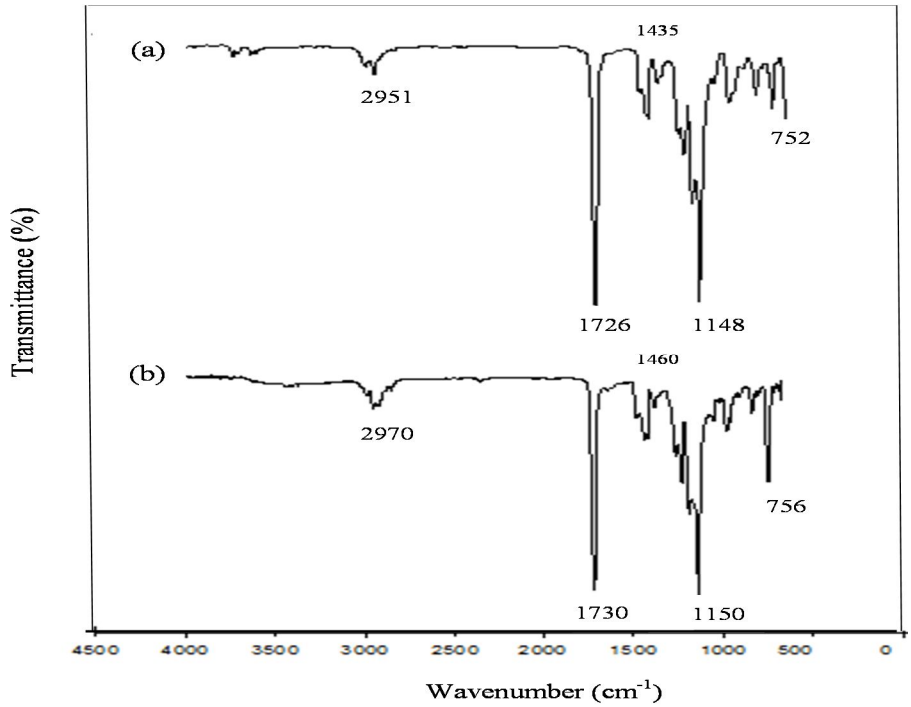

FIG. 3. FTIR spectra for (a) as-received PMMA powder and (b) PMMA thin film.

The tensile test is probably the most widely used tool in order to characterize the mechanical properties of a plastic material. Tensile test measures the force required to break a specimen and the extent to which the specimen stretches or elongates to that breaking point. Thereby, a stress-strain diagram generated from the tensile test is applied to identify the tensile strength, elongation at break and Young's modulus values. Figs. 4(a) and (b) show respectively the stress-strain curve for the PMMA thin film and a commercial plastic used as the reference sample. The ability of a material to resist breaking under tensile stress is one of the most important and widely measured properties of materials used in structural applications. The tensile strength of a material is the maximum amount of tensile stress that it can withstand before failure [11-13]. In the present study, the tensile strength of the PMMA thin film is determined to be 57.80 MPa, while the tensile strength of the commercial plastic film is found to be only 2.59 MPa.

The ultimate elongation (fracture strain) of a material is the percentage increase in length that occurs before it breaks under tension. The ultimate elongation of PMMA thin film (3.93 %) is found to be much lower than that of the commercial plastic film (7.93 %), indicating that the PMMA film is less elastic than the commercial plastic film. This result also reveals that the PMMA film could be classified as a rigid plastic film, which exhibits a fracture strain value under 5 % by referring to the study reported by Pharr et al. [14]. The Young's modulus value of the sample is directly obtained from the tensile testing system. The Young's modulus determined for PMMA thin film is 380.76 MPa, which is much higher than that of the available commercial polymer (2.59 MPa). This finding clearly denotes that the PMMA thin film is much harder than the commercial plastic film. The integration of high ultimate tensile strength and low fracture strain would possibly produce materials with high toughness values. This effect could eventually lead to a high Young's modulus that is defined as the ratio of stress to strain in tension. A high Young's modulus value means that the material is rigid, hence more stress is required to produce a given amount of strain [11, 13]. In the present case, PMMA shows highly strain and strain rate-dependent properties and substantially improves the mechanical behaviors as induced by the chloroform solvent. In comparison, the tensile strength values were obtained to be much higher as compared to those prepared by the thermal solvent method [3, 7]. According to Namouchi et al. [7], PMMA is one of the hard materials with significantly lower hardness and Young's modulus that can be more easily deformed when compared to glass.

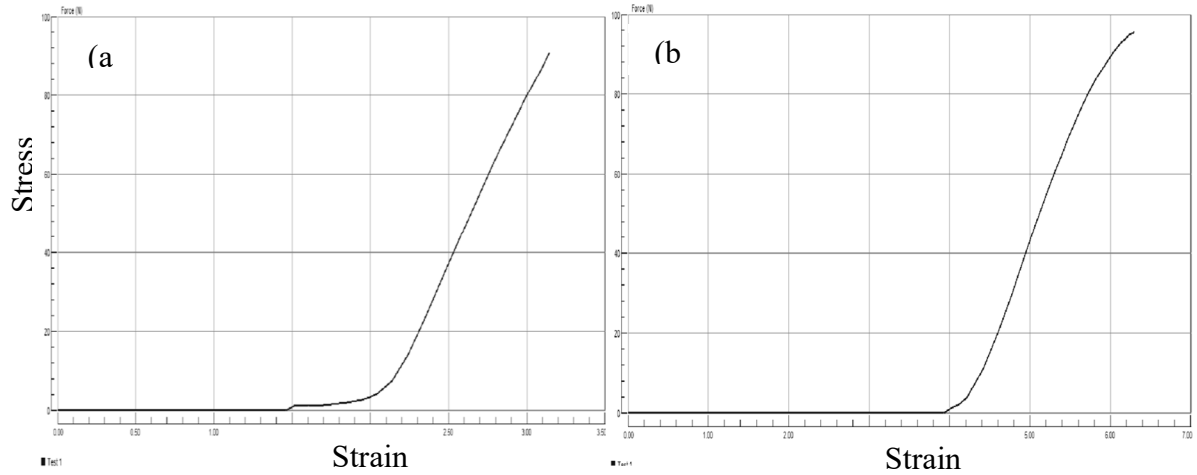

FIG. 4. The stress-strain curve for (a) PMMA thin film and (b) commercial plastic film.

The universal hardness method defines more precisely the hardness of a surface as its general ability to resist plastic deformation by penetration. Recently, Rockwell hardness test has been widely used and proven to be a major advance in the field of hardness testing, which enables the user to perform an accurate hardness test on a variety of sized parts in just a few seconds. In the present study, the Rockwell hardness tester machine was incorporated with a 1/16-inch diameter steel ball (Rockwell B system), with a load of 100 kg for measuring the

hardness of a sample. Under this circumstance, the average hardness value determined for PMMA thin film is 54.30. This result implies that the present film hardness is higher than that of a commercially available plastic film.

Conclusion

The improved structural and mechanical properties of PMMA thin film formulated by chloroform solvent casting was investigated thoroughly by SEM, FTIR, hardness tester and tensile testing machine. A smooth and homogeneous surface is obtained for this sample as observed by SEM. The Young's modulus value determined for PMMA thin film is 380.76 MPa, which is much higher than that of the commercial plastic film. The characteristic bands of PMMA show a slight shift to higher wavenumber and the band intensity assigned to C-O and C-H bonds becomes stronger when the PMMA powder is transformed into the thin film as assisted by chloroform solvent. This effect might contribute to the improvement in tensile properties and hardness of the PMMA film as compared to commercially available plastic and literature-reported PMMA thin films.

References

[1] Trojanowski, A., Ruiz, C. and Harding, J., J. Phys. IV France, 7 (1997) 447.

[2] Okamoto, Y., Yeh, T.F., Lee, H.S. and Skotheimk, T.A., Journal of Polymer Science - Part A, 31 (10) (1993) 2573.

[3] Rittel, D. and Brill, A., Journal of the Mechanics and Physics of Solids, 56 (4) (2008) 1401.

[4] Ali, E.A.G.E., Kim, T.L., Abdullah, M.A.A. and Sheng, C.K., Journal of Sustainability Science and Management, 14 (2019) 4.

[5] Rajendran, S. and Uma, T., Bulletin of Materials Science, 23 (1) (2012) 27.

[6] Sheng, C.K., Amin, K.A.M., Hong, L.L., Hassan, M.F. and Ismail, M., Int. J. Electrochem. Sc., 12 (2017) 10023.

[7] Namouchi, F., Smaoui, H., Guermazi, H., Zerrouki, C., Fourati, N., Agnel, S., Toureille, A. and Bonnet, J.J., European Polymer Journal, 43 (11) (2007) 4821.

[8] Sheng, C.K., Yunus, W.M.M. and Yunus, W.M.Z.W., J. Non-linear Opt. Phys. Mater., 12 (2003) 1.

[9] Liu, C.X. and Choi, J.W., Nanomaterials, 2 (4) (2012) 329.

[10] Pavia, D.L., Lampman, G.M. and Kriz, G.S., "Introduction to Spectroscopy", 4th Edition, (Brookescole Publishers, California, 2008).

[11] Sheng, C.K., Amin, K.A.M., Kee, K.B., Hassan, M.F. and Ali, E.G.E., AIP Conf. Proc., 1958 (2018) 1.

[12] Sheng, C.K., Senin, H.B. and Naimah, I., AIP Conf. Proc., 1136 (2009) 366.

[13] Sheng, C.K., Senin, H.B. and Hamdan, S., AIP Conf. Proc., 1017 (2008) 286.

[14] Pharr, G.M., Oliver, W.C. and Brotzen, F.R., Journal of Materials Research, 7 (3) (1993) 613.

Volume 15, Number 4, 2022. pp. 383-392

Jordan Journal of Physics

ARTICLE

Assessment of Naturally Occurring Radionuclides with Depths in the Soils of Selected Dumpsites, Ogun State, Southwestern Nigeria

Akintayo O. Ojo

Department of Applied Sciences, Federal College of Dental Technology and Therapy, Enugu, Nigeria.

Doi: **https://doi.org/10.47011/15.4.7**

Received on: 03/02/2021; *Accepted on: 02/03/2021*

Abstract: The assessment of natural radionuclides in sixteen soil samples obtained across Saje, Oke-Diya, Premier and Ita-Oshin dumpsites, Ogun State, Southwestern Nigeria was carried out to determine the activity concentrations of ^{238}U, ^{232}Th and ^{40}K and to evaluate possible health hazards that these radionuclides may pose to inhabitants. The samples were collected at profile depths of 0-20, 20-40, 40-60 and 60-80 cm using soil auger. The samples were oven-dried for 24 hours and about 600 g post-sieved samples were sealed for thirty days before analysis using a high-purity germanium detector. The results revealed higher concentrations of ^{40}K compared to ^{232}Th and ^{238}U in the soil samples. Saje samples revealed mean concentrations of ^{238}U and ^{40}K above their global averages, while those of ^{232}Th were below the global averages. The mean concentrations of ^{238}U, ^{232}Th and ^{40}K were all above the global averages for Oke-Diya samples. Ita-Oshin and Premier samples recorded mean concentrations that were below the global averages. The estimated radiological parameters for the representative soil samples were all below the permissible limits, except for the absorbed dose rates of Oke-Diya samples. The study areas generally revealed a reasonably high level of soil radionuclides which may continue to increase with the dumpsites' age.

Keywords: Dumpsites, Soil, Natural radionuclides, Activity concentrations, Health risks.

1. Introduction

Radioactive elements are found naturally in the soil at low concentrations since the formation of the Earth [1, 2]. The most significant natural radionuclides are Uranium-238 (^{238}U) and Thorium-232 (^{232}Th) and their subsequent radioactive decay products, as well as Potassium-40 (^{40}K). They are found at varying degrees of concentrations all over the surface of the Earth [3, 4]. Traces of radionuclides are found in groundwater, ambient air, soil and human bodies. Human beings and other living organisms inhale and ingest radionuclides on a daily basis which have been ubiquitous on earth since its creation [5]. The presence of natural radionuclides in soil results in internal and external exposure of humans [6] and this could lead to increase both carcinogenic and non-carcinogenic health risks in man.

The deleterious radiological adverse health risks posed by human activities, such as solid-waste dumpsites, have attracted great concern and tremendous interest over the years in the field of radiation and health physics due to the enormous amounts of generated wastes, with large constituents of radionuclides being embedded in them [7-9]. According to Telford et al. [10], radionuclides can have both beneficial and adverse effects on all living organisms, but the latter are more, especially when radionuclides are available in excess. The staple food stuffs consumed in most parts of Nigeria contain traces of radionuclides in them [11] and

Corresponding Author: Akintayo O. Ojo **Email**: akintayoojo@yahoo.com

as a result, the dumpsites in which food stuff leftovers were disposed are liable to be highly polluted with radioactive contaminants [11, 12]. Furthermore, [13] reported that the vegetation and most farmlands in Nigeria contain traces of natural radionuclides. Soils with high level of activity concentrations are considered as the main sources of natural background radiation [14, 15]. The need for precise and accurate information on the background ionizing radiation levels in the soils of dumpsites laid credence to this study.

Naturally occurring environmental radiations and radioactivity in soils have received appreciable attention in recent times due to human exposure to different levels of natural radioactive materials, depending on the mineral contents of each region of the earth and the degree of radionuclide pollutions on contaminated sites, such as solid-waste dumpsites [16, 17]. The knowledge of the distribution of natural radionuclides in soils plays an important role in radiation protection and measurement [12, 14, 18]. Gamma-ray measurement techniques are the backbone tool for radionuclide concentration estimation in environmental samples [1], because most radionuclides emit gamma ray. High penetration of gamma rays permits a comparatively simple source of preparation and gamma-ray spectrometry gives good selectivity in discriminating among radionuclides [9, 19]. Gamma-ray spectrometry based on high-purity germanium detectors is preferred for the determination of radionuclides in environmental samples, such as soils, because of its high resolving power, superior energy resolution, high-quality spectral capability, excellent peak symmetry, low-noise operation and efficiency in stopping and detecting high-energy gamma rays [20, 21].

In recent times, Abeokuta had consistently shown the highest level of natural radioactivity in southwestern Nigeria, while the location Jos has the highest level of natural radioactivity in Nigeria [12, 22, 23]. Odunaike et al. [24] studied the radiation dose in some dumpsites within Abeokuta, Ogun State and observed that the radiation doses were minimal compared to global average dose rates, but no matter how low, all levels of radiation still constitute a hazard. A survey of natural radionuclide levels with depth in dumpsite soils within Abeokuta was carried out by Bello and Farinre [7] and the activity concentrations of natural radionuclides indicated low significant health risks to inhabitants. This study therefore seeks to determine the activity concentrations of naturally occurring radionuclides in soils of four selected dumpsites within Abeokuta and Sagamu metropolises and to evaluate the radiological hazard parameters on man due to exposure to these naturally occurring radionuclides.

2. The Study Areas

Abeokuta is located on the basement complex of southwestern Nigeria, while Sagamu terrain is mainly sedimentary and located on the Ewekoro formation (Fig. 1). The study areas are Saje, Oke-Diya, Ita-Oshin and Premier dumpsites (Fig. 2). Saje is the largest dumpsite in Abeokuta and is located in Abeokuta south local government area within latitudes N07º11.201′-N07º11.480′ and longitudes E003º21.001′-E003º22.250′, covering an area of about 119,000 m^2. Oke-Diya is also the largest dumpsite in Sagamu and is located within Sagamu local government area. It has an area of about 60,000 m^2 and is bounded with latitudes N06º48.100′-E06º48.902′ and longitudes E003º35.520′-E003º36.655′. These two study areas have been in operation for the past twenty years. Ita-Oshin and Premier are located within Abeokuta north local government area, Abeokuta and cover approximate areas of 1,600 and 2,000 m^2, respectively. Ita-Oshin lies within latitudes N07º08.085′-N07º08.210′ and longitudes E003º18.351′-E003º18.544′ while Premier is bounded by latitudes N07º09.595′-N07º09.986′ and longitudes E003º18.201′-E003º18.581′. They have been in operation for the past ten years.

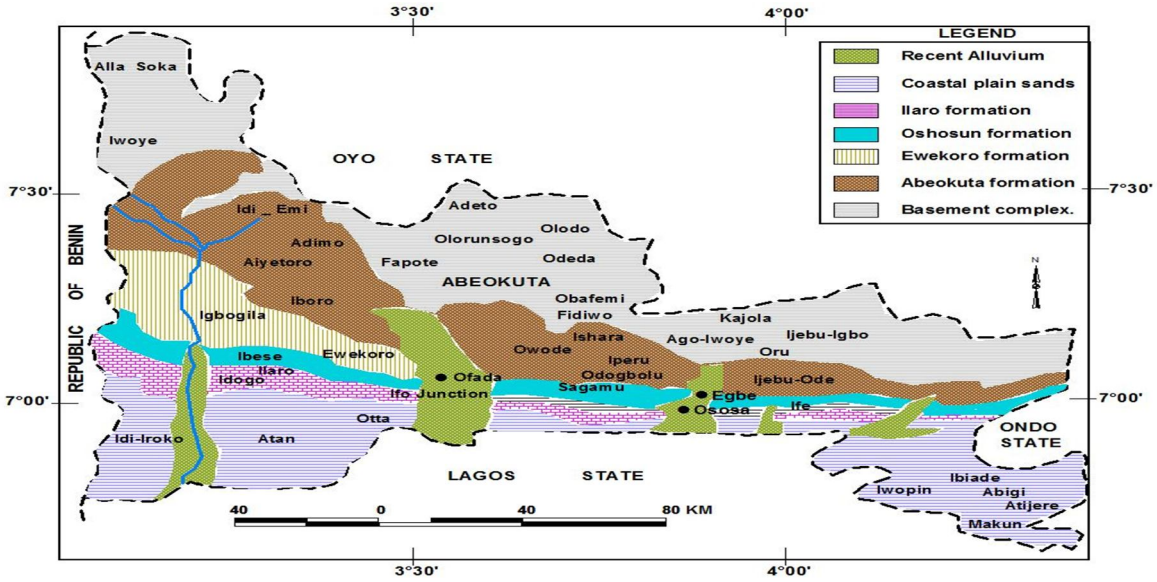

FIG. 1. Geological map of Ogun state showing Abeokuta and Sagamu terrains.

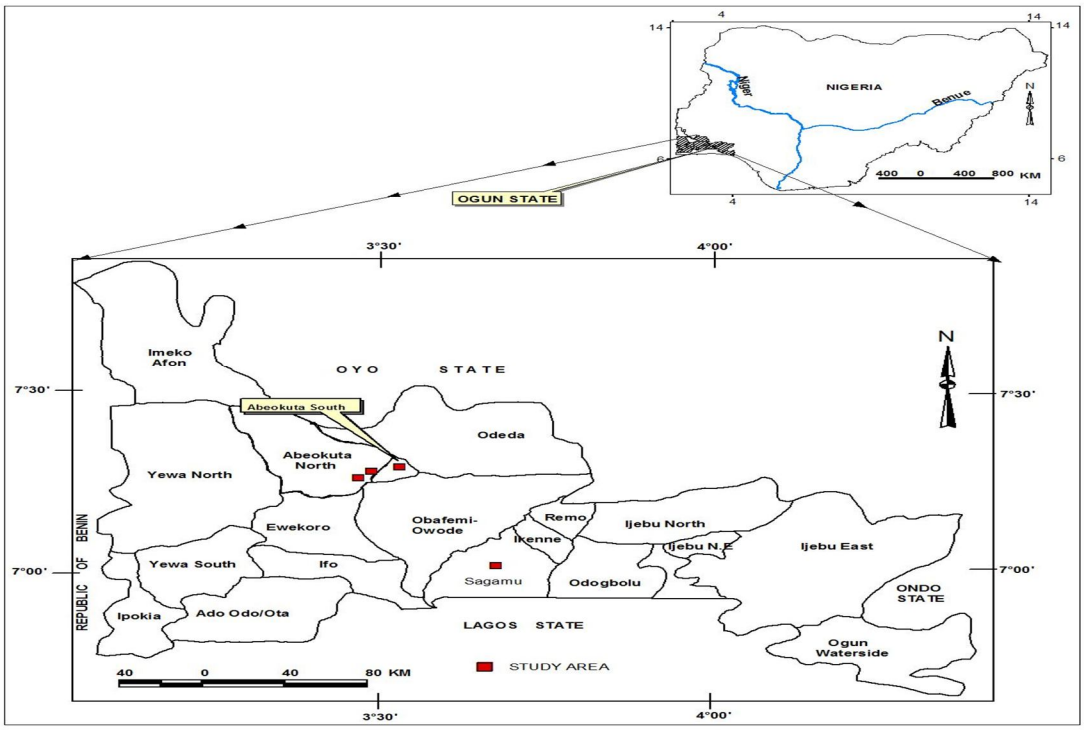

FIG. 2. Map of Ogun state showing the study areas.

3. Methodology

In order to collect sufficient soil samples for radionuclide measurements, about 1 kg of soil was collected at depths of 0-20, 20-40, 40-60 and 60-80 cm at each study area using a soil auger. The depths were measured using a meter tape, while the adequate records of the sampling locations were recorded by the Global Positioning System. Hand disposable gloves were worn to avoid soil contamination. Each sample was first transferred into a 2-mm sieve collecting pan to remove all extraneous materials that could introduce errors into the results. The sixteen post-sieved soil samples were then oven-dried for 24 hours at 100°C to remove significant moisture from the samples [25]. A 100-µm mesh was then used to sieve approximately 600 g of the dried samples to obtain uniform homogenous particle sizes for effective and efficient counting and the samples were parked and sealed in air-tight Marinelli beakers to prevent the escape of gaseous radon [17, 19]. Finally, the samples

were stored for thirty days in order to reach radioactive secular equilibrium [16, 26].

Gamma-spectrometry analysis was performed at the environmental unit, National Institute of Radiation Protection and Research, University of Ibadan, Nigeria, using a p-type coaxial high-purity germanium (HPGe) gamma-ray detector (GEM-25) which has a diameter of 57.5 mm and thick crystals of 51.5 mm and was coupled with a multi-channel analyzer for data acquisition. The spectrometer was set at 2800 volts, 1.67 keV energy resolution, 28.2% relative efficiency and full width at half maximum of 1.33 MeV. In order to avoid interferences of background radiations in the measurements from terrestrial sources, a well-designed suitable cylindrical lead shield was used to cover the detector. Energy calibration was carried out before sample measurement and was repeated prior to the measurements of new samples in order to reduce any changes as a result of subsequent measurements. Also, the counting efficiency of the detector was considered and number of pulses counted was determined to estimate the two significant values of detection efficiencies; the absolute total efficiency and the intrinsic total efficiency. The samples were counted for 86,400 seconds to achieve minimum photo-peak fitting errors [17]. The system was calibrated for photo peak efficiency using multi-gamma ray standard. The spectral data was analyzed using the Genie 2K Canberra software. The container used for the analysis was counted before being filled with the samples and the counts were subtracted from the total counts so as to determine the background radiation distribution [27].

The counting rate is proportional to the amount of radioactivity in a sample, so the activity concentration (A_c) in Bqkg^{-1} for a specific full-energy peak is given by the following Equation:

$$A_c = \frac{C}{\gamma \times \varepsilon(E_\gamma) \times m} \quad (1)$$

where C is the net peak count, γ is the absolute gamma decay intensity for the specific energy peak, m is the mass, and $\varepsilon(E_\gamma)$ is the absolute full-energy peak efficiency of the HPGe detector at this particular gamma-ray energy [28]. The activity concentrations of the soil samples were measured by considering the peaks of ^{238}U, ^{232}Th and ^{40}K at 1764.5, 2614.5 and 1460 KeV, respectively, on the spectra. These concentrations were used to estimate the radiological parameters, such as radium equivalents, gamma absorbed dose rates, annual effective dose equivalents, external hazard index and internal hazard index for individuals living around the study areas.

The radium equivalent (Ra_{eq}) assesses the risks associated with samples containing natural radionulides ^{238}U, ^{232}Th and ^{40}K. The spreads of these radionuclides in soils are not equal and in order to estimate the hazards caused due to the exposure to these radionuclides, their activity concentrations were combined together as given in Eq. (1) to give the radium equivalent in Bqkg^{-1} [15,29]. The universal maximum permissible limit of Ra_{eq} is 370 Bqkg^{-1} [3].

$$Ra_{eq} = (A_K \times 0.077) + (A_u) + (A_{Th} \times 1.43) \quad (2)$$

where A_u, A_{Th} and A_K are the activity concentrations in Bqkg^{-1} of ^{238}U, ^{232}Th and ^{40}K, respectively.

The absorbed dose rate (D) of the soil samples can be deduced from the following equation [30], where the universal maximum permissible limit is 55 nGyh^{-1} [3].

$$D = 0.042\, A_K + 0.429\, A_U + 0.666\, A_{Th} \quad (3)$$

In order to estimate the annual effective dose rate (E) in air, a conversion coefficient of 0.7 SvGy^{-1} for environmental sample exposure to gamma rays of moderate energy must be considered [30], as well as the absorbed dose in air to effective dose received by an adult and the outdoor occupancy factor of about 0.2. The annual effective dose equivalent is then given by Eq. (4) and the global average annual effective dose rate for outdoor or indoor terrestrial gamma radiation is 0.460 mSvy^{-1} [3].

$$E(mSvy^{-1}) = D \times 24hours \times 365.25 \times 0.2 \times 0.7SvGy^{-1} \times 10^{-6} \quad (4)$$

The external hazard index (H_{ex}) and internal hazard index (H_{in}) are deduced from the following Eqs. (5) and (6), respectively [16,17]. The prime objective of these indices is to limit the radiation dose to the admissible permissible dose equivalent limit of 1 mSvy^{-1} [3,30]. The external and internal hazard indices should be ≤ 1.

$$H_{ex} = \left(\frac{A_u}{740}\right) + \left(\frac{A_{Th}}{520}\right) + \left(\frac{A_K}{9628}\right) \leq 1 \quad (5)$$

$$H_{in} = \left(\frac{A_U}{185}\right) + \left(\frac{A_{Th}}{259}\right) + \left(\frac{A_K}{4810}\right) \leq 1 \quad (6)$$

where A_u, A_{Th} and A_K are the activity concentrations of ^{238}U, ^{232}Th and ^{40}K, respectively.

4. Results and Discussion

4.1 Activity Concentrations of Natural Radionuclides in the Soils

The activity concentrations of naturally occurring radionuclides in the sixteen representative soil samples collected from different depths into the soil profiles across the study areas were analyzed to determine the activity concentrations of ^{238}U and ^{232}Th natural decay chains and the long-lived naturally occurring radionuclide ^{40}K (Table 1). Table 2 presents the mean activity concentrations of each radionuclide in comparison with their global averages. Also, Fig. 3 shows the activity concentrations of each radionuclide at various depths. The determination of the specific activity of individual radionuclides in the representative soil samples revealed that ^{40}K had the highest activity concentrations in all the soil samples. Higher concentrations of ^{40}K were also observed in previous research [2, 19, 24, 26].

Saje samples (S1-S4) revealed that the activity concentrations of ^{238}U, ^{232}Th and ^{40}K increased with depth (Fig. 3A) and the highest concentrations of 63.83±8.54, 16.6±2.06 and 600.13±42.43 Bqkg^{-1}, respectively, were observed at depths of 60-80 cm. This probably indicates that the radionuclides had leached down into the subsurface and got accumulated at depths above 80 cm. The leaching action may be due to physical, metamorphic and chemical activities in these study areas, which gives a high tendency of the shallow aquifer getting contaminated. At depths 20-40 and 40-60 cm, the activity concentrations were very close and this probably indicates the migration of radionuclides into the subsurface. The mean activity concentrations of ^{238}U and ^{40}K were above their global averages, while that of ^{232}Th was below its global average.

TABLE 1. Activity concentrations of the soil samples

Locations	Samples	Depths (cm)	^{238}U (Bqkg^{-1})	^{232}Th (Bqkg^{-1})	^{40}K (Bqkg^{-1})
Saje	S1	0-20	13.83±2.54	7.02±1.07	216.38±16.33
Saje	S2	20-40	39.58±6.51	14.70±1.99	461.04±32.03
Saje	S3	40-60	59.05±8.20	15.58±2.05	464.71±32.26
Saje	S4	60-80	63.83±8.67	16.68±2.16	600.13±42.43
Oke-Diya	S5	0-20	37.06±6.12	34.91±4.31	751.29±51.14
Oke-Diya	S6	20-40	44.51±7.38	37.52±4.23	797.85±47.50
Oke-Diya	S7	40-60	56.83±9.06	50.22±6.34	982.86±64.06
Oke-Diya	S8	60-80	25.94±4.40	52.77±6.33	1043.00±68.02
Ita-Oshin	S9	0-20	44.85±7.26	13.25±1.79	819.40±54.36
Ita-Oshin	S10	20-40	40.56±6.40	12.98±1.73	516.05±35.61
Ita-Oshin	S11	40-60	38.53±6.40	5.21±0.45	460.00±32.42
Ita-Oshin	S12	60-80	9.90±2.11	0.16±0.04	69.16±6.67
Premier	S13	0-20	38.69±6.24	35.89±4.65	626.09±50.76
Premier	S14	20-40	26.31±3.40	32.20±6.32	521.16±25.65
Premier	S15	40-60	20.19±6.14	24.10±3.44	245.40±14.56
Premier	S16	60-80	12.54±3.34	12.90±2.11	95.76±7.89

TABLE 2. The mean activity concentrations compared with the global averages

Study Area	^{238}U (Bqkg^{-1})	^{232}Th (Bqkg^{-1})	^{40}K (Bqkg^{-1})
Saje	44.07±6.48	13.50±1.82	473.57±30.76
Oke-Diya	41.09±6.74	43.85±5.30	893.75±57.68
Ita-Oshin	33.46±5.54	7.90±1.00	466.30±32.27
Premier	24.43±4.78	26.27±4.13	372.10±24.72
Global Averages [3]	35	30	400

Oke-Diya samples (S5-S8) showed that the activity concentrations of the soil samples increased with depth (Fig. 3B), except for ^{238}U that had its highest concentration at depths of 40-60 cm. The soil samples had the highest concentrations of 56.83±9.06, 52.77±6.33 and 1043±68.02 Bqkg^{-1} for ^{238}U, ^{232}Th and ^{40}K, respectively. The mean activity concentrations were all above their respective global averages. The high concentrations observed could be attributed to the age, geology and nature of the materials dumped on this site, which were mostly industrial and domestic municipal wastes as well as contraband goods. The highest and lowest concentrations of ^{238}U were at depths 40-60 and 60-80 cm respectively. The radionuclide had probably leached down into the subsurface due to the high infiltration nature of the terrain and got accumulated at depths of 40-60 cm. The highest concentrations ^{232}Th and ^{40}K were at depths of 60-80 cm, and the pattern in which the concentrations increased with depth indicated migration of these radionuclides into the subsurface. The pattern also indicated the high tendency of the shallow water aquifer being polluted.

Ita-Oshin samples (S9-S12) revealed the highest concentrations of 44.85±7.26, 13.25±1.79 and 819.40±54.36 Bqkg^{-1} for ^{238}U, ^{232}Th and ^{40}K, respectively, at surface depths of 0-20 cm. The radionuclide concentrations decreased with depth (Fig. 3C) and the mean activity concentrations of ^{238}U and ^{232}Th were below their global averages, while the mean concentration of ^{40}K was above the global average. Ita-Oshin samples generally revealed low concentrations of radionuclides at depths above 60 cm and relatively high concentrations at depths below 60 cm. Premier samples (S13-S16) revealed low concentrations of radionuclide compared to other study areas and moreover, the concentrations decreased with depth (Fig. 3D). The low concentrations could be due to the age of the dumpsite and the nature of wastes dumped on it, which were majorly domestic municipal wastes. The highest concentrations of ^{238}U, ^{232}Th and ^{40}K at the surface depths (0-20 cm) were 38.69±6.24, 35.89±4.65 and 626.09±50.76 Bqkg^{-1}, respectively. Also, the mean activity concentrations of the radionuclides were all below the global averages. The observations in Ita-Oshin and Premier samples suggested that these radionuclides had not leached to depths above 60 cm in the subsurface; therefore, they may not be posing much havoc to the surface water and shallow aquifer.

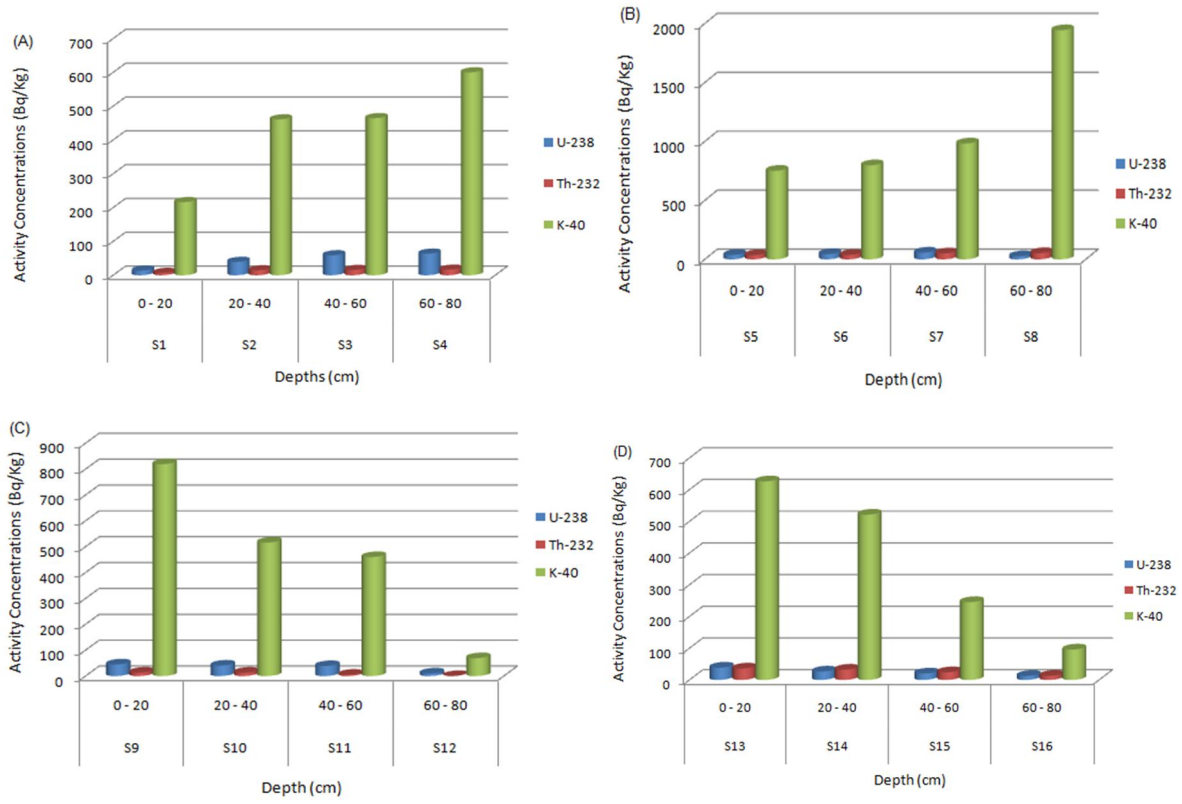

FIG. 3. Radionuclide concentrations with depths:(A) Saje (B) Oke-Diya (C) Ita-Oshin (D) Premier.

The mean activity concentrations of radionuclides ^{238}U, ^{232}Th and ^{40}K obtained in this study were within the ranges obtained by previous studies in Abeokuta (54.60, 2.09 and 426.91 Bqkg^{-1}) [7]; (43, 84 and 329 Bqkg^{-1}) [12]; Port-Harcourt (25.58, 10.97 and 326.47 Bqkg^{-1}) [19]; Agbara (26.3, 38.1 and 531.1 Bqkg^{-1}) [26]; Ibadan (26, 54 and 619 Bqkg^{-1}) [31]; Igbokoda (19.76, 31.98 and 494.64 Bqkg^{-1}) [32]; India (24, 55 and 549 Bqkg^{-1}) [33] and Georgia (53.57, 53.18 and 879.76 Bqkg^{-1}) [34].

4.2 Estimation of Radiological Parameters

The activity concentrations for the naturally occurring radionuclide distributions in the representative soil samples at different depths into the soil profile were used to estimate the radiological parameters for individuals living around the study areas (Tables 3).

4.2.1 Radium Equivalent (Ra_{eq})

The radium equivalent (Ra_{eq}) gives a single index used to describe the gamma absorbed output from different mixtures of uranium, thorium and potassium in the soil samples. The mean value of radium equivalent (Ra_{eq}) in the representative soil samples (S1-S16) from Saje, Oke-Diya, Ita-Oshin and Premier study areas were 96.91±11.45, 172.62±18.76, 80.65±9.46 and 90.65±12.59 Bqkg^{-1}, respectively. These values were considered to be normal, because they were all less than the permissible limit of 370 Bqkg^{-1}. Oke-Diya samples, S5-S8, had the highest values of 144.83±16.22, 159.60±17.09, 204.32±23.06 and 181.71±18.69 Bqkg^{-1}, respectively. Ita-Oshin soil samples, S9-S12, had the least values of 126.89±14.01, 98.86±11.62, 81.40±9.54 and 15.45±2.68 Bqkg^{-1}, respectively.

4.2.2 Gamma Absorbed Dose Rate (D)

The gamma absorbed dose rates of Saje samples (S1-S4) had values ranging from 19.70±2.49 to 63.70±6.94 nGyh^{-1} with the mean dose rate of 46.19 nGyh^{-1}. The absorbed dose rates of S3 and S4 obtained at depths of 40-80 cm were higher than the published maximum admissible limit of 55 nGyh^{-1}, while S1 and S2 dose rates were below the limit. Generally, the gamma absorbed dose rates increased with depth. Oke-Diya samples (S5-S8) had gamma dose rates above the admissible limit at all depths. The dose rates ranged between 70.70±7.64 (depths of 0-20 cm) and 99.12±10.80 nGyh^{-1} (depths of 40-60 cm) and the mean gamma dose rate was 84.37 nGyh^{-1}. Oke-Diya had the highest values of gamma dose rates and this could pose a threat to the local aquifer and agricultural production if the site is used for growing crops. Ita-Oshin samples (S9-S12) dose rates ranged between 7.26 (depths of 60-80 cm) and 69.48 nGyh^{-1} (depths of 0-20 cm). The gamma dose rates decreased with depth and the mean value was 40.94 nGyh^{-1}. The dose rate of S9 was higher than the admissible standard, while the other samples had values within the permissible limits. Premier samples (S13-S16) revealed the highest absorbed dose rate of 66.80±7.91 nGyh^{-1} at depths of 0-20 cm and the lowest absorbed dose rate of 17.99±3.17 nGyh^{-1} at depths of 60-80 cm. The mean gamma dose rate was 43.64 nGyh^{-1}. At depths of 0-20 cm, S13 had a dose rate above the standard limit, while samples at depths above 20 cm (S14-S16) had lower dose rates when compared to the limits.

TABLE 3. The gamma dose rate (D), radium equivalent (Ra_{eq}), annual effective dose equivalent (E), external hazard index (H_{ex}), and internal hazard index (H_{in}) of the radionuclides in the soil samples compared to their permissible limits

Samples	Depths (cm)	Ra_{eq} (Bqkg^{-1})	D (nGyh^{-1})	E (mSvy^{-1})	H_{ex} (mSvy^{-1})	H_{in} (mSvy^{-1})
S1	0-20	40.53±5.33	19.70±2.49	0.024±0.003	0.054±0.007	0.147±0.021
S2	20-40	96.10±11.82	46.13±5.46	0.057±0.007	0.128±0.016	0.368±0.050
S3	40-60	117.11±13.62	55.23±6.24	0.068±0.008	0.156±0.018	0.477±0.059
S4	60-80	133.89±15.03	63.70±6.94	0.078±0.009	0.178±0.020	0.536±0.064
S5	0-20	144.83±16.22	70.70±7.64	0.087±0.009	0.192±0.022	0.494±0.061
S6	20-40	159.60±17.09	77.59±7.97	0.095±0.010	0.212±0.022	0.554±0.066
S7	40-60	204.32±23.06	99.12±10.80	0.122±0.013	0.271±0.031	0.709±0.087
S8	60-80	181.71±18.69	90.08±8.96	0.111±0.011	0.241±0.025	0.565±0.062
S9	0-20	126.89±14.01	69.48±6.59	0.085±0.008	0.168±0.019	0.466±0.058
S10	20-40	98.86±11.62	47.72±5.39	0.059±0.007	0.131±0.016	0.378±0.049
S11	40-60	81.40±9.54	39.32±4.41	0.048±0.005	0.108±0.013	0.325±0.043

Samples	Depths (cm)	Ra_{eq} ($Bqkg^{-1}$)	D ($nGyh^{-1}$)	E ($mSvy^{-1}$)	H_{ex} ($mSvy^{-1}$)	H_{in} ($mSvy^{-1}$)
S12	60-80	15.45±2.68	7.26±1.21	0.009±0.001	0.021±0.004	0.069±0.013
S13	0-20	138.33±16.80	66.80±7.91	0.082±0.010	0.184±0.022	0.480±0.062
S14	20-40	112.49±14.41	54.62±6.74	0.067±0.008	0.149±0.019	0.377±0.048
S15	40-60	73.55±12.18	35.14±5.54	0.043±0.007	0.098±0.016	0.255±0.050
S16	60-80	38.36±6.96	17.99±3.17	0.022±0.004	0.051±0.009	0.138±0.028
Limits [3]		370	55	0.460	1	1

The mean absorbed dose rate in dumpsite soils from different locations within Abeokuta was estimated by Bello and Farinre [7] as 55 $nGyh^{-1}$. This value was higher than the mean values obtained in Saje, Ita-Oshin and Premier, but lower than the mean value of Oke-Diya. Also, Odunaike et al. [24] obtained a mean absorbed dose rate of 36 $nGyh^{-1}$ for soils from a dumpsite in Abeokuta; this value was lower than the values obtained in this study. Again, Obed et al. [12] estimated a mean absorbed dose rate of 88 $nGyh^{-1}$; this value was higher than the mean absorbed doses obtained in this study. In dumpsites in Agbara and Port-Harcourt, mean absorbed doses of 62.4 and 52.49 $nGyh^{-1}$ were obtained, respectively [1, 26]; these values were higher than the mean values estimated for Saje, Ita-Oshin and Premier, but lower than the Oke-Diya values. The mean absorbed dose rates in dumpsites from Osogbo and Port-Harcourt were 28.80 and 31.98 $nGyh^{-1}$, respectively [19, 35]. These values were lower than the values obtained in this study. The mean absorbed dose rates estimated in this study were relatively high (especially for Oke-Diya results) compared to these similar studies.

4.2.3 Annual Effective Dose Equivalent (E)

The annual effective dose equivalents estimated ranged from 0.009±0.001 to 0.122±0.013 $mSvy^{-1}$. The minimum annual effective dose of 0.009 $mSvy^{-1}$ was obtained in Ita-Oshin sample S12 (depths of 60-80 cm), while the maximum annual effective dose of 0.122 $mSvy^{-1}$ was obtained in Oke-Diya sample S7 (depths of 40-60 cm). The mean annual effective dose equivalents obtained for Saje, Oke-Diya, Ita-Oshin and Premier samples were 56.7, 103.8, 50.2 and 53.5 μSvy^{-1}, respectively. These values were higher than the mean effective dose of 24.6 μSvy^{-1} obtained in samples from some selected dumpsites in Port-Harcourt, Rivers State, Nigeria by [9] and also higher than the mean annual effective dose of 36.0 μSvy^{-1} obtained in some dumpsites in Abeokuta, Ogun State, Nigeria [24], but lower than the annual effective dose of 80.0 μSvy^{-1} for the surface soil in some Southwestern cities of Nigeria [36], except for Oke-Diya study location with higher values. The high effective dose obtained in Oke-Diya may be due to its sedimentary terrain and the nature of the waste materials dumped on the site, which are mostly associated with industrial and domestic (household, animal bones and related wastes, charcoal, … and so on) wastes, as well as contraband goods and other market wastes which contain high amounts of potassium. In general, the average annual effective dose equivalents for all the representative soil samples were below the global average annual effective dose limit of 460 μSvy^{-1} and the study areas can then be considered to have permissible levels of background radiation.

4.2.4 External and Internal Hazard Indices

The external hazard index (H_{ex}) for the representative soil samples for Saje, Oke-Diya, Ita-Oshin and Premier ranged from 0.054±0.007-0.178±0.020, 0.192±0.022-0.271±0.031, 0.021±0.004-0.108±0.013 and 0.051±0.009-0.184±0.022 $mSvy^{-1}$, respectively. Also, the internal hazard index (H_{in}) ranged from 0.147±0.021-0.536±0.064, 0.494±0.061-0.709±0.087, 0.069±0.013-0.466±0.058 and 0.138±0.028-0.480±0.062 $mSvy^{-1}$ for Saje, Oke-Diya, Ita-Oshin and Premier, respectively. The external and internal hazard indices for all the representative samples were within the normal range, as they were all below unity and these low values were also obtained in similar studies by Sowole and Egunjobi [32], and Taqi et al. [37]. The external hazard index values of the soil samples were very low compared to the standard permissible limit of 1 $mSvy^{-1}$. Moreover, the internal hazard index values for Oke-Diya soil samples were relatively high compared to the other study areas; most of the values obtained were higher than 0.5 $mSvy^{-1}$.

5. Conclusion

The activity concentrations associated with ^{238}U and ^{232}Th natural decay chains and the long-lived naturally occurring radionuclide ^{40}K in sixteen representative soil samples collected from different depths into the soil profiles across the study areas were determined. Saje samples revealed an increase in the activity concentrations with depth, probably indicating leaching of the radionuclides into the subsurface. Oke-Diya samples revealed the highest concentrations of radionuclides, which may be due to geologic, hydro-geologic and anthropogenic effects. The radionuclide concentrations increased with depth, indicating the accumulation of these radionuclides at deeper depths. Ita-Oshin and Premier samples had their highest radionuclide concentrations at the surface depths and the radionuclide concentrations decreased with depth. The radionuclides had not leached into deeper depths of the subsurface and therefore may not pose much threat to soil and aquifer. Premier samples revealed low concentrations of the radionuclides when compared to the other study areas. The gamma absorbed dose rate, radium equivalent, external and internal hazard indices and annual effective dose equivalent for the complete set of samples were all below the recommended standards, except for the mean gamma absorbed dose rate of Oke-Diya samples. These parameters showed a radiation burden on the environment and the study areas could be regarded to have a relatively high level of natural background radiation which may increase overtime as the dumpsites age.

References

[1] Itota, G.O. and Balogun, A.O., Physical Science International Journal, 13(4) (2017) 1.

[2] Isinkaye, M.O. and Emelue, H.U., Journal of Radiation Research and Applied Sciences, 8 (2015) 459.

[3] United Nations Scientific Committee on the Effects of Atomic Radiation, "Sources and Effects of Ionizing Radiation", Report vol. 1 to the General Assembly, with scientific annexes, United Nations Sales Publication, United Nations, New York, (2000).

[4] Eisenbud, M. and Gesell, T.F., "Environmental Radioactivity", Fourth Edition, (San Diego: Academic Press, 1997).

[5] Bristow, Q., Carson, J.M., Darnley, A.G., Holroyd, M.T. and Richardson, K.A., Geological Survey of Canada, Open File No. 335, (1977).

[6] Murugesan, S., Mullainathan, S., Ramasamy, V. and Meenakshisundaram, V., Iranian Journal of Radiation Research, 8 (4) (2011) 211.

[7] Bello, R. and Farinre, O.Z., Physical Science International Journal, 5 (1) (2015) 51.

[8] Alaamer, A.S., Turkish Journal of Engineering and Environmental Sciences, 32 (2008) 229.

[9] Farai, I.P., Okwunakwe, C.E. and Makinde, O.S., Proceedings of the 16th International Conference on Radionuclide Metrology in Cape Town, Elsevier B.V: 850-854, (2007), June-July.

[10] Telford, W.M., Geldart, L.P. and Sheriff, R.E., "Applied Geophysics", 1st Edition, (Cambridge University Press, Cambridge, 1976), 65-115.

[11] Jibiri, N.N., Farai, I.P. and Alausa, S.K., Radiation and Environmental Biophysics, 46 (2007) 53.

[12] Obed, R.I., Farai, I.P. and Jibiri, N.N., Journal of Radiological Protection, 25 (2005) 305.

[13] Akinloye, M.K. and Olomo, J.B., Nigerian Journal of Physics, 17S (2005) 219.

[14] Farai, I.P., "Atomic Energy: The Myth and the Truth", An inaugural lecture delivered at the University of Ibadan, Ibadan University Press, (2011), 100-110.

[15] Brevik, E.C., Slaughter, L., Singh, B.R., Steffan, J.J., Collier, D., Barnhart, P. and Pereira, P., Air, Soil and Water Research, 13 (2020) 1.

[16] Raghu, Y., Ravisankar, R., Chandrasekaran, A., Vijayagopal, P. and Venkatraman, B., Journal of Taibah University for Science, 11 (2017) 523.

[17] Alzubaidi, G., Hamid, F.B.S. and Abdul Rahman, I., The Scientific World Journal, 2016 (2016) 6178103.

[18] Otwoma, D., Patel, J.P., Bartilo, S. and Mustapha, A.O., XI Radiation Physics & Protection Conference, Nasr City-Cairo, Egypt, (2012), June 25-28.

[19] Ehirim, C.N. and Itota, G.O., Journal of Environmental Science, Toxicology and Food Technology, 2 (5) (2013) 35.

[20] Princeton, Gamma-Tech., "P-type HPGe Detectors", Available at: http://www.pgt.com/nuclear/ptype.html (2018), December 20.

[21] Knoll, G.F., "Radiation Detection and Measurements", Third Edition, (New York: John Wiley & Sons, Inc., 2000), ISBN: 0-471-07338-5.

[22] Farai, I.P. and Vincent, U.E., Nigerian Journal of Physics, 18 (1) (2006) 121.

[23] Jibiri, N.N. and Farai, I.P., Radioprotection, 40 (4) (2005) 489.

[24] Odunaike, R.K., Alausa, S.K., Fasunwon, O.O., Orunsolu, B.A. and Ijeoma, G.C., Research Journal of Environmental Science, 3(2) (2009) 262.

[25] El-Taher, A. and Makhluf, S., Indian Journal of Pure and Applied Physics, 48 (2010) 697.

[26] Ademola, A.K., Olaoye, M.A. and Abodunrin, P.O., Journal of Radiation Research and Applied Sciences, 8 (2015) 148.

[27] Saleh, M.A., Ramli, A.T., Alajerami, Y. and Aliyu, A.S., Journal of Ovonic Research, 9 (2013) 17.

[28] International Atomic Energy Agency, "Almera Proficiency Test on the Determination of Radionuclides in Spinach, Soil and Water", IAEA-CU-2007-04, Analytical Quality in Nuclear Applications, No. IAEA/AQ/3, (2009).

[29] Farai, I.P. and Ademola, J.A., Journal of Environmental Radioactivity, 79 (2005) 119.

[30] Valentin, J., "The Recommendations of the International Commission on Radiological Protection in ICRP 103", (Elsevier Science Publishers, 2007), 100p.

[31] Ajayi, O.S. and Ibikunle, S.B, International Journal of Radiation Research, 11 (4) (2013) 271.

[32] Sowole, S. and Egunjobi, K.A., Tanzania Journal of Science, 45(3) (2019) 307.

[33] Mittal, S., Rani, A., Mehra, R. and Ramola, R.C., Radiation Effects and Defects in Solids, 173 (7-8) (2018)673.

[34] Kapanadze, K., Magalashvili, A. and Imnadze, P., Heliyon, 5 (2019) e01377.

[35] Bamidele, L. and Olatunji, K.O., Nigerian Journal of Physics, 25(1) (2014) 68.

[36] Arogunjo, A.M., Journal of Applied Sciences, 7 (11) (2007) 1534.

[37] Taqi, A.H., Shaker, A.M. and Battawy, A.A., International Journal of Radiation Research, 16 (4) (2018) 455.

Volume 15, Number 4, 2022. pp. 393-402

Jordan Journal of Physics

ARTICLE

Solutions of the N-dimensional Klein-Gordon Equation with Ultra Generalized Exponential–Hyperbolic Potential to Predict the Mass Spectra of Heavy Mesons

Joseph E. Ntibi[b], **Etido P. Inyang**[a], **Ephraim P. Inyang**[b], **Eddy S. William**[b] and **Etebong E. Ibekwe**[c]

[a] *Department of Physics, National Open University of Nigeria, Jabi, Abuja, Nigeria.*

[b] *Theoretical Physics Group, Department of Physics, University of Calabar, P.M.B 1115 Calabar, Nigeria.*

[c] *Department of Physics, Akwa Ibom State University, Ikot Akpaden, P.M.B 1167, Uyo, Nigeria.*

Doi: **https://doi.org/10.47011/15.4.8**

Received on: 06/02/2021; *Accepted on: 12/04/2021*

Abstract: We solved the N-dimensional Klein-Gordon equation analytically using the Nikiforov-Uvarov method to obtain the energy eigenvalues and the corresponding wave function in terms of Laguerre polynomials with the ultra generalized exponential–hyperbolic potential. The present results are applied for calculating the mass spectra of heavy mesons, such as charmonium ($c\bar{c}$) and bottomonium ($b\bar{b}$), for different quantum states. The present work provides excellent results in comparison with experimental data with a maximum error of $0.0059GeV$ and the works of other researchers.

Keywords: Ultra generalized exponential–hyperbolic potential, Klein-Gordon equation, Heavy mesons, Nikiforov-Uvarov method.

1. Introduction

The solution of the spectral problem for the Klein-Gordon equation with spherically symmetric potentials is of major concern in describing the spectra of heavy mesons. Potential models offer a good description of the mass spectra of quarkonium systems, such as bottomonium and charmonium [1-5]. In simulating the interaction for these systems, confining-type potentials are generally used. The holding potential is the Cornell potential with two terms, one of which is responsible for the Coulomb interaction of quarks and the other corresponds to the confinement of the quark [6]. Although this potential, proposed to describe quarkonia with heavy quarks, has been used for a long time, nevertheless the problem of finding the inter-quark potential with exponential-type potential still remains incompletely solved. In recent times, the solutions of the Schrödinger equation (SE) and Klein-Gordon equation (KGE) under the quarkonium interaction potential model, such as the Cornell or the Killingbeck potential, have attracted much interest of researchers [7-15]. The KGE with some potential can be solved exactly for $l = 0$, but is insolvable for any arbitrary angular momentum quantum number $l \neq 0$. In this case, several approximate techniques are employed in obtaining the solution. For instance, such techniques include, asymptotic iteration method (AIM) [16] Laplace transformation method [17], the Nikiforov-Uvarov functional analysis (NUFA) method [18-20], the Nikiforov-Uvarov(NU) method [21-34],

Corresponding Author: E. P. Inyang **Email**: etidophysics@gmail.com

the series expansion method (SEM) [35-37], WKB approximation [38], among others [39].

Various exponential-type potentials have been studied by many researchers, such as Hellmann plus Hulthen potential [40], Kratzer plus screened Coulomb potential [25], Yukawa potential [41], Hellmann plus Eckart potential [29] and many more. The trigonometric hyperbolic potential plays a vital role in atomic and molecular physics, since it can be used to model inter-atomic and inter-molecular forces [42, 43].

The ultra generalized exponential –hyperbolic potential (UGEHP) takes the form [44]:

$$V(r) = \frac{ae^{-4\alpha r}+be^{-2\alpha r}}{r^2} + \frac{ce^{-2\alpha r}-dCosh(\eta\alpha r)e^{-\alpha r}+gCosech\alpha r e^{\alpha r}}{r} + f, \quad (1)$$

where $a, b, c, d, \eta, g \text{ and } f$ are potential strengths and α is the screening parameter. When $\eta = 1$, then:

$$\left.\begin{aligned} Cosh\alpha r &= \frac{e^{\alpha r}+e^{-\alpha r}}{2} \\ \text{Cosech}\,\alpha r &= \frac{2}{e^{\alpha r}-e^{-\alpha r}} \end{aligned}\right\}. \quad (2)$$

We carry out a series expansion of the exponential terms in Eqs. (1) and (2) up to order three, in order to model the potential to interact in the quark-antiquark system and substitute the results into Eq. (1), which yields:

$$V(r) = \frac{\beta_0}{r^2} - \frac{\beta_1}{r} + \beta_2 r - \beta_3 r^2 + \beta_4, \quad (3)$$

where

$$\left.\begin{aligned} \beta_0 &= a + b, \\ \beta_1 &= 4a\alpha + 2b\alpha + d - g, \\ \beta_2 &= 2c\alpha^2 + \alpha d \\ \beta_3 &= \alpha(d - g), \\ \beta_4 &= 8a\alpha^2 + 2b\alpha^2 - 2c\alpha - \alpha d + g\alpha + f \end{aligned}\right\}. \quad (4)$$

The third term of Eq. (3) is a linear term for confinement feature and the second term is the Coulomb potential that describes the short distance between quarks.

Researchers in recent times have obtained the mass spectrum of the quarkonium systems using different techniques [45-47]. For instance, Inyang et al. [45] examined heavy quarkonia characteristics in the general framework of SE with extended Cornell potential using the exact quantization rule. Furthermore, Omugbe et al. [39] obtained the heavy and heavy-light spectra in non-relativistic regime with Killingbeck potential plus an inversely quadratic potential model using the WKB method. In addition, Inyang et al. [46] obtained the Klein-Gordon equation solutions for the Yukawa potential using the Nikiforov-Uvarov method. The energy eigenvalues were obtained both in relativistic and non-relativistic regimes. The results were applied to calculate heavy-meson masses. Therefore, in this present work, we aim at studying the KGE with the ultra generalized exponential –hyperbolic potential (UGEHP) using the NU method to obtain the mass spectra of heavy mesons, such as charmonium $(c\bar{c})$ and bottomonium $(b\bar{b})$. To the best of our knowledge, this study is not in literature. The study will be carried out in threefold. We will first model the potential to interact in the quark-antiquark system, thereafter we solved the model potential with KGE using the NU method and finally, the mass spectra are calculated.

2. Bound State Solution of the Klein-Gordon Equation with the Ultra Generalized Exponential – Hyperbolic Potential (UGEHP)

The Klein-Gordon equation for a spinless particle for $\hbar = c = 1$ in N dimensions is given as [46]:

$$\left[-\nabla^2 + (M + S(r))^2 + \frac{(N+2l-1)(N+2l-3)}{4r^2}\right]\psi(r,\theta,\varphi) = [E_{nl} - V(r)]^2\psi(r,\theta,\varphi) \quad (5)$$

where ∇^2 is the Laplacian, M is the reduced mass, E_{nl} is the energy spectrum, n and l are the radial and orbital angular momentum quantum numbers, respectively. It is well known that for the wave function to satisfy the boundary conditions, it can be rewritten as:

$$\psi(r,\theta,\varphi) = \frac{R_{nl}}{r} Y_{lm}(\theta,\varphi). \quad (6)$$

The angular component of the wave function could be separated leaving only the radial part as shown below:

$$\frac{d^2R(r)}{dr^2}+\left[\left(E_{nl}^2-M^2\right)+V^2(r)-S^2(r)-2(E_{nl}V(r)+MS(r))-\frac{(N+2l-1)(N+2l-3)}{4r^2}\right]R(r)=0\,. \quad (7)$$

Thus, for equal vector and scalar potentials $V(r)=S(r)=2V(r)$, Eq. (7) becomes:

$$\frac{d^2R(r)}{dr^2}+\left[\left(E_{nl}^2-M^2\right)-2V(r)(E_{nl}+M)-\frac{(N+2l-1)(N+2l-3)}{4r^2}\right]R(r)=0\,. \quad (8)$$

Upon substituting Eq. (3) into Eq. (8), we obtain:

$$\frac{d^2R(r)}{dr^2}+\left[\begin{array}{c}\left(E_{nl}^2-M^2\right)+\\ \left(-\frac{2\beta_0}{r^2}+\frac{2\beta_1}{r}-2\beta_2 r\right)(E_{nl}+M)\\ +2\beta_3 r^2-2\beta_4\\ -\frac{(N+2l-1)(N+2l-3)}{4r^2}\end{array}\right]R(r)=0. \quad (9)$$

In order to transform the coordinate from r to x in Eq. (9), we set**:**

$$x=\frac{1}{r}\ . \quad (10)$$

This implies that the 2nd derivative in Eq. (10) becomes:

$$\frac{d^2R(\mathrm{r})}{dr^2}=2x^3\frac{dR(\mathrm{x})}{dx}+x^4\frac{d^2R(\mathrm{x})}{dx^2}\ . \quad (11)$$

Substituting Eqs. (10) and (11) into Eq. (9), we obtain**:**

$$\frac{d^2R(x)}{dx^2}+\frac{2}{x}\frac{dR}{dx}+\frac{1}{x^4}\left[\begin{array}{c}\left(E_{nl}^2-M^2\right)+\\ \left(-2\beta_0x^2+2\beta_1x\right.\\ \left.-\frac{2\beta_2}{x}+\frac{2\beta_3}{x^2}-2\beta_4\right)(E_{nl}+M)\\ -\frac{(N+2l-1)(N+2l-3)x^2}{4}\end{array}\right]R(x)=0\,. \quad (12)$$

Next, we propose the following approximation scheme on the term $\frac{\beta_2}{x}$ and $\frac{\beta_3}{x^2}$.

Let us assume that there is a characteristic radius r_0 of the meson. Then, the scheme is based on the expansion of $\frac{\beta_2}{x}$ and $\frac{\beta_3}{x^2}$ in a power series around r_0; i.e., around $\delta\equiv\frac{1}{r_0}$, in the x-space up to the second order. This is similar to Pekeris approximation, which helps deform the centrifugal term such that the potential can be solved by the NU method [47].

Setting $y=x-\delta$ and around $y=0$, it can be expanded into a series of powers as:

$$\frac{\beta_2}{x}=\frac{\beta_2}{y+\delta}=\frac{\beta_2}{\delta\left(1+\frac{y}{\delta}\right)}=\frac{\beta_2}{\delta}\left(1+\frac{y}{\delta}\right)^{-1} \quad (13)$$

which yields:

$$\frac{\beta_2}{x}=\beta_2\left(\frac{3}{\delta}-\frac{3x}{\delta^2}+\frac{x^2}{\delta^3}\right). \quad (14)$$

Similarly,

$$\frac{\beta_3}{x^2}=\beta_3\left(\frac{6}{\delta^2}-\frac{8x}{\delta^3}+\frac{3x^2}{\delta^4}\right). \quad (15)$$

By substituting Eqs. (14) and (15) into Eq. (12), we obtain:

$$\frac{d^2R(x)}{dx^2}+\frac{2x}{x^2}\frac{dR(x)}{dx}+\frac{1}{x^4}\left[-\varepsilon+\beta x-\gamma x^2\right]R(x)=0 \quad (16)$$

where

$$\left.\begin{array}{l}-\varepsilon=\left(\begin{array}{c}\left(E_{nl}^2-M^2\right)-\frac{6\beta_2}{\delta}(E_{nl}+M)\\ +\frac{12\beta_3}{\delta^2}(E_{nl}+M)-2\beta_4(E_{nl}+M)\end{array}\right)\\ \beta=\left(\begin{array}{c}2\beta_1(E_{nl}+M)+\frac{6\beta_2}{\delta^2}(E_{nl}+M)\\ -\frac{16\beta_3}{\delta^3}(E_{nl}+M)\end{array}\right)\\ \gamma=\left(\begin{array}{c}2\beta_0(E_{nl}+M)+\frac{2\beta_2}{\delta^3}(E_{nl}+M)\\ -\frac{6\beta_3}{\delta^4}(E_{nl}+M)+\frac{(N+2l-1)(N+2l-3)}{4}\end{array}\right)\end{array}\right\}. \quad (17)$$

Comparing Eq. (16) and Eq. (A1), we obtain:

$$\left.\begin{array}{l}\tilde{\tau}(\mathrm{x})=2x,\ \sigma(\mathrm{x})=x^2\\ \tilde{\sigma}(\mathrm{x})=-\varepsilon+\beta x-\gamma x^2\\ \sigma'(\mathrm{x})=2x,\ \sigma''(\mathrm{x})=2\end{array}\right\}. \quad (18)$$

We substitute Eq. (18) into Eq. (A9) to obtain:

$$\pi(\mathrm{x})=\pm\sqrt{\varepsilon-\beta x+\left(\gamma+k\right)x^2}\ . \quad (19)$$

To determine k, we take the discriminant of the function under the square root, which yields:

$$k = \frac{\beta^2 - 4\gamma\varepsilon}{4\varepsilon} \quad . \tag{20}$$

We substitute Eq. (20) into Eq. (19) and have:

$$\pi(x) = \pm\left(\frac{\beta x}{2\sqrt{\varepsilon}} - \frac{\varepsilon}{\sqrt{\varepsilon}}\right). \tag{21}$$

For a physically acceptable solution, we take the negative part of Eq. (21) which is required for bound-state problems and differentiate. This yields:

$$\pi'_{-}(\mathrm{x}) = -\frac{\beta}{2\sqrt{\varepsilon}}. \tag{22}$$

By substituting Eqs. (18) and (22) into Eq. (A7), we have:

$$\tau(\mathrm{x}) = 2x - \frac{\beta x}{\sqrt{\varepsilon}} + \frac{2\varepsilon}{\sqrt{\varepsilon}} \quad . \tag{23}$$

Differentiating Eq. (23). we have:

$$\tau'(\mathrm{x}) = 2 - \frac{\beta}{\sqrt{\varepsilon}}. \tag{24}$$

By using Eq. (A10), we obtain:

$$\lambda = \frac{\beta^2 - 4\gamma\varepsilon}{4\varepsilon} - \frac{\beta}{2\sqrt{\varepsilon}}. \tag{25}$$

And using Eq. (A11), we obtain:

$$\lambda_n = \frac{n\beta}{\sqrt{\varepsilon}} - n^2 - n. \tag{26}$$

Equating Eqs. (25) and (26) and substituting Eqs. (4) and (17) yield the energy eigenvalue equation of the UGEHP in the relativistic limit as:

$$\begin{aligned} M^2 - E_{nl}^2 &= \tfrac{6(2c\alpha^2+\alpha d)}{\delta}(E_{nl}+M) \\ &\quad - \tfrac{12\alpha(d-g)}{\delta^2}(E_{nl}+M) \\ &\quad + 2\begin{pmatrix} 8a\alpha^2 + 2b\alpha^2 - 2c\alpha \\ -\alpha d + g\alpha + f \end{pmatrix}(E_{nl}+M) \\ &\quad + \frac{1}{4}\left[\frac{\begin{matrix} 2(4a\alpha+2b\alpha+d-g)(E_{nl}+M) \\ +\frac{6(2c\alpha^2+\alpha d)(E_{nl}+M)}{\delta^2} - \frac{16\alpha(d-g)(E_{nl}+M)}{\delta^3} \end{matrix}}{n+\frac{1}{2}+\sqrt{\begin{matrix} \frac{1}{4} - 2(a+b)(E_{nl}+M) + \frac{2(2c\alpha^2+\alpha d)}{\delta^3}(E_{nl}+M) \\ -\frac{6\alpha(d-g)}{\delta^4}(E_{nl}+M) + \frac{(N+2l-1)(N+2l-3)}{4} \end{matrix}}}\right]^2. \end{aligned} \tag{27}$$

2.1 Non-relativistic Limit

In this sub-section, we consider the non-relativistic limit of Eq. (27). Considering a transformation of the form: $M + E_{nl} \to \frac{2\mu}{\hbar^2}$ and $M - E_{nl} \to -E_{nl}$, where μ is the reduced mass, and substituting it into Eq. (27), we have the non-relativistic energy eigenvalue equation as:

$$\begin{aligned} E_{nl} &= \tfrac{12\alpha(d-g)}{\delta^2} - \tfrac{6(2c\alpha^2-\alpha d)}{\delta} \\ &\quad -2(8a\alpha + 2b\alpha^2 - 2c\alpha - \alpha d + \alpha g + f) \\ &\quad -\frac{\hbar^2}{8\mu}\left[\frac{\begin{matrix} \frac{4\mu}{\hbar^2}(4a\alpha+2b\alpha+d-g) \\ +\frac{12\mu}{\delta^2\hbar^2}(2c\alpha^2+\alpha d) - \frac{32\mu\alpha}{\delta^3\hbar^2}(d-g) \end{matrix}}{n+\frac{1}{2}+\sqrt{\begin{matrix} \frac{1}{4} - \frac{4\mu}{\hbar^2}(a+b) + \frac{4\mu}{\delta^3\hbar^2}(2c\alpha^2+\alpha d) - \frac{12\mu\alpha}{\delta^4\hbar^2}(d-g) \\ +\frac{(N+2l-1)(N+2l-3)}{4} \end{matrix}}}\right]^2. \end{aligned} \tag{28}$$

The unnormalized wave function in terms of Laguerre polynomials is given as:

$$\psi(\mathrm{s}) = B_{nl}\, s^{-\frac{\alpha_1}{2\sqrt{\varepsilon}}} e^{-\frac{\varepsilon}{s\sqrt{\varepsilon}}} L_n^{\frac{\alpha_1}{\sqrt{\varepsilon}}}\left(\frac{2\varepsilon}{s\sqrt{\varepsilon}}\right), \tag{29}$$

where L_n is the associated Laguerre polynomials and B_{nl} is the normalization constant, which can be obtained from:

$$\int_0^\infty |\,\mathrm{B}_{nl}(r)\,|^2 dr = 1 \tag{30}$$

3. Results and Discussion

3.1 Results

We calculate the mass spectra of the heavy quarkonium system, such as charmonium and bottomonium, in 3-dimensional space ($N = 3$) that have the quark and anti-quark flavors, using the following relation [48]:

$$M = 2m + E_{nl}^{N=3}, \tag{31}$$

where m is the quarkonium bare mass and $E_{nl}^{N=3}$ stands for the energy eigenvalues. By substituting Eq. (28) into Eq. (31), we obtain the mass spectra for UGEHP as:

$$M = 2m + \frac{12\alpha(d-g)}{\delta^2} - \frac{6\left(2c\alpha^2-\alpha d\right)}{\delta} - 2(8a\alpha + 2b\alpha^2 - 2c\alpha - \alpha d + \alpha g + f) - \frac{\hbar^2}{8\mu}\left[\frac{\frac{4\mu}{\hbar^2}(4a\alpha+2b\alpha+d-g) + \frac{12\mu}{\delta^2\hbar^2}(2c\alpha^2+\alpha d) - \frac{32\mu\alpha}{\delta^3\hbar^2}(d-g)}{n+\frac{1}{2}+\sqrt{\frac{1}{4}-\frac{4\mu}{\hbar^2}(a+b)+\frac{4\mu}{\delta^3\hbar^2}(2c\alpha^2+\alpha d)-\frac{12\mu\alpha}{\delta^4\hbar^2}(d-g) + \frac{(N+2l-1)(N+2l-3)}{4}}}\right]^2. \quad (32)$$

3.2 Discussion of Results

We calculate the mass spectra of charmonium and bottomonium for states from 1S, 2S, 1P, 2P, 3S, 4S, 1D, 2D, and 1F, by using Eq. (32). The free parameters of Eq. (32) were then obtained by solving two algebraic equations by inserting experimental data of mass spectra for $2S, 2P$ in the case of charmonium. In the case of bottomonium, the values of the free parameters in Eq. (32) are calculated by solving two algebraic equations, which were obtained by inserting experimental data of mass spectra for $1S, 2S$.

The experimental data was taken from [49]. For bottomonium $b\bar{b}$ and charmonium $c\bar{c}$ systems, we adopt the numerical values of these masses as $m_b = 4.823\,GeV$ and $m_c = 1.209\,GeV$ [50]. Then, the corresponding reduced masses are $\mu_b = 2.4115\,GeV$ and $\mu_c = 0.6045\,GeV$, respectively. We note that the calculations of mass spectra of charmonium and bottomonium are in good agreement with experimental data and works of other researchers, in Refs. [7, 48] as presented in Tables 1 and 2. In order to test for the accuracy of the predicted results determined numerically, we used a Chi-squared function to determine the error between the experimental data and the theoretically predicted values. The maximum error in comparison with the experimental data is found to be $0.0059\,GeV$. We plotted the variation of mass spectra energy with respect to potential strengths, reduced mass (μ) and screening parameter (α), respectively. In Figs. 1 and 2, the mass spectra energy increases as the potential strength increases for different quantum numbers. In Fig. 3, it is observed that the mass spectra energy decreases exponentially as the reduced mass increases for various angular quantum numbers; a divergence is noticed when $\alpha = 0.1$. Finally, an increase in mass spectra energy is observed as the screening parameter increases.

TABLE 1. Mass spectra of charmonium in (GeV).

$$\left(\begin{array}{c} a = -22.17885GeV, \quad b = 13.73217GeV, \quad c = 10.73524GeV^2, \\ d = 3.010241GeV^{-1}, \quad g = 10.64213, \quad f = 0.05GeV^3, \\ \alpha = 0.01, \quad \delta = 1.00252GeV, \ m_c = 1.209GeV, \quad N = 3, \quad \hbar = 1, \quad \mu = 0.6045GeV \end{array}\right)$$

State	Present work	[7]	[48]	Experiment [49]
1S	3.096	3.096	3.096	3.096
2S	3.686	3.686	3.672	3.686
1P	3.526	3.255	3.521	3.525
2P	3.767	3.779	3.951	3.773
3S	4.040	4.040	4.085	4.040
4S	4.262	4.269	4.433	4.263
1D	3.768	3.504	3.800	3.770
2D	4.034	-	-	4.159
1F	4.162	-	-	-

TABLE 2. Mass spectra of bottomonium in (GeV).

$$\begin{pmatrix} a=-20.99857GeV, & b=13.6254385GeV, & c=13.73524GeV^2, \\ d=4.110240GeV^{-1}, & g=11.542130, & f=0.05GeV^3, \\ \alpha=0.01, \delta=1.00252GeV, m_c=4.823GeV, N=3, \hbar=1, \mu=2.4115GeV & & \end{pmatrix}$$

State	Present work	[7]	[48]	Experiment[49]
1S	9.460	9.460	9.4620	9.460
2S	10.023	10.023	10.027	10.023
1P	9.761	9.619	9.9630	9.899
2P	10.261	10.114	10.299	10.260
3S	10.355	10.355	10.361	10.355
4S	10.579	10.567	10.624	10.580
1D	9.998	9.864	10.209	10.164
2D	10.206	-	-	-
1F	10.109	-	-	-

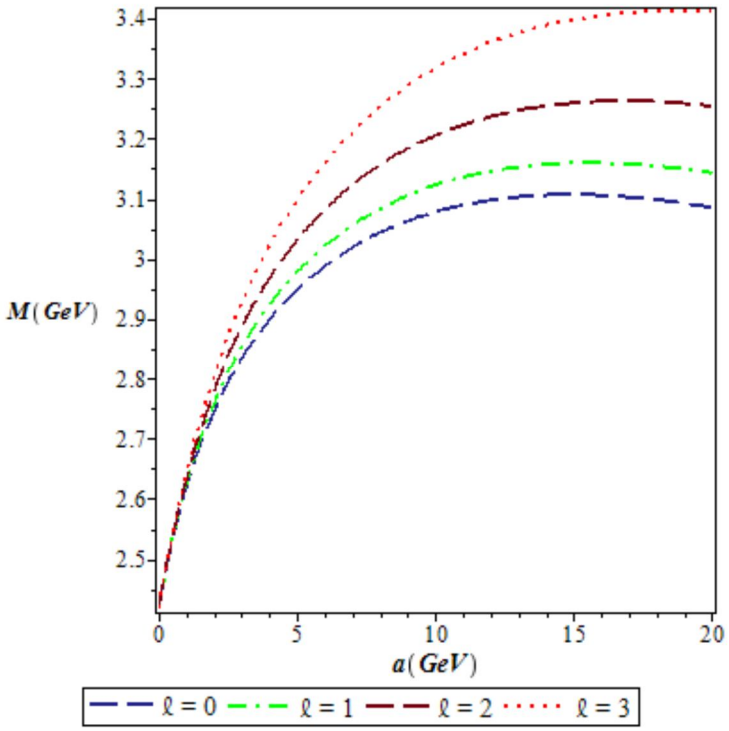

FIG. 1. Variation of mass spectra with potential strength (a) for different quantum numbers.

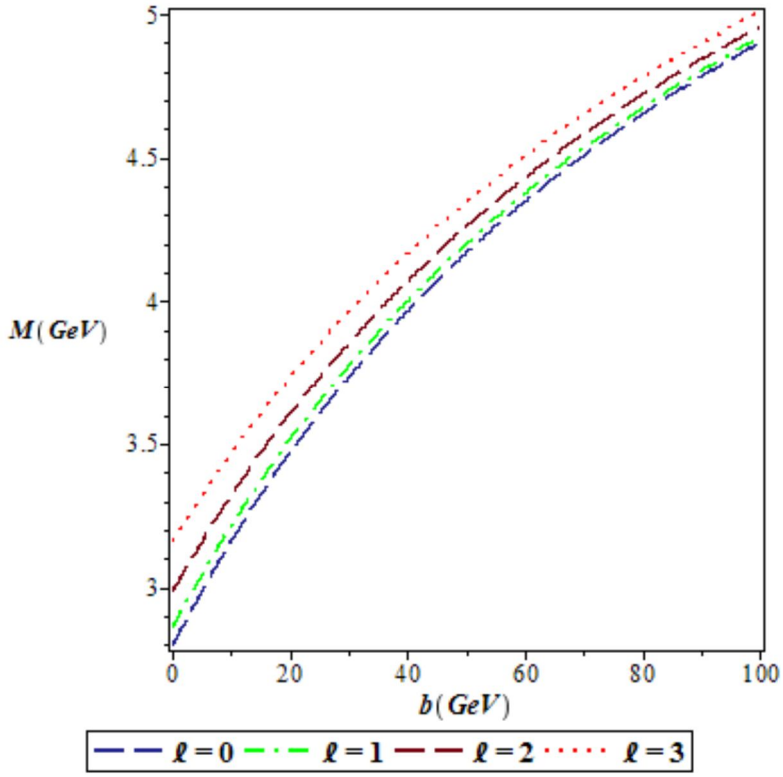

FIG. 2. Variation of mass spectra with potential strength (b) for different quantum numbers.

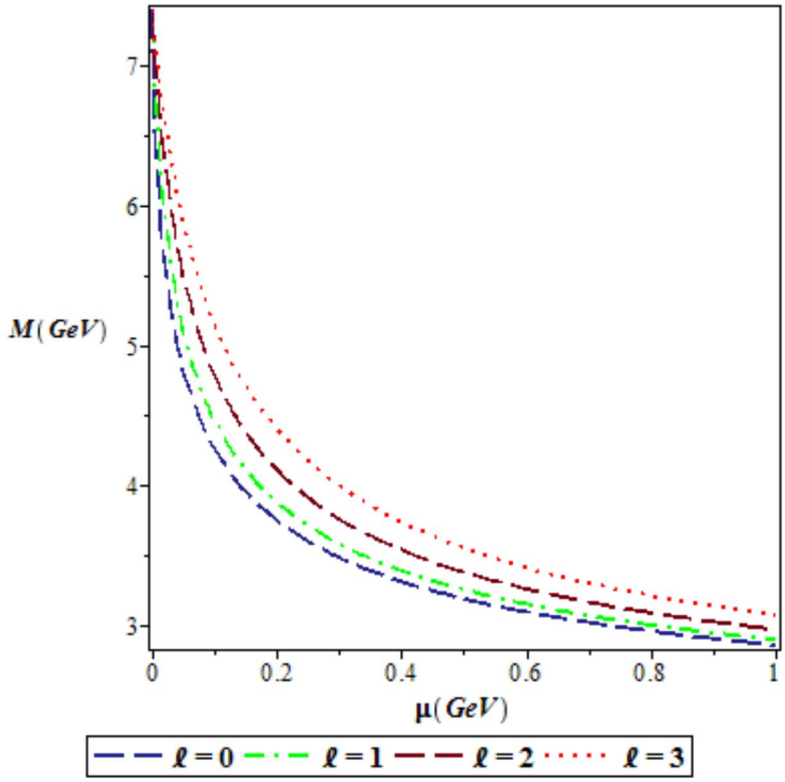

FIG. 3. Variation of mass spectra with reduced mass (μ) for different quantum numbers.

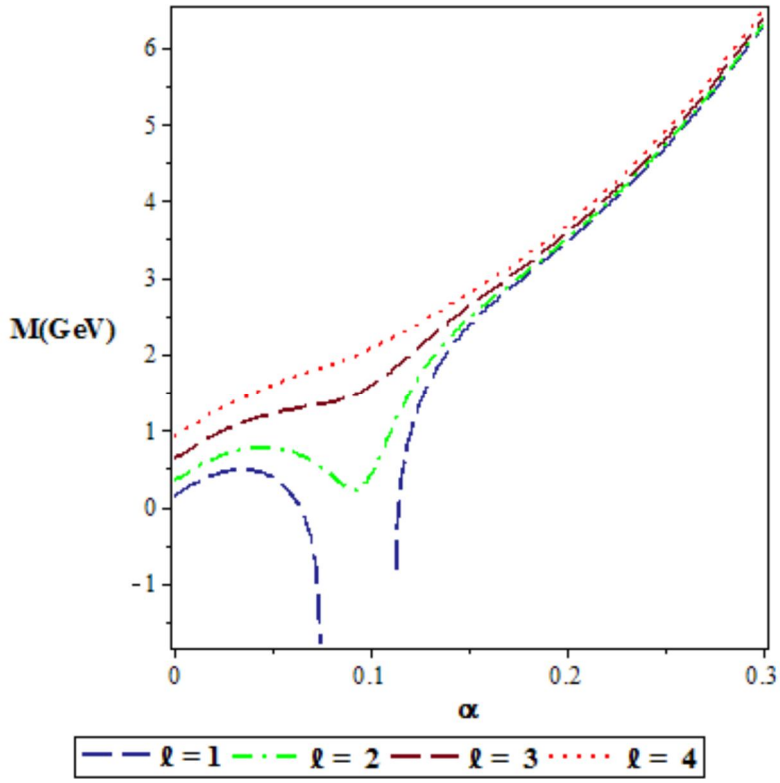

FIG. 4. Variation of mass spectra with screening parameter (α) for different quantum numbers.

4. Conclusion

In this study, we model the adopted ultra generalized exponential–hyperbolic potential to interact in quark-antiquark system. We obtained the approximate solutions of the KGE for energy eigenvalues and unnormalized wave function using the NU method. We applied the present results to compute heavy-meson masses of charmonium and bottomonium for different quantum states. The results agreed with experimental data, with a maximum error of $0.0059\,GeV$, and works of other researchers. Mass spectra variation with potential strengths, reduced mass (μ) and screening parameter (α) were plotted and discussed.

APPENDIX A: Review of Nikiforov-Uvarov (NU) method

The NU method was proposed by Nikiforov and Uvarov [51] to transform Schrödinger-like equations into a second-order differential equation *via* a coordinate transformation $x = x(r)$, of the form:

$$\psi''(x)+\frac{\tilde{\tau}(x)}{\sigma(x)}\psi'(s)+\frac{\tilde{\sigma}(x)}{\sigma^2(x)}\psi(x)=0 \quad \text{(A1)}$$

where $\tilde{\sigma}(x)$ and $\sigma(x)$ are polynomials, at most second-degree, and $\tilde{\tau}(x)$ is a first-degree polynomial. The exact solution of Eq. (A1) can be obtained by using the transformation:

$$\psi(x)=\phi(x)y(x). \quad \text{(A2)}$$

This transformation reduces Eq. (A1) into a hypergeometric-type equation of the form:

$$\sigma(x)y''(x)+\tau(x)y'(x)+\lambda y(x)=0 \quad \text{(A3)}$$

The function $\phi(x)$ can be defined as the logarithm derivative:

$$\frac{\phi'(x)}{\phi(x)}=\frac{\pi(x)}{\sigma(x)}, \quad \text{(A4)}$$

with $\pi(x)$ being at most a first-degree polynomial. The second part of $\psi(x)$ being $y(x)$ in Eq. (A2) is the hypergeometric function with its polynomial solution given by Rodrigues relation as:

$$y(x)=\frac{B_{nl}}{\rho(x)}\frac{d^n}{dx^n}\left[\sigma^n(x)\rho(x)\right] \quad \text{(A5)}$$

where B_{nl} is the normalization constant and $\rho(x)$ the weight function which satisfies the condition below:

$$\left(\sigma(x)\rho(x)\right)' = \tau(x)\rho(x) \tag{A6}$$

where also:

$$\tau(x) = \tilde{\tau}(x) + 2\pi(x). \tag{A7}$$

For bound solutions, it is required that:

$$\tau'(x) < 0. \tag{A8}$$

The eigenfunctions and eigenvalues can be obtained using the definition of the following function $\pi(x)$ and parameter λ, respectively:

$$\pi(x) = \frac{\sigma'(x)-\tilde{\tau}(x)}{2} \pm \sqrt{\left(\frac{\sigma'(x)-\tilde{\tau}(x)}{2}\right)^2 - \tilde{\sigma}(x) + k\sigma(x)} \tag{A9}$$

and

$$\lambda = k_- + \pi_-'(x). \tag{A10}$$

The value of k can be obtained by setting the discriminant in the square root in Eq. (A9) equal to zero. As such, the new eigenvalues equation can be given as:

$$\lambda + n\tau'(x) + \frac{n(n-1)}{2}\sigma''(x) = 0, (n = 0,1,2,\dots). \tag{A11}$$

References

[1] Kumar, R. and Chand, F., Commun. Theore. Phys., 59 (2013) 456.

[2] Mutuk, H., Advan. in High Energy Phys., 20 (2018) 653.

[3] Inyang, E.P., Iwuji, P.C., Ntibi, J.E., Omugbe, E., Ibanga, E.A. and William, E.S., East Eur. J. Phys., 2 (2022) 51.

[4] Omugbe, E., Osafile, O.E., Okon, I.B., Inyang, E.P., William, E.S. and Jahanshir, A., Few-Body Syst., 63 (2022) 7.

[5] Inyang,E.P. Obisung,E.O.,Iwuji, P.C., Ntibi, J.E., Amajama, J. and William, E.S.,J.Nig.Soc.Phys.Sci., 4(2022)884.

[6] Mocsy, A., The Euro. Phys. J., 61 (2009) 705.

[7] Ciftci, H. and Kisoglu, H.F., Adv. High Energy Phys., 45 (2018) 497.

[8] Abu-Shady, M., Abdel-Karim, T.A. and Khokha, E.M., J. of Quantum Phys., 45 (2018) 567.

[9] Hall, R.L. and Saad, N., Open Phys., 13 (2015) 23.

[10] Abu-Shady, M. and Ikot, A.N., The Euro. Phys. J., 54 (2019) 134.

[11] Al-Jamel, A., Int. J. Mod. Physics, 34 (2019) 242.

[12] Mansour, H. and Gamal, A., Adv. High Ener. Phys., 65 (2018) 1234.

[13] Al-Oun, A., Al-Jamel, A. and Widyan, H., Jordan. J. Phys., 8 (4) (2015) 199.

[14] Abu-Shady, M., Int. J. Appl. Math. Theor. Phys., 2 (2016) 16.

[15] Vega, A. and Flores, J., Pramana J. Phys., 87 (2016) 73.

[16] Edet, C.O., Mahmoud, S., Inyang, E.P., Ali, N. S . , Aljunid, A., Endut, R., Ikot, A.N. and Asjad ,M., Mathematics., 10, (2022) 2824.

[17] Al-Jamel, A. and Widyan, H., Appl. Phys. Research, 4 (2012) 57.

[18] Ikot, A.N., Okorie, U.S. Amadi, P.O. Edet, C.O., Rampho, G.J. and Sever, R., Few-Body Syst., 62 (2021) 9.

[19] Inyang , E.P., William, E.S. Ntibi, J.E., Obu, J.A., Iwuji, P.C. and Inyang, E.P., Can. J. Phys., 100 (10) (2022) 473.

[20] Inyang, E.P., William, E.S., Omugbe, E. et al., Revista Mexicana de Fisica, 68 (2022) 14.

[21] Okoi, P.O., Edet, C.O., Magu, T.O. and Inyang, E.P., Jordan J. Phys., 15 (2022) 148.

[22] Inyang, E.P. and Obisung, E.O., East Eur. J. Phys., 3 (2022) 32.

[23] William, E.S., Inyang, E.P., Akpan, I.O., Obu, J.A., Nwachukwu, A.N. and Inyang, E.P., Indian J. Phys., 96 (2022) 3461.

[24] Inyang, E.P., Ayedun, F., Ibanga, E.A. et al., Results in Physics, 43 (2022) 106075.

[25] Edet, C.O., Okorie, U.S., Ngiangia, A.T. and Ikot, A.N., Indian J. Phys., 94 (2020) 423.

[26] Okoi, P.O., Edet, C.O. and Magu, T.O., Rev. Mex. Fis., 66 (2020) 6.

[27] Inyang, E.P., Ikot, A.N., Inyang, E.P., Akpan, I.O., Ntibi, J.E., Omugbe, E. and William, E.S., Result in Physics, 43 (2022) 105754.

[28] Inyang, E.P., Inyang, E.P., William, E.S. and Ibekwe, E.E., Jordan. J. Phys., 14 (2021) 345.

[29] Inyang, E.P., Obisung, E.O., William, E.S. and Okon, I.B., East Eur. J. Phys., 3 (2022) 114.

[30] William, E.S., Okon, I.B., Ekerenam, O.O., Akpan, I.O., Ita, B.I., Inyang, E.P., Etim, I.P. and Umoh, I.F., Intl. J. Quan. Chem., 122 (2022) e26925.

[31] William, E.S., Inyang, E.P., Ntibi, J.E., Obu, J.A. and Inyang, E.P., Jordan J. Phys., 15 (2022) 193.

[32] Inyang, E.P., William, E.S. and Obu, J.A., Rev. Mex. Fis., 67 (2) (2021) 193.

[33] Akpan, I.O., Inyang, E.P., Inyang, E.P. and William, E.S., Revista Mexicana de Física, 67 (3) (2020) 482.

[34] Inyang, E.P.,William, E.S., Obu, J.O., Ita, B.I., Inyang, E.P. and Akpan,1.O., Mol. Phys., 119 (2021) e1956615.

[35] Ibekwe, E.E., Okorie, U.S., Emah, J.B. Inyang, E.P. and Ekong, S.A., Eur. Phys. J. Plus, 87 (2021) 136.

[36] Inyang, E.P., Inyang, E.P., Akpan, I.O., Ntibi, J.E. and William, E.S., The Euro. J. Appl. Phys., 2 (2020) 26.

[37] Inyang, E.P., Iwuji, P.C., Ntibi, J.E., William, E.S. and Ibanga, E.A., East Eur. J. Phys., 1 (2022) 11.

[38] Omugbe, E., Osafile, O.E., Okon, I.B., Eyube, E.S., Inyang, E.P., Okorie, U.S., Jahanshir, A. and Onate, C.A., Eur. Phys. J. D., 76 (72) (2022) 11.

[39] Omuge, E., Osafile, O.E. and Onyeajh, M.C., Adv. High Ener. Phys., 10 (2020) 1143.

[40] William, E.S., Inyang, E.P. and Thompson, E.A., Rev. Mex. Fis., 66 (2020) 730.

[41] Edet, C.O., arXiv:2012.08644, (2020).

[42] Deta, U.A., Suparmi, A. and Cari, C., J. Phys. Conf. Ser., 539 (2014) 2018.

[43] Ikot, A.N., Ibanga, E.J., Awoga, O.A., Akpabio, L.E. and Antia, A.D., J. Mod. Phys., 3 (2011) 1855.

[44] Parmar, R.H., Few-Body Syst., 61 (2020) 39.

[45] Inyang, E.P., Inyang, E.P., William, E.S., Ibekwe, E.E. and Akpan, I.O., arXiv: 2012.10639, (2020).

[46] Inyang, E.P., Inyang, E.P., Ntibi, J.E., Ibekwe, E.E. and William, E.S., Ind. J. Phys., 95 (2021) 2733.

[47] Inyang, E.P., Inyang, E.P., Akpan, I.O., Ntibi, J.E. and William, E.S., Can. J. Phys., 99 (2021) 990.

[48] Abu-Shady, M., J. Egypt. Math. Soc., 23 (2016) 4.

[49] Barnett, R.M., Carone, C.D., Groom, D.E., Trippe, T.G. and Wohl, C.G., Phys. Rev. D, 92 (2012) 656.

[50] Tanabashi, M., Carone, C.D., Trippe, T.G. and Wohl, C.G., Phys. Rev. D, 98 (2018) 548.

[51] Nikiforov, A.F. and Uvarov, V.B., "Mat. Phys.", A. Jaffe (ed.), (Germany: Birkhauser Verlag Basel, 1988) 317.

Volume 15, Number 4, 2022. pp. 403-408

Jordan Journal of Physics

ARTICLE

Low-energy Gamma Unfolding Using NaI(Tl) Geant4 Detector Model and GRAVEL Code

S. Boukhalfa and **R. Khelifi**

LPTHIRM, Department of Physics, Faculty of Science, University of Blida 1 Soumaa Street, B.P. 270, Blida (09000), Algeria.

Doi: **https://doi.org/10.47011/15.4.9**

Received on: 16/02/2021; *Accepted on: 15/04/2021*

Abstract: In the field of gamma spectrometry with calibrated NaI(Tl) 3" × 3" γ-ray spectrometer, the correction of the photo-peak region of the original spectrum was discussed. In the present paper, GRAVEL algorithm based on Bayes theorem was used to test the unfolding process at low energetic interval, where Compton continium and background contributions are dominant. The simulated response matrix was constructed from mono-energetic γ-ray using validated Geant4 code. The calculated spectrum was compared with experimental ^{133}Ba gamma spectrum. The compared activities were found in good agreement in 4.10 % order.

Keywords: Spectrum unfolding, Gamma-ray spectra, Geant4 simulation, NaI(Tl) detector.
PACS: NaI(Tl): Sodium iodide (NaI) detector activated by thallium (Tl), Geant4: GEometry ANd Traking, FWHM: Full Width at Half Maximum.

1. Introduction

Up to now, the unfolding concept was successfully presented as a powerful method for spectral readability, especially for poor-resolution detectors, complex spectra and raw data. The unfolding process for neutron and gamma spectra was carried out by computer programs [1-7], where the instrument response function and pulse height distribution are needed. At this end, the instrument response function was constructed by numerical simulation using validated Geant4 code.

In this study, the interesting part is to check the validity test of unfolding GRAVEL code at the low-energetic range. Hence, the iterative GRAVEL validity was carried out for ^{133}Ba gamma-ray spectrum using an NaI(Tl) detector. The unfolded spectrum was compared with certified source activity to validate the followed approach and an acceptable increment of 4.10 % was found.

2. Materials And Methods

2.1 Running the GRAVEL Code

Let $Z(E)$ be the original spectrum emitted by a parallel γ calibration source located at X distance from the front surface of the detector, being the unknown and registered by an NaI(Tl) scintillation counter. $\Phi(E)$ is the experimentally observed spectra. $R(E, E_0)$ is the detector response function, recorded at energy E for emitting gamma ray at E_0.

The unfolding mathematical equation concerning $Z(E)$, $\Phi(E)$ and $R(E, E_0)$ is generally described as [4, 8-10]:

$$\phi(E) = \int_0^\infty Z(E) \times R(E, E_0) dE \qquad (1)$$

To solve this equation, the matrix detection system $R(E, E_0)$ and the measured pulse height

Corresponding Author: S. Boukhalfa **Email**: boukhalfasalma@gmail.com

spectrum $\Phi(E)$ can be expressed as in the following matrix equation [9]:

$$\phi(E) = Z(E) \times R(E, E_0) \quad (2)$$

For the unfolding process and inverting the instrument matrix $R^{-1}(E, E_0)$ in few channels by a successful way [11-12], a modified version of SAND-II method based on an iteration algorithm [6, 11] to a new method called GRAVEL [10] is used. The counts' vectors $\Phi(E)$, $Z(E)$ and the response matrix $R(E, E_0)$ can be rewritten in a matrix form as [7, 11]:

$$\phi(E) = \sum_l R_{kl} \times Z_l \quad (3)$$

The next gamma iteration record obtained after the unfolding process can be exploited discretely as [14-15]:

$$Z_i^{\alpha+1} = Z_i^{\alpha} \times \exp\left(\frac{\sum_k^n k \times A_{ik}^{\alpha} \times \ln\left(\frac{\phi_k}{R_k}\right)}{\sum_{k=1}^n k \times A_{ik}^{\alpha}} \right) \quad (4)$$

where $Z_i^{\alpha+1}$ is the new spectrum, Z_i^k is the γ emitted after α iteration, A_{ik}^{α} is the weighting factor [12] and R_k^{α} is the numeric pulse corresponding to γ convolution fluence [11-12].

The GRAVEL iteration algorithm stops running when the χ^2 is minimum [9]. It should be noted that the χ^2 value per degree of freedom n (Eq. 5) describes the goodness of the deconvolved spectrum. Also, it is used as a criterion for stopping the iteration procedure [9,11]:

$$\frac{\chi^2}{n} = \frac{1}{n} \sum_i \frac{\left(\sum_j R_{ij} Z_j - Z_i \right)^2}{\sigma_i^2} \quad (5)$$

From Eqs. (5) and (3):

$$\frac{\chi^2}{n} = \frac{1}{n} \sum_i \frac{\left(\phi_i - Z_i \right)^2}{\sigma_i^2} \quad (6)$$

Z_i and Φ_i are the unfolded spectrum and the measured spectrum, respectively, after i iterations. σ_i is the uncertainty of the measured spectrum.

As a consequence, if χ^2 per degree of freedom is almost 1, the iteration is convergent [11]. In this work, we have used 10000 iterations.

2.2 Detector Modelling

A cylindrical scintillation detector is coupled directly to a photomultiplier tube, hermetically sealed on the back of the crystal, housed by aluminium around it with a density of 2.7 g.cm^{-3} and surrounded by MgO powder. The MgO and NaI(Tl) crystal densities are 2.0 g.cm^{-3} and 3.667 g.cm^{-3}, respectively [13-14]. The SiO_2 back part was not considered during Geant4 (package 4-9.6.4 versions) simulation. In this study, the physics list used is G4EmStandardPhysics.

In Fig. 1, a screenshot of the NaI(Tl) 3"×3" detector model is shown.

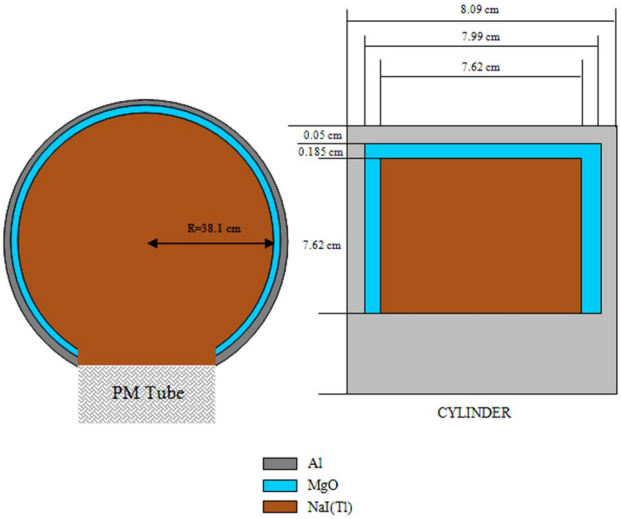

FIG. 1. Representation of the scintillator detector model.

The Gaussian energy broadening function was accounted for [15] by using three photopeaks of ^{137}Cs (661.6 keV) and ^{60}Co (1173.2 and 1332.5 keV) sources. Then, a non-linear fitting of the measured FWHM is used. In Eq. 7, the measured FWHM as an energy function can be expressed as:

$$FWHM = a + b\sqrt{E + cE^2} \quad (7)$$

where E is the incident particle energy, a, b and c are the energy broadening parameters determined by non-linear fitting (see Table 1).

TABLE 1. Adjusting FWHM parameters.

a (keV)	*b (keV^{-1})*	*c (keV^{-1})*
-88.7888	8.57634	0.000558254

The simulated geometry will be used to validate the Monte Carlo code by a punctual ^{137}Cs source fixed at 1 cm from the central axis of the detector. Experimentally, the acquisition time was kept as long as possible to get 1% statistical uncertainty.

During the Monte Carlo simulation, 10^6 events were generated.

2.3 NaI(Tl) Response Function

Due to the lack of mono-energetic sources, experimental measurements of the response function *R(E, E$_0$)* are not possible. As known, the spectral response function can be calculated using Monte Carlo methods [18-19]. In the case of a certified Bariym-133 source, gamma emission at 80.99 keV is chosen.

The simulated low-energetic boundary varied from 20 to 110 keV. The simulation series was carried out at an increment of 1 keV. The structure of each single response matrix for E$_0$ should be arranged in ascending order [11]. For good statistical results of each centroid peak, the history numbers were chosen by Geant4 code to achieve 1% uncertainly.

3. Results and Discussion

3.1 Validation of NaI(Tl) Detector Model

In Fig. 2, a 3D visualisation of the 3"×3" NaI(Tl) detector model considered in Geant4 simulation is presented. On the right side, we see the vertical section and on the left side, the NaI(Tl) detector structure is shown. In the same figure, the inner structure as crystal and the surrounding materials can be easily distinguished. Fig. 3 and Table 2 show a direct comparison between experimental and simulated pulse height distributions as the energy function of ^{137}Cs calibration source counted by the NaI(Tl) detector.

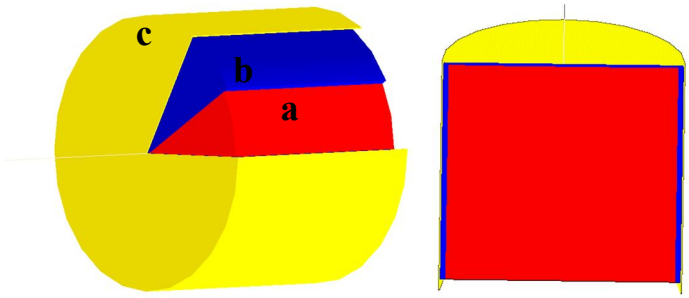

FIG. 2. Representation of scintillator detector model, (a): NaI(Tl) crystal, (b): MgO powder and (c): Aluminium cover.

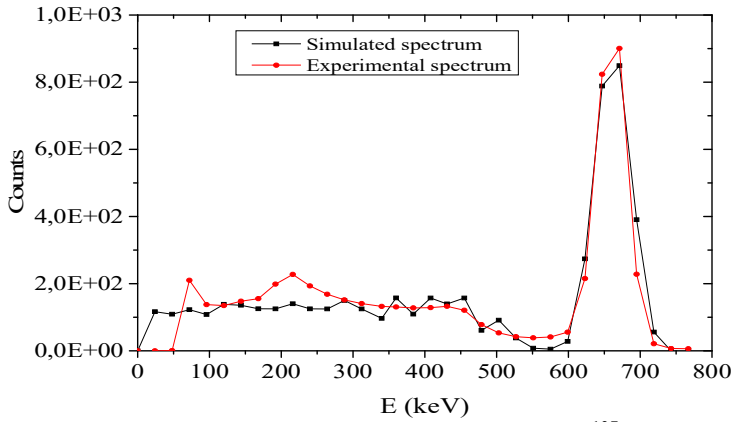

FIG. 3. Experimental and simulated pulse height distributions of ^{137}Cs punctual source.

TABLE 2. Measured and simulated data of ^{137}Cs source.

Energy (keV)	*Experimental*	*Geant4*
0	0	0
24	0	117
48	1	109
72	210	122
96	136	106
120	133	137
144	147	135
168	155	124
192	198	124
216	227	139
240	139	124
264	168	124
288	151	150
312	140	124
340	132	97
360	130	157
384	127	109
408	128	157
431	132	139
455	121	157
479	78	61
503	53	91
527	41	38
551	39	8
575	41	5
599	56	27
623	215	278
647	823	778
671	901	849
695	228	390
719	21	56
743	7	0
767	6	0

The obtained pulse height distribution was normalized by source activity [14]. The background radiation was subtracted from the original spectra and an acceptable accuracy between simulated and experimental data even in energy resolution at 661.6 keV is observed.

A similar test configuration using Monte Carlo codes was carried out with NaI(Tl) detector [14] and the same spectra form, approximately, was observed.

Below 300 keV, the Compton edges are lower than the measured spectrum, probably because of the scattered photons in the unclosed cylindrical shielding system around the detector [16], noting that the K-X-ray peaks of ^{137m}Ba source [17] are not considered in Geant4 simulation.

3.2 Unfolding Experimental Distribution by GRAVEL Algorithm

After background removal from ^{133}Ba experimental spectrum, $\Phi(E)$, GRAVEL iteration algorithm is used now for a few channel energies. The simulated response function $R(E, E_0)$ and pulse height vector $\Phi(E)$ are used. In Fig. 4, the unfolding spectrum (continuous line) shows a pulse height lower than in the measured spectra in the energy range 60 to 90 keV. It is due to the Compton and background removal. Consequently, the deconvolved area will be used to estimate the source activity. These results will be presented as histogram data. This type of figure is commonly used to represent similar results (e.g., Matzek (2002) and Cheminet (2003)).

Table 3 presents a comparison between the certified activity and the estimated activity.

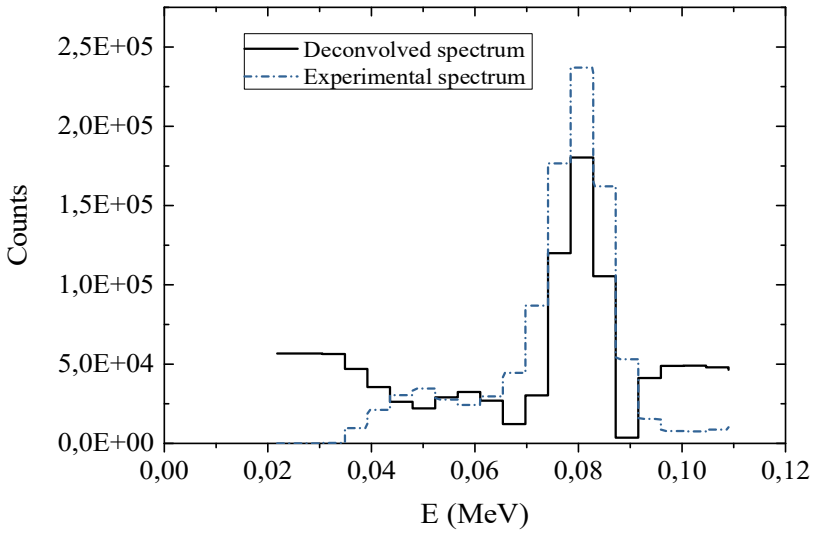

FIG. 4. Original spectrum (dashed line) and unfolded spectrum obtained by GRAVEL algorithm (continuous line) after 10000 iterations using ^{133}Ba at 81 keV energy.

TABLE 3. ^{133}Ba activity, (10^3 Bq).

Isotope	*Reference activity*	*GRAVEL*	*Relative error (%)*
^{133}Ba	29.2	28.0	4.10

4. Conclusion

In this work, the NaI(Tl) response function constructed by virtual mono-energetic photon sources using the validated Geant4 code is presented. The Geant4 simulation showed that the Gaussian energy broadening, experimentally measured, must be introduced during detector simulation.

The GRAVEL iterative method has been applied to experimental data in the 20-110 keV energy range.

The GRAVEL results are very encouraging and can be used with a high accuracy at low-energetic ranges. Besides, the unfolding spectra can be quickly analyzed because of Compton and background removal.

References

[1] Hartman, J. and Barzilov, A., Physics Procedia, 66 (2015) 410.

[2] Tripaty, S.P., Sunil, C., Nandy, N., Sarkar, P., Sharma, D. and Mukherjee, B., Nuclear Instruments and Methods in Physics Research-Section A, 583(2007) 421.

[3] Felter, T., "Development of a Neutron Unfolding Code", (2013) 1–9.

[4] Ewa, L. and Katarzyna, MM., Fusion Engineering and Design, 156 (2020) 111593.

[5] Shuhuan, L., Chen, D., Nannan, D., Jingye, A., Wenshou, Z. and Kai, W., Nuclear Science and Techniques, 18 (2007) 77.

[6] Rahman, M.S., Cho, G. and Kang, B.S., Radiation Protection and Dosimetry, 135 (2009) 203.

[7] De, S., Thomas, R.G., Rout, P.C., Suryanarayana, S.V., Nayak, B.K. and Saxena, A., Journal of Instrumentation, 13 (2018) 460.

[8] Tsoulfanidis, N., "Detection of Radiation Fields", Second Edn., (Taylor and Francis, University of Missouri-Rolla, 2005).

[9] Matzke, M., Instruments and Methods in Physics Research-Section A: Accelerators, Spectrometers, Detectors and Associatted Equipment, 476 (2002) 230.

[10] McElory, W.N., Berg, S., Crockett, T. and Hawkins, R.G., SAND II (Report AFWL-TR-67-41). US Weapons Laboratory, United States (1967).

[11] Matzke, M., The HEPROW Program System, (2003).

[12] Cheminet, A., Ph.D Thesis, University de Toulouse, (2013).

[13] Tekin, H.O., Science and Technolgy of Nuclear Installations, 2016 (2016) 7.

[14] Salgado, C.M., Brandão, L.E.B., Schirru, R., Pareira, C.M.N.A. and Conti, C.C., Progress in Nuclear Energy, 59 (2012) 19.

[15] Rahman, M.S. and Cho, G., Journal of Scientific Research, 2 (2010) 221.

[16] Berger, M.J. and Seltzer, S.M., Nuclear Instrumentation and Methods in Physics Research, 104 (1972) 317.

[17] Heath, R.L., "Scintillation Spectrometry: Gamma-ray Spectrum Catalogue", New Version, (1997).

[18] Kovaltchouk, V. and Machrafi, R., Annals of Nuclear Energy, 38 (2011) 788.

[19] Belgya, T. and Szentmiklósi, L., Nuclear Instrumentation and Methods in Physics Research-Section A, 991 (2021) 165018.

Volume 15, Number 4, 2022. pp. 409-416

Jordan Journal of Physics

ARTICLE

Variation of Secondary Gamma Radiation Flux during Closest Approach of Mars towards Earth, Mars at Opposition and Transit of Moon across Different Constellations and Planets in the Month of October, 2020 at Udaipur, India

Devendra Pareek and **Pallavi Sengar**

Department of Physics, Bhupal Nobles University, Udaipur (313001), Rajasthan, India.

Doi: **https://doi.org/10.47011/15.4.10**

Received on: 09/03/2021; *Accepted on: 30/03/2021*

Abstract: The experimental studies of closest approach of Mars towards Earth on October 6 & 7, 2020, Mars at opposition on October 13, 2020 and transit of Moon across different constellations and planets at Udaipur (27^0 43' 12.00" N, 75^0 28' 48.01" E), Rajasthan, India were conducted in the month of October, 2020 using a ground-based NaI (Tl) scintillation detector. For the closest approach of Mars, the data files were stored in computer for a half-hour duration from 20.30 IST to 1.00 IST on the dates of October 6 & 7, 2020, for Mars at opposition data files stored in computer for a half-hour duration from 18.00 IST to 20.00 IST on the date of October 13, 2020 and for Moon in the constellation experimental study the data files were stored in computer for a half-hour duration for the time 18.30 IST – 19.00 IST in the month of October, 2020 dated 19, 21, 22, 23, 25, 27, 28 and 29 at Udaipur (27^0 43' 12.00" N, 75^0 28' 48.01" E), Rajasthan, India, using a ground-based NaI (Tl) scintillation detector. For these experimental studies, the calibration of the scintillation detector was 2 keV per channel using a standard Cs^{137} source. Therefore, we detected the secondary radiation flux in the energy range from 2 keV to 2 MeV.

Analyzed data of closest approach of Mars revealed a significant enhancement of secondary gamma-radiation flux (SGR) of about 4.5% on closest approach of Mars towards Earth at time 00.00 IST -00.30 IST (October 7) in comparison to the time 20.30 IST -21.00 IST (October 6). We interpret that such enhancement of SGR flux is on the basis of closest approach of Mars towards Earth, reflection of solar radiation from Mars towards Earth and gravitational lensing effect produced by Mars. For Mars at opposition, the analyzed data revealed a significant enhancement of secondary gamma-radiation flux (SGR) of about 1.7% in between times 19.00 IST – 19.30 IST. We interpret such enhancement of SGR flux on the basis of Mars at opposition, combined gravitational pull due to planet Mars, planet Earth and the Sun and gravitational lensing by Mars and for transit of Moon, the analyzed data revealed a significant variation of secondary gamma radiation flux (SGR) in the month of October. We interpret such variation of SGR flux on the basis of transit of Moon across different constellations and planets in the month of October.

Keywords: Cosmic radiation, Reflection of solar radiation, Secondary gamma radiation, Closest approach of Mars, Mars at opposition, Combined gravitational pull and gravitational lensing effect by Mars, Transit of Moon across different constellations and planets.

Corresponding Author: Devendra Pareek **Email**: deven.pareek69@gmail.com

Introduction

Radiation coming towards the Earth from all directions is called cosmic radiation (CR) and such radiation has charged particles that travel at nearly the speed of light. Composition of CR is about 89% nuclei of protons, 10% nuclei of helium and 1% nuclei of other heavier elements (Lithium, Beryllium and Boron) [1, 2, 3]. Energy range of primary cosmic radiation is from 10^9 eV - 10^{20} eV or more [4]. In comparison, through interstellar abundance of elements and solar system with help of cosmic radiation, we can understand their origin and propagation process through interplanetary space and arrival on Earth. Simpson (1983) [5] pointed out chemical abundance of cosmic radiation in different energy ranges. He made a comparison between solar system abundances and estimated abundances for the local interstellar medium and observed that carbon, nitrogen, oxygen and iron groups are present both in the cosmic radiation and solar system abundances. In the atmosphere above 50 km from the surface of the Earth, the intensity of primary cosmic radiation flux is almost the same as in the interstellar space, but at about 20 km, secondary cosmic radiation produces a denser ionization. The number of particles reaching the Earth's surface is related to the energy of the primary cosmic radiation that struck the upper atmosphere. When high-energy primary cosmic radiation undergoes collisions with atoms of the upper atmosphere, it produces a cascade of lighter particles known as "secondary" particles and called secondary cosmic radiation [6]. In the atmosphere, there is a production of showers of secondary cosmic particles. These particles have X- rays, protons, alpha particles, pions, muons, electrons, neutrinos and neutrons. These particles increase rapidly as they move downward in the atmosphere and in each interaction, the particles loose energy [7, 8]. A small fraction of these particles usually comes down to the ground. In this way, secondary cosmic particles shower down through the atmosphere to the Earth's surface [9]. Such radiation has three components; an electromagnetic component, a hadronic component and a masonic component [10, 11, 12]. In the electromagnetic component, there is a presence of electrons and gamma particles. The hadronic component has low-energy protons and neutrons, while the masonic component has pions, muons, neutrinos and kaons. Therefore, penetrating cosmic radiation produces secondary shower [13]. Produced secondary cosmic radiation flux can be detected using an appropriate detector on the ground [14, 15].

It was observed that when the electromagnetic radiation passes near a massive object, then due to the gravitational field of the object, it bends. This phenomenon is called gravitational lensing. The object could be a galaxy, a star or a cluster of galaxies [16, 17, 18]. Gravitational lensing effect was proved by A. S. Eddington and collaborators in a famous experiment during a total solar eclipse in 1919.

Celestial Events and Variation of Radiation Flux

Secondary cosmic and solar radiation flux was observed by many scientist groups during normal days and on days of special celestial events, such as solar eclipse, lunar eclipse, appearance of comets in the sky, phases of the moon, closest approach of celestial objects, transit of celestial objects, … etc. with the help of an efficient counter system.

During solar eclipse, to observe the variation in secondary radiation flux, many experimental studies were conducted by scientist groups, such as Bhattacharya et al. [19], Kandemir, G. et al. [20], Nayak et al. [21], Bhaskar et al. [22] and Pareek et al. [23].

We conducted a solar eclipse study to understand the interaction of GCR and SR flux with gravitational fields (gravitational lensing) of the sun and well-established shadowing effect of the moon [23].

During lunar eclipse, to observe the variation in secondary radiation flux, many experimental studies were conducted by scientist groups, such as Pareek et al. [24], Raghav et al. [25] and J.N. Ananda Rao et al. [26].

Pareek et al. [24] did an experimental study to observe the variation of secondary cosmic and solar gamma radiation flux at some energy ranges. Such interesting finding can be explained on the basis of bending of primary cosmic radiation and solar radiation by combined gravitational lensing effect of Sun and Earth, backscattered secondary flux form the Moon, combined magnetic field of the Sun and the interplanetary magnetic field.

An experimental study of comets was conducted by Pareek et al. [27] using a

scintillation counter with lead shield in the energy range of 10 keV to 5 MeV. We observed an unusual variation of secondary cosmic radiation flux in the energy spectrum of specific energies of about1.127 MeV, 2.29 MeV and 3.66 MeV.

At the celestial event of transit of Venus on June 6, 2012 at Udaipur India, an experimental study was conducted by Pareek et al. [28]. After analyzing the collected data, it was observed that there was a 2 % decrement of secondary solar radiation gamma-ray flux.

A lunar phase ground-based experimental study was conducted by Pareek et al. using a scintillation counter in the month of September 2000 [29]. This experimental study provided information regarding the GCR, SR modulation at the time of new Moon, Full Moon and different phases of the Moon with different backgrounds of constellations in the sky. During the passes of Moon through the background of Capricornus constellation, an abrupt change in energy spectra was noticed on 9^{th} and 10^{th} September 2000 due to gravitational lensing effect.

With the fact that different celestial events happen in the sky, to study modulate terrestrial secondary flux of cosmic and solar radiation, we attempted to see the effect of closest approach of Mars, Mars at opposition and transit of Moon on secondary gamma-radiation flux on the surface of Earth.

The closest approach of Mars on October 7, 2020 was at the time 00.00 IST - 00.30 IST. The data was collected using a scintillation detector on the dates of 6 & 7 October from 20.30 IST to 1.00 IST.

The celestial event Mars at opposition occurred between times 19.00 IST-19.30 IST on October 13, 2020. During Mars at opposition, the planet Mars, Planet Earth and the Sun are in a straight line and the planet Mars was opposite to the Sun.

For transit of Moon study, the data files were stored in computer for a half-hour duration for the time 18.30 IST – 19.00 IST in the month of October, 2020 on dates 19, 21, 22, 23, 25, 27, 28 and 29.

Experimental Set-up and Observations

In these experimental studies, we used a scintillation detector (SD 152 F) of flat type (Fig. 1), Nucleonix made, to detect the secondary gamma-radiation flux. The radiation was allowed to enter in the NaI (Tl) crystal of size 2" x 2", optically coupled with a photo-multiplier tube. This integral line was connected to 1k multi-channel analyzer (MC 1000), Nucleonix made, with a USB interface built-in in a high-voltage shaping amplifier.

This scintillation counter system was kept open to collect the counts as a function of time on the roof of the Astronomy Laboratory of the Department of Physics, Bhupal Nobles University, Udaipur (Rajasthan), India. For closest approach of Mars, data was collected from 20.30 IST to 1.00 IST on the dates of 6 & 7 October 2020 and for Mars at opposition, the data files were stored in computer for a half-hour duration from 18.00 IST to 20.00 IST on the date of October 13, 2020. For transit of Moon study, the data files were stored in computer for a half-hour duration for the time 18.30 IST – 19.00 IST in the month of October, 2020 on dates of 19, 21, 22, 23, 25, 27, 28 and 29. For this experimental study, the detector is kept towards the Moon.

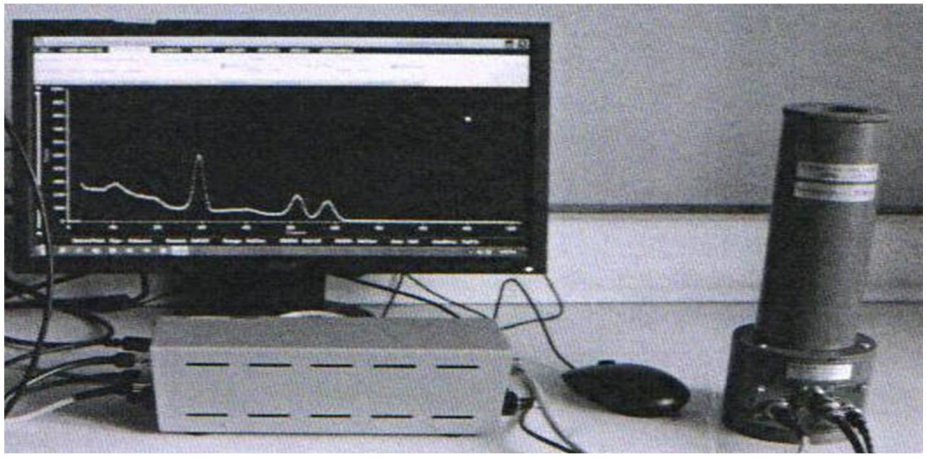

FIG. 1. Scintillation counter system.

Analysis and Results

As depicted in Table 1, the integrated counts of secondary gamma-radiation flux on the dates of 6 & 7 October 2020 from 20.30 IST to 1.00 IST for the experimental study closest approach of Mars towards Earth and using this Table 1, we plotted Fig. 2 between integrated counts and time of secondary gamma-radiation flux. For Mars at opposition, as given in Table 2, the integrated counts of secondary gamma-radiation flux on the date of 13th October 2020 from 18.00 IST to 20.00 IST are shown. Using this Table 2, we plotted Fig. 3 between integrated counts of secondary gamma-radiation flux and time.

TABLE 1. Closest approach of Mars.

Sr. No.	Time (IST)	Integrated Counts
1	20.30 – 21.00	317618
2	21.00 -21.30	320670
3	21.30 – 22.00	322044
4	22.00 – 22.30	327856
5	22.30 – 23.00	329391
6	23.00 – 23.30	329276
7	23.30 – 00.00	330220
8	00.00 -00.30	332178
9	00.30 – 1.00	329331

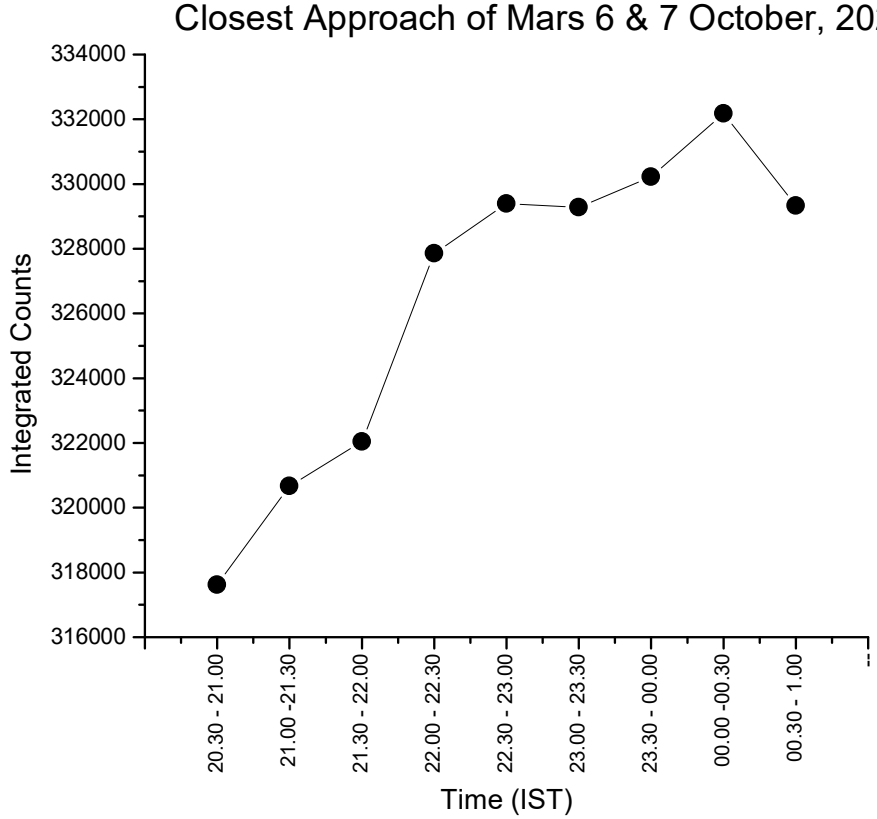

FIG. 2. Integrated counts of secondary gamma-radiation flux for closest approach of Mars on 6 & 7 October 2020.

Table 1 and Fig. 2 show that on the date of October 6, the integrated counts were 317618, 320670, 322044, 327856, 329391, 329276 and 330220 from time 20.30IST to 00.00 IST. On the date of October 7, the integrated counts were 332178 and 329331 from time 00.00 IST to 1.00 IST, respectively. On the date of October 6 at time 20.30 IST, the integrated counts were 317618, while at the closest approach of Mars towards Earth time (00.00 IST - 00.30 IST), the integrated counts were 332178. In comparison to closest approach of Mars towards Earth (00.00 IST -00.30 IST, on October 7) from the time 20.30 IST -21.00 IST (October 6) the increment in counts was 14500 i.e., 4.5 % enhancement of SGR flux counts. After closest approach of Mars time, the counts started to decrease from time 00.30 IST – 1.00 IST.

TABLE 2. Mars at opposition.

Sr. No.	Time (IST)	Integrated Counts
1	18.00 – 18.30	242481
2	18.30 – 19.00	242940
3	19.00 – 19.30	246732
4	19.30 – 20.00	246823

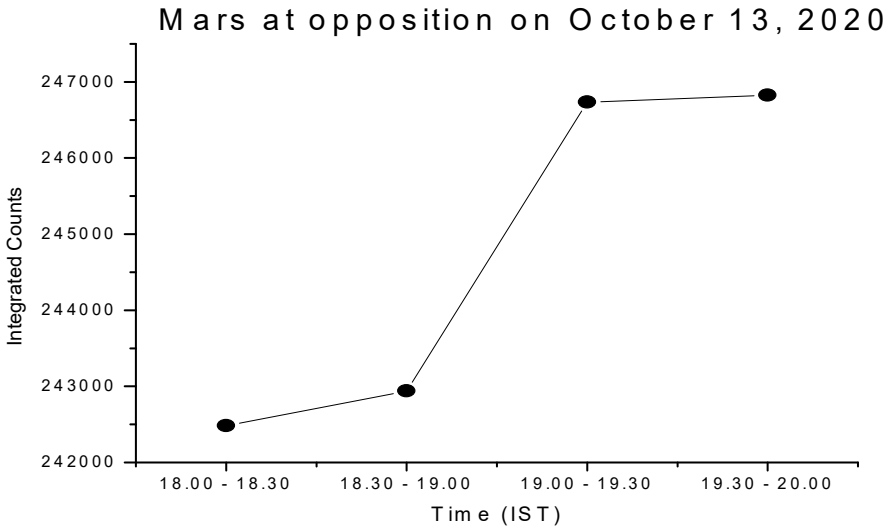

FIG. 3. Integrated counts of secondary gamma-radiation flux for Mars at opposition on 13 October 2020.

Table 2 and Fig. 3 show that on the date of October 13, the integrated counts were 242481, 242940, 246732 and 246823 from the time 18.00 IST to 20.00 IST. In comparison to time between 19.00 IST -19.30 IST, from the time 18.00 IST – 18.30 IST the increment in counts was 4251 i.e., 1.7 % enhancement of SGR flux and the SGR flux remains almost constant between the time 19.30 IST – 20.00 IST after Mars at opposition time.

For the experimental study transit of the Moon, as depicted in Table 3, the integrated counts of secondary gamma-radiation flux on the dates of 19, 21, 22, 23, 25, 27, 28 and 29 are shown. Using this Table 3, we plotted Fig. 4 between integrated counts of secondary gamma-radiation flux and dates.

TABLE 3. Transit of Moon.

Month of October, 2020 Time 18.30-19.00 (IST)		
Sr. No.	Date	Integrated Counts
1	19	255084
2	21	251022
3	22	259212
4	23	258957
5	25	240754
6	27	249136
7	28	248968
8	29	245372

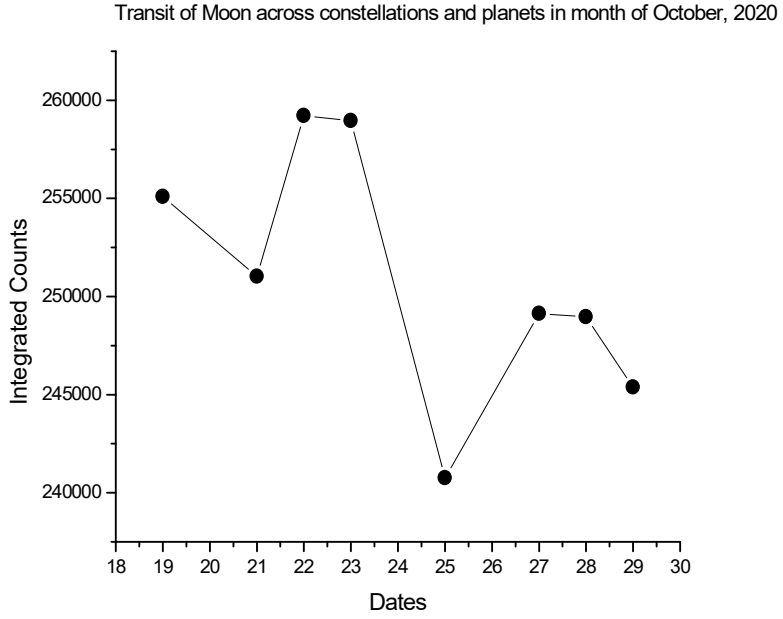

FIG. 4. Integrated counts of secondary gamma-radiation flux for transit of Moon across constellations and planets in October 2020.

Table 3 and Fig. 4 show that on the dates of 19, 21, 22, 23, 25, 27, 28 and 29 in the month October, the integrated counts were 255084, 251022, 259212, 258957, 240754, 249136, 248968 and 245372, respectively, in time 18.30 IST to 19.00 IST. On the date of 19 October, the Moon was close to the constellation Scorpius and then on the date of 21 October, it moved away from this constellation. On the date of 22, the Moon was in the constellation Sagittarius and close to planets Jupiter and Saturn. On the dates of 23 and 25, it moved away from the constellation and the planets. On the date of 27, the Moon was close to the constellation Aquarius and on onward dates 28 and 29, it moved away from this constellation.

Discussion

Closest Approach of Mars towards Earth

Table 1 and Fig. 2 clearly show that counts were increasing as the Mars approaches closer and closer towards the Earth. On the date of October 7, 2020 at time 00.00 IST – 00.30 IST, we observed the highest counts in comparison to other times of October 6 & 7, because at this time (00.00 IST – 00.30 IST), the planet Mars was closest to the Earth.

The probable reasons in this present study for the enhancement of SGR flux counts are as follows:

(1) On the dates of October 6 & 7, 2020 from time 20.30 IST to 00.00 IST -00.30 IST, Mars was regularly approaching closer and closer towards the Earth; therefore, the intensity of reflected solar radiation form the surface of Mars was increasing. Hence, the formation of secondary radiation flux became more and more in the atmosphere of the Earth.

(2) Due to closest approach of Mars, gravitational lensing effect becomes more significant. It was highest on the date (October 7, time 00.00IST to 00.30 IST) of closest approach of Mars towards the Earth. Therefore, more cosmic radiation came on the Earth atmosphere and the formation of secondary radiation became more.

Due to the above probable reasons given in points (1) and (2), we got 4.5% enhancement of secondary gamma-radiation flux counts on October 7, 2020.

This is a unique and new observation reported in the present study during the closest approach of Mars towards the Earth.

Mars at Opposition

Table 2 and Fig. 3 clearly show that counts during Mars at opposition time were 246732.

The probable reasons in this present study for the enhancement of SGR flux counts are as follows:

(1) On the date of October 13, 2020 between times 19.00 IST and 19.30 IST, the planet Mars, the planet Earth and the Sun are in a straight line and planet Mars is opposite to the Sun. Between these times, the combined gravitational pull due to all these celestial objects is significant and maximum. Therefore, more background radiation is pulled by this combined gravitational pull. Hence, the formation of secondary radiation flux became more in the atmosphere of the Earth.

(2) At time of Mars at opposition, the planet Mars produced a gravitational lensing effect. Therefore, more cosmic radiation was bent and came on the Earth atmosphere. So, the production of secondary radiation was more.

Due to the above probable reasons given in points (1) and (2), we got 1.7% enhancement of secondary gamma-radiation flux on October 13, 2020.

This is a unique and new observation reported in the present study during Mars at opposition.

Moon across Different Constellations and Planets

Table 3 and Fig. 4 clearly show the variation of counts during Moon across different constellations and planets.

The probable reasons in this present study are as follows:

1. On the date of 19 October, the Moon was close to the Scorpius constellation and on 21 October, the Moon was shifted away from this constellation and so, there was a decrease in counts from 255084 to 251022; i.e., the decrement in counts was 4062. This clearly represents the gravitational lensing effect on the background cosmic radiation due to constellation Scorpius and the radiation from this constellation.

2. On the date of 22 October, the Moon was in the constellation Sagittarius and close to the planets Jupiter and Saturn. Therefore, we observed the highest counts of 259212 in this observation. This is due to radiation coming from the constellation, gravitational lensing effect by the constellation on background radiation, combined gravitational lensing effect on background radiation due to planets and reflected solar radiation from planets. Therefore, more radiation was bent along with reflected solar radiation, which may produce more showers of secondary gamma-radiation particles in the atmosphere of the Earth.
3. On 27 October, again there was an increase in the integrated counts by 8382 in comparison to the date of 25. On this date, the Moon was close to constellation Aquarius. Therefore, due to gravitational lensing and radiation from the constellation, there was an increase in the counts of secondary gamma-radiation flux.

Therefore, whenever the Moon passes from a constellation, then due to gravitational lensing and radiation from the constellation, more cosmic radiation is bent. This bent radiation impinges deep inside the atmosphere of the Earth, which produces more secondary gamma-radiation particles that give such variation in the month October.

Also, when the Moon comes close towards planets, then there was an increment in the counts due to more formation of secondary radiation from reflected solar radiation and gravitational lensing effect due to planets on background radiation.

Due to the above probable reasons given in points (1), (2) and (3), we can understand the variation of secondary flux during transit of the Moon across different constellations and planets.

This is a unique and new observation reported during transit of the Moon across different constellations and planets.

Conclusions

(A) On October 7, 2020, the planet Mars was closest towards the Earth, so we observed an enhancement of secondary gamma-radiation flux of about 4.5 % on the surface of the Earth.

(B) On October 13, 2020 between times 19.00 IST – 19.30 IST during Mars at opposition, we observed an enhancement of secondary gamma-radiation flux of about 1.7% on the surface of the Earth.

(C) Experimental study transit of Moon gave information about variation of secondary gamma-radiation flux on the surface of the Earth due to transit of the Moon across different constellations and planets.

Acknowledgment

The authors are thankful to Himanshu Singh Chouhan who was involved in these experimental studies.

References

[1] Longair, M.S., “High-energy Astrophysics" 1st and 2nd Eds., (Pub. Cambridge University press, 1992).

[2] Chaisson, E. and Mcmillan, S., “Astronomy Today”, 3rd Ed., (Prentice Hall, 1999).

[3] Mewaldt, R.A., “Cosmic Rays”, (California Institute of Technology, 2010).

[4] Kudela, K., Actaphysicas Lovaca, 59 (2009) 537.

[5] Simpson, J., Annual Reviews of Nuclear and Particle Science, 33 (1983) 323.

[6] Anderson, C.D. and Neddermeyer, S.H., Physical Review, 50 (1936) 263.

[7] Bhabha, H.J., Proc. Roy. Soc. A, 166 (1938) 501.

[8] Bhabha, H.J., Nature, 141 (1938) 117.

[9] Allkofer, O.C. and Grieder, P.K.F., “Cosmic Rays on Earth”, (1984).

[10] Heitler, W.H., Proceedings of the Royal Society A, 161 (1937) 261.

[11] Nordheim, L.W., Physical Review, 51 (1937) 1110.

[12] Pfotzer, G., Z. Phys., 102 (1936) 23.

[13] Heitler, W., Royal Society, 166 (927) (1938) 529.

[14] Kodama, M., Journal of Physical Society of Japan, 52 (1983) 1503.

[15] Chilingarian, A., Daryan, A., Arakelyan, K., Hovhannisyan, A., Mailyan, B., Melkumyan, L., Hovsepyan, G., Chilingaryan, S., Reymers, A. and Vanyan, L., Physical Review D, 82 (4) (2010) 043009.

[16] Walsh, D., Carswell, R.F. and Weymann, R.J., Nature, 279 (5712) (1979) 381.

[17] Mellier, Y., Ann. Rev. Astron. Astrophys., 37 (1999) 127.

[18] Narayan, R. and Bartelmann, M., "Lectures on gravitational lensing", (1996).

[19] Bhattacharyya, A., Biswas, S., Chatterjee, B.K., Das, M., Das, P.K., Das, T.K., De, T.K., Engineer, M.H., Mukherjee, R.N., Raha, S., Roy, S.C., Saha, S.K., Sen, A.K., Sinha, B. and Syam, D., Astrophysics and Space Science, 250 (1997) 313.

[20] Kandemir, G. et al., ASP Conference Series: The Last Total Solar Eclipse of the Millennium in Turkey, 205 (2000) 202.

[21] Nayak, P.K. et al., Astroparticle Physics, 32 (2010) 286.

[22] Bhaskara, A., Purohit, A., Hemalatha, M., Pai, C., Raghav, A., Gurada, C., Radha, S., Yadav, V., Desai, V., Chitnis, A., Sarpotdar, P. and Patankar, A., Astroparticle Physics, 35 (5) (2011) 223.

[23] Pareek, D., Jaaffrey, S.N.A., Talesra, K.P., Yadav, R. and Ameta, S., Research Journal of Physical Sciences, 1 (5) (2013) 22.

[24] Pareek, D. and Jaaffrey, S.N.A., Research Journal of Physical Sciences, 1 (4) (2013) 22.

[25] Raghav, A., Bhaskar, A., Yadav, V., Kumar, N., Pai, B.C., Koli, A., Navale, N., Pal Singh, G., Dubey, N., Pawar, S., Parab, P., Narvankar, G., Rawoot, V., Rawat, V., Borse, S., Garad, N., Rozario, C., Kaushal, N., Tiwari, S.K. and Press, M.R., Journal of Geophysical Research: Space Physics, 118 (10) (2011) 6426.

[26] Ananda, R.J.N., Physics Letters A, 25 (2) (1967) 74.

[27] Pareek, D. and Jaaffrey, S.N.A., International Journal of Scientific Research, Ahmedabad, 3 (4) (2014) 411.

[28] Pareek, D., Jaaffrey, S.N.A., Daspattnayak, H.T. and Shrimali, M., Global Journal for Research Analysis, Ahmedabad, 6 (5) (2017) 500.

[29] Pareek, D. and Jaaffrey, S.N.A., International Journal of Scientific Research, Ahmedabad, 3 (5) (2014) 6.

Volume 15, Number 4, 2022. pp. 417-427

Jordan Journal of Physics

ARTICLE

Development of a Radiometer for Ground-based Ultra Violet (UV)/ Cosmic Particle Characterization

Lanre O. Daniyan[a], **Matthew O. Afolabi**[a], **Ilesanmi A. Daniyan**[b] and **Felix Ale**[c]

[a] *Department of Physics and Electronics, Adekunle Ajasin University, Akungba Akoko, Ondo State, Nigeria.*

[b] *Department of Industrial Engineering, Tshwane University of Technology, Pretoria 0001, South Africa.*

[c] *National Space Research and Development Agency (NASRDA), Abuja, Nigeria.*

Doi: **https://doi.org/10.47011/15.4.11**

Received on: 04/05/2021; *Accepted on: 22/08/2021*

Abstract: The need for high-precision radiometers for the measurement of solar ultraviolet (UV) radiation triggered this research interest. This is due to the quest for the determination of the trends of terrestrial UV trends associated with the depletion of the ozone layer. This work features the development of a radiometer for the characterization of UV and ionizing radiations from the sun reaching the earth surface at a specific location. The radiations were quantified with the aid of a UV radiation sensor, Geiger tubes, a microcontroller and associated devices. Time series and location coordinates were stamped on the data records with the aid of NEO6M Global Positioning System (GPS) modules. The ionizing radiations were characterized in counts per minute (cpm), while the UV index indications were realized from the voltage output (mV) of the UV sensor using a model based on the UV index chart. The results obtained indicate that the UV index ranges from a minimum value of 0 to a maximum value of 3, while the radiation count ranges from a minimum value of 0 to a maximum value of 48 cpm for 3 days. Hence, the status of the ozone layer can be ascertained from a review of a much longer period of data gathering.

Keywords: CPM, CSV, FFF, Geiger, GPS, Ionizing, UV.

1. Introduction

The increasing trends of human activities have led to the production of gases, such as chlorofluorocarbons CFCs (CFCs) which are destructive to the ozone layer. The ozone layer in the stratosphere absorbs most of the UV radiation emitted from the sun [1]. Hence, the ozone protects the earth's surface from the intense UV radiation from the sun, which is harmful to humans and the environment. However, the generation of gases, which depletes the ozone layer, upsets the natural balance of ozone, thus resulting in a decline in the ozone levels in the stratosphere. These reduced ozone levels have increased the amount of harmful ultraviolet radiation reaching the earth's surface [1]. Since the sun is the major propelling force of the terrestrial atmospheric processes, the variations in the atmospheric processes can be traced to the variations which arise as a result of solar radiation and its modulation by the earth's orbital motion [2-3]. Some of these variations are caused by the cosmic rays, which stem from the galactic and solar sources. The constituents of cosmic rays include high-speed neutrons, electrons and atomic nuclei. Cosmic-ray particles are mostly

Corresponding Author: Lanre O. Daniyan **Email**: danomartins@hotmail.com

comprised of fully ionized elements, such as hydrogen (87-90%) and some helium (9-12%) with small amounts of electrons (1%) [4-5]. Cosmic-ray energy level ranges between 300 MeV and 10 GeV [4]. The primary cause of modulation of cosmic rays has been traced to the variation in the magnitude of the solar wind. Hence, the variations in the UV radiation call for the need for high-precision radiometers for the measurement of solar ultraviolet (UV) radiation in order to determine the terrestrial UV trends associated with the depletion of the ozone layer. The isotopic composition of the cosmic rays provides important information about the source, acceleration and transport phenomenon of cosmic rays in the galaxy.

The knowledge of the elemental composition of cosmic rays will assist in the determination of the chemical fractionation in the source region. This will also provide information about the nature of the source region as well as the propagation of cosmic rays in the interstellar space [5]. The identification of the cosmic-ray isotopes will further enhance the understanding of the nature of the source region as well as the timescales of the injection and initial acceleration. Measurements at high energies will indicate the sources of the particles. At the highest energies, the presence of cosmic rays may indicate the approximate direction of the most powerful source [5]. Cosmic rays and energetically charged particles in space influence some occurrences in the solar atmosphere, heliosphere and geosphere. The characterization of the particles is necessary in order to understand the changes in the physical state of the magnetosphere, study the effects of space radiations on humans and the environment and understand the electromagnetic propagation in the environment [6-8].

At the core of the sun, energy is generated *via* thermonuclear reactions, creating extreme temperatures deep within the sun's core [3]. This results in a continuous emission of solar particles, ionizing radiations, Corona mass ejections, solar winds, solar flares, plasmas and other high-energy cosmic particles spanning the full electromagnetic spectrum that travel through the heliosphere. Some of these particles are absorbed, re-emitted at lower energies or intercepted within the interplanetary space.

The stratospheric ozone blocks some of these dangerous particles from reaching the earth's surface in quantities considered very dangerous to life on earth [9]. Thus, the dynamic nature of the ozone layer underscores the need to constantly monitor the quantity of radiations reaching the earth surface. Furthermore, the issue of climate change with increasing global warming has been traced to the net imbalance in the energy radiation of the earth [10]. In addition, a striking increase in the cases of skin cancers has been detected in fairly skinned populations worldwide since the early 1970s and the rising cases have been heavily linked to sun exposure and its ultraviolet (UV) component [10]. Other exposure risks include acute and chronic skin disorder such as sunburn, tanning, eye disorder, such as cataracts and photokeratitis as well as immune system disorders … etc.

Small quantities of UV radiation are needed for the production of vitamin D, which is beneficial to the human health. It is also needed in small amounts in the treatment of some disorders and diseases, such as rickets, psoriasis and eczema under proper medical supervision. However, there are some major health risks associated with the prolonged exposure to UV. Continuous exposure to UV in the long term could also induce degenerative changes in cells, fibrous tissue and blood vessels, which could lead to premature skin ageing. UV radiation can also cause inflammatory reactions of the eye, such as photokeratitis [10-11]. The aim of this study is to develop a radiometer for ground-based UV / cosmic particle characterization by integrating a UV sensor, a Geiger counter, a Global Positioning System (GPS) module and a Secure Digital (SD) memory card to a central microcontroller. The development of a high-precision ground-based radiometer will provide the relevant information about the trends of the UV levels over a period. The information about the UV levels acquired by the radiometer can also be employed for the evaluation of radiative transfer models.

The succeeding sections present a literature review in order to explore the research gaps, the materials and methods employed in this study as well as the results obtained, the conclusions and directions for future study.

2. Literature Review

Many works have been reported in an effort to estimate the magnitude of cosmic ray and characterize its particles. For instance, Simonsen

et al. [12] developed a ground-based Galactic Cosmic Ray (GCR) simulator aimed at generating a spectrum of ion beams that approximates both the primary and secondary GCR fields experienced at human organ locations in order to mitigate the health risks due to exposure to cosmic rays. Slaba *et al.* [13] developed a preliminary beam-selection strategy for accelerator-based GCR simulation. Utomo [4] found a strong - but inverse - correlation relationship between the solar activity and cosmic rays as well as a strong and positive correlation between the solar activity and solar constant. As reported by Utomo [4], an increase in the magnitude of cosmic rays produces a decline in the solar constant. When cosmic-ray particles with high energy (10 GeV) enter the earth's atmosphere at a speed near to $3 \times 10^8\ m/s$, there is a possibility of collision with the atmospheric molecules. The collision may cause the composition of the molecules in the atmosphere to break, thereby forming secondary ions which act as condensation nuclei. Hence, this phenomenon can bring about an increase in the rate of cloud formation with subsequent reduction in the intensity of solar radiation that reaches the earth's surface. Marinan *et al.* [14] assessed a radiometer calibration with GPS radio occultation for the MiRaTA CubeSat mission. An initial estimation of the retrieved temperature precision indicated that the developed system should meet the requirements for the Global Positioning System Radio Occultation (GPSRO) temperature precision based on the thermal noise contribution of error. Mendonça *et al.* [15] analyzed the atmospheric effects of cosmic rays and the underlying relationships to cut-off rigidity and zenith angle. The analysis was carried out using Global Muon Detector Network, which consists of four multidirectional muon detectors placed at different locations, between 2007 and 2016. The results obtained indicated that the main atmospheric effects are related to pressure and temperature changes. Part *et al.* [16] developed a UV index sensor - based device with the EUVB ratio of natural light. The developed device demonstrated the capacity to acquire UV-related information, such as UVI and EUVB, which are critical to the prevention of potential damage due to exposure to UV radiation.

In this work, a UV/ cosmic particle meter was developed to characterize in real time UV and cosmic ionizing radiations reaching the earth's surface at a specific location. Alongside the times of events and the specific location coordinates, the quantities of these radiations were logged in an SD card. There is a dearth of information relating to the development of a UV/ Cosmic particle meter, which has the capacity to characterize in real time UV and cosmic ionizing radiations reaching the earth's surface at a specific location alongside the times of events and the specific location coordinates. The concept of additive manufacturing was explored in the development of the casing, which makes its process of development time- and cost-effective and easy for rapid prototyping. The development and use of the UV/ cosmic particle meter will definitely provide insight into the state, permeability and dynamics of the ozone layer. It will also strengthen sun-protection programmes and increase the awareness of the health hazards of UV radiation. This will assist people to change their lifestyle and habits in order to reduce the chances of the health risk associated with undue exposure to UV. Following a reliable means of UV measurement, effective sensitization programs can be developed in order to enhance the public health and the general approach to sun protection.

3. Materials and Methods

The developed radiometer employs the principles of spectroadiometric measurement for the characterization of the UV and ionizing radiations from the sun reaching the earth surface at a specific location. The choice of the spectroadiometric measurement stems from the problem to be addressed; ground-based Ultra Violet (UV)/ cosmic particle characterization. The ground-based measurement developed in this study is essential for proper understanding of the factors which affect the transmission of UV radiation *via* the atmosphere. It is also necessary for the evaluation of the effects of UV radiation on both the earth's ecosystems and human health [1]. The developed ground-based radiometer which employs the principles of spectroadiometric measurement is useful for detecting the UV trends and is also capable of data acquisition for the development and evaluation of radiative transfer models.

Comparing the spectral and broadband measurements, spectral measurement employed in this study boasts the effective computation of biological impacts of UV radiation for any action

spectrum and of the acquisition the information on the atmospheric composition given by the fine structure of the spectrum. It is also flexible in application and eliminates spectral mismatch. However, it requires the expertise of the operator in order for effective calibration and measurement before reliable results can be obtained. On the other hand, the broadband measurement is limited only to one action spectrum, being designed to strictly follow and rely on theoretical correction factors to compensate for the spectral difference between the meter response and the desired action spectrum in order to obtain the estimates for various effects following different action spectra. However, the merits of the broadband measurement include simplicity of operation and cost effectiveness.

The materials employed for the development of the radiometer are presented in Table 1.

TABLE 1. Materials employed for the development of the radiometer.

S/N.	Material	Quantity
1.	UV sensor (ML8511)	1
2.	SD card	1
3.	Geiger counter (D-v1.1(CAJOE) with tube series J3058 2020I)	1
4.	Microcontroller (Atmel ATMega328P)	1
5.	GPS module	1
6.	Step up (LM6009)	1
7.	Li-ion 18650 batteries	4
8.	Polyethylene Terephthalate Glycol (PETG) filament for casing (building volume: 200x200x180 mm)	½ roll

3.1 System Architecture

The system architecture of the developed UV/ cosmic particle meter for the characterization of the cosmic ionizing radiation is presented in Fig. 1. The UV sensor detects the UV radiation variabilities and sends corresponding signals to the microcontroller for processing. The Geiger tube detects ionizing radiations from the sun and sends the corresponding pulse counts to the microcontroller, which in turn counts the frequencies in number of occurrences per minute (cpm). Subsequently, the UV index is computed from the UV voltage levels by the microcontroller through a pre-programmed UV index chart. The date, as well as the time series are extracted from the GPS NMEA sentences and logged with the UV and Geiger data onto the SD card in CSV format.

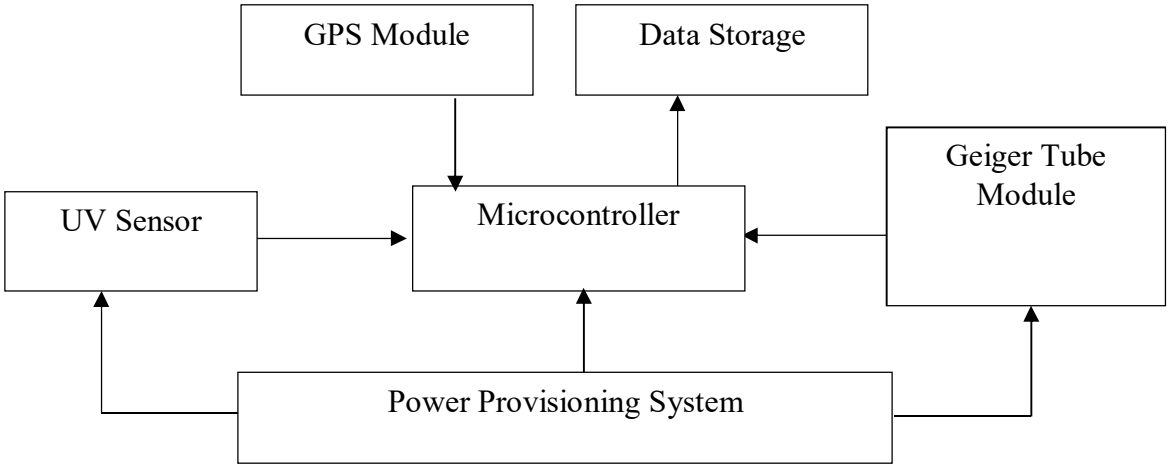

FIG. 1. Architecture of the UV/ cosmic particle meter.

3.2 Proteus Model

Fig. 2 presents the Proteus model of the system circuitry, which depicts the connection of the Geiger counter, GPS, memory and UV sensors to the central microcontroller.

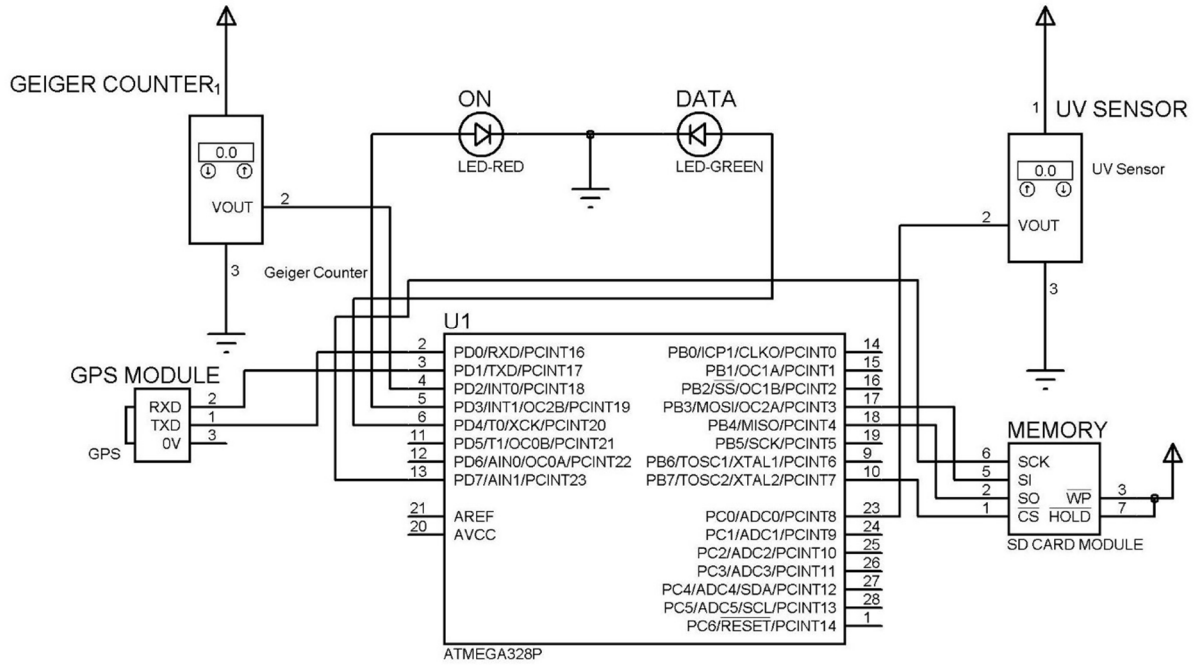

FIG. 2. Proteus model of the system circuitry.

3.3 Material Consideration

For the implementation of this design, the following materials were considered.

1. A UV sensor ML8511 was used. This sensor outputs analog voltage that is linearly related to the measured UV intensity (mW/cm^2) in the range of 200 – 375 nm wavelength. This module with an input voltage range of 3.3 – 5 V has an output voltage range of 0 – 1 V. The ML8511 is equipped with an amplifier, which converts photocurrent into voltage depending on UV intensity[17]. Its normal environmental working temperature range is -20 to 85^{o}C.
2. A Geiger radiation counter D-v1.1(CAJOE) with the tube series J3058 2020I was employed for picking the doses of ionizing radiation. A Geiger counter is a device used for detecting and measuring ionizing radiation. The tube is filled with an inert gas that becomes conductive when it is impacted by a high – energy particle [18]. The tube with a diameter of 10 mm and a length of 90 mm has a starting voltage of about 350 V, an operational voltage of about 380 V and an extreme voltage of about 550 V. It is very suitable for environments with temperatures of about -40 - 55^{o}C. The tube has a chamber containing two electrodes and a potential difference of several hundred volts and is also filled with inert gas at low pressure. A charged particle passing through the gas causes excited and ionized molecules along its path [19]. With the high voltage and consequently the strong electric field, there is a resultant conduction in the tube.
3. LM6009 boost converter steps up the voltage from about 3.7 V provided by an array of Li-ion to a regulated 5 V needed to operate the system. This converter has an input range of 3–32 V, an output range of 5–35 V and a maximum output current of 4 A [20].
4. An Atmel ATMega328P microcontroller was programmed to count the pulse input from the Geiger counter module and receive input from the UV sensor and the time-location strings from the NEO6M GPS module. ATMega 328P is an 8 – bit AVR microcontroller with 32Kbytes in-system programmable flash [21].
5. Other materials include Li-ion 18650 batteries and an SD card module for data storage.

The ATmega 328p microcontroller was employed as the central controller. This microcontroller was installed on a circuit board developed using a vero board. The microcontroller is comprised of 14 digital pins and 6 programmable analog inputs. The outputs of the UV sensor are fed into the microcontroller alongside the time-location strings from the GPS. The microcontroller is programmed to

count the pulse input from the Geiger counter module.

3.4 Casing Fabrication

The casing was modelled using Rhinoceros, a Computer-aided Design (CAD) environment for 3D modeling. The 3D model was subsequently sliced using CURA slicer with a 0.1-mm layer height configuration. The resultant G-code was fed into Whanhao duplicator i3 plus, for fused filament fabrication *via* the process of additive manufacturing. Whanhao duplicator i3 plus is a single-extruder system with a building volume capacity of 200x200x180 mm [22]. Fig. 3 presents the block diagram for the additive manufacturing process. The additive manufacturing (AM) is an emerging digital technology capable of producing component parts directly from a digital model [23-24]. The 3D model was implemented using sky blue and white PETG filament *via* additive manufacturing to realize the casing.

The model shown in Fig. 4 was implemented using the additive manufacturing technique. The final product is shown in Fig. 4.

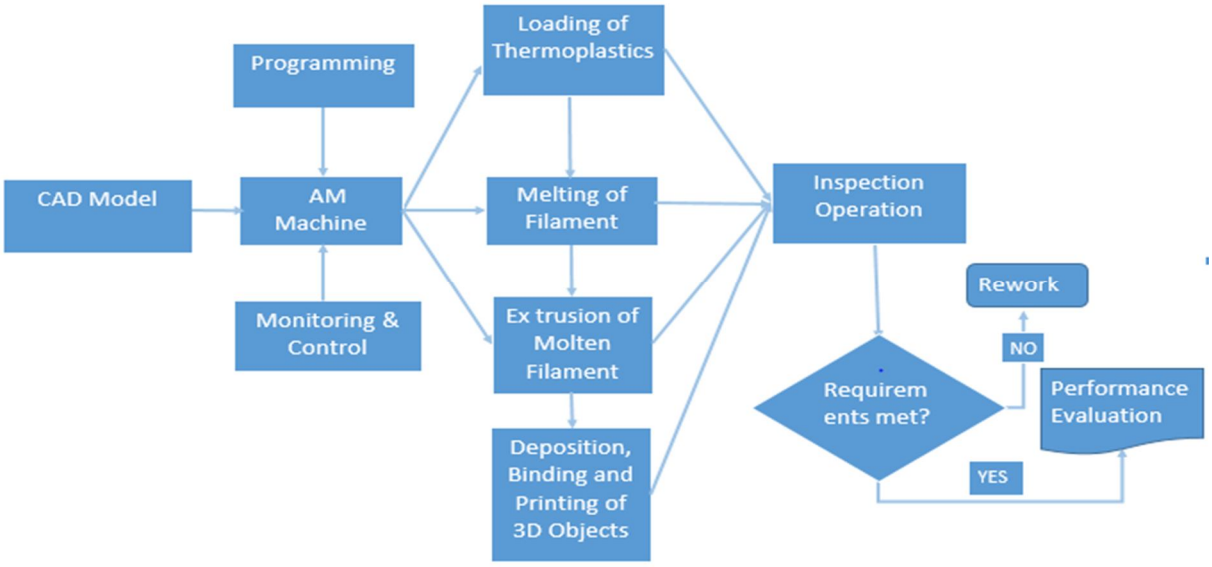

FIG. 3. Block diagram for the additive manufacturing process [25].

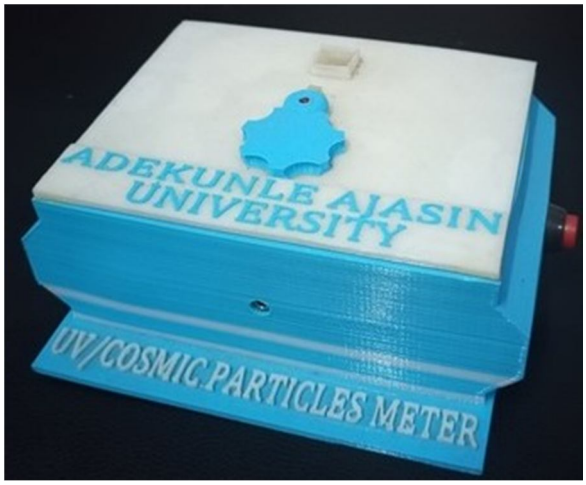

FIG. 4. The UV/ cosmic particle meter.

3.5 Performance Evaluation of the Radiometer

The radiometer characterizes UV and ionizing radiation from the sun reaching the earth surface at a specific location. The intensity of these cosmic radiations depends on the time of the year, the geographical location and the dynamics of the ozone layer the state of which determines its permeability to radiations. These radiations were quantified with the aid of a UV radiation sensor, Geiger tubes, a Microcontroller and associated devices. Data is stored in an SD card in Comma Separated Version (CSV) format

for future processing. Time-series and location coordinates were stamped on the data records with the aid of NEO6M GPS modules. The ionizing radiations were characterized in counts per minute (cpm), while the UV index indications were realized from the voltage output (mV) of the UV sensor using a model based on the UV index chart. The characterization of UV and ionizing radiations were carried out at a specific location between 10 am and 2 pm and at an update cycle of five minutes for a test period of three days. The geographical features of the location are as follows: latitude: 6.84, longitude: 7.35, altitude: 432 m, as indicated by the GPS subsystem.

Eq. (1) expresses the global solar UV index (CIE: ISO 17166:1999/CIE S 007/E-1998) which measures the UV radiation.

$$I_{UV} = k_{er}.\int_{250\,nm}^{400\,nm} E_{\lambda}.S_{er}(\lambda)d\lambda \quad (1)$$

where E_{λ} is the solar spectral irradiance $(W/(m^2.nm^1)$, (λ) is the wavelength and $d\lambda$ is the wavelength interval. S_{er} is the erythema reference action spectrum and k_{er} is a constant equal to 40 m^2/W.

The mean rate of change of momentum of an individual particle, as given by the adiabatic deceleration rate, is expressed by Eq. (2) [26]:

$$\dot{P}_{ad} = \frac{-p^i}{3}\frac{\partial}{\partial r}.V \quad (2)$$

where p^i is the particle momentum (kg m/s) and V is the solar-wind velocity (m/s) at a position r.

Eq. (3) expresses the mean rate of change of momentum of the cosmic-ray particles having momentum p^i specified relative to the wind frame at position r [26].

$$(\dot{p^i})^* = \frac{-P^i}{3}\frac{\partial}{\partial r}.V \quad (3)$$

Considering the particle streaming and energy changes, the continuity equation for the cosmic rays which propagate in the interplanetary region is expressed by Eq. (4).

$$\frac{\partial(U_p)^*}{\partial t} + \frac{\partial}{\partial r}.(S_P)^* + \frac{\partial}{\partial p^i}\left((\dot{p}^i)^*(U_p)^*\right) = 0 \quad (4)$$

where r is the position, p^i is the particle momentum (kg m/s), $(U_p)^*$ is the differential number density and $(S_P)^*$ is the differential current density.

Eq. (5) expresses the time rate of change of momentum of the particles in the fixed frame [5].

$$\dot{p} = \frac{p}{3U_p}V.\frac{\partial U_p}{\partial r}. \quad (5)$$

For spectroradiometric measurement, Eq. (6) holds [1]:

$$S(A,\Delta\lambda,\lambda_o) = \int_{\Delta\lambda}^{\infty}\int_{A}^{\infty} E_{\lambda}(x,y,\lambda)R_{\Phi}(\lambda_o,\lambda)dAd\lambda \quad (6)$$

where E_{λ} is the spectral irradiance (w/m^3) measured at points $x\ and\ y$ and at a wavelength λ (nm). R_{Φ} is the flux responsivity of the spectroradiometer (V/W), $\Delta\lambda$ is the bandwidth of the spectroradiometer (bps) and A is the area of the receiving aperture (mm^2).

For a homogeneous field, Equation 6 reduces to Eq. (7) [1].

$$S(\lambda_o) = A\int_{\Delta\lambda}^{\infty} E_{\lambda}\,(\lambda)R_{\Phi}(\lambda_o,\lambda)d\lambda\,. \quad (7)$$

The bandwidth of the measurement instrument is determined using Eq. (8) [1].

$$\Delta\lambda = \frac{\int_{\Delta\lambda}^{\infty} R_{\Phi}(\lambda_o,\lambda)d\lambda}{R_{\Phi}(\lambda_o,\lambda)}. \quad (8)$$

The radiometer uses a Geiger tube J305 202I which is largely used for the detection of beta and gamma radiations. The Geiger tube contains a low-pressure inert gas, usually helium, neon or argon, thus making the Geiger tube non-conductive under normal conditions. Whenever the tube receives cosmic-ionizing radiation reaching the earth's surface, the gas is ionized; electrons are stripped off the inert gas molecules, thus making the inert gas conducting across the electrodes which have a potential difference of about 500 Volts across the terminals. When the gas molecules are ionized, positively charged ions and electrons are created. A strong electric field is created by the tube's electrodes, accelerating the ions towards the cathode and the electrons towards the anode. The ion pairs gain sufficient energy to ionize further gas molecules through collisions on their way, thereby creating an avalanche of charged particles. This momentary occurrence generates a pulse of current which passes from the negative electrode to the positive electrode and is counted per time by the microcontroller. The counts per minute (cpm) alongside the ultraviolet radiation mV reading and the corresponding UV index are logged in a csv file.

4. Results and Discussion

Fig. 5 shows the output from the UV sensor (mV), while Fig. 6 shows the corresponding UV index chart. These variations were between 10 am and 2 pm at an update cycle of 5 minutes for a period of three (3) days at a specific location: latitude: 6.84, longitude: 7.35, altitude: 432 m, as indicated by the GPS sub-system.

The noticeable correlation in the two Figs. (5 and 6) shows that the modeling of the UV index chart by the instrument based on the output of the UV sensor and the UV index chart were quite good enough to give an understanding of safety levels, appropriate response and precautionary measures to be taken at certain exposure levels. The good fit in Fig. 5 for the three days under review is also an indication of good repeatability of the characterizing instrument. The UV index ranges from a minimum value of 0 to a maximum value of 3. According to the Global Solar UV Index report, [10], values ranging from 0 to < 2 are considered low with no protection required. On the other hand, values ranging from 3-5 are considered moderate with some level of protection required. It is then implied from the results obtained that the UV radiation ranges from low to moderate with some level of protection required in cases where the magnitude of the UV index exceeds 2. Global Solar UV Index report [10] identifies the factors which influence the UV levels, such as sun elevation, latitude, cloud cover, altitude, ozone layer and ground reflection. An increase in the altitude will result in an increase in the UV index and the closer the latitude to the equatorial regions, the higher the UV-radiation levels and *vice versa*. The higher the sun in the sky, the higher the UV-radiation level and *vice versa*. The UV-radiation levels vary with the time of the day and the time of the year. The highest level of the UV-radiation is usually obtained when the sun is at its maximum elevation outside the tropics and at around the midday (solar noon) during the summer months. The presence of clouds reduces the UV levels as UV-radiation levels are highest under cloudless skies. However, even with cloud cover, the UV-radiation levels can be sometimes high. The effect of scattering can have the same effect as the reflectance by different surfaces hence increasing the total UV-radiation levels [10]. The presence of the ozone layer also reduces the level of UV radiation. The ozone layer can absorb some of the UV radiation that would otherwise reach the earth's surface. In the event of continuous depletion of the ozone layer, gradual increase in the mV reading, the UV index and the frequency of occurrence of ionizing radiation in cpm, over time, would be the indications. Also, if these parameters drop in values recorded over time, this would suggest the healing of the ozone layer.

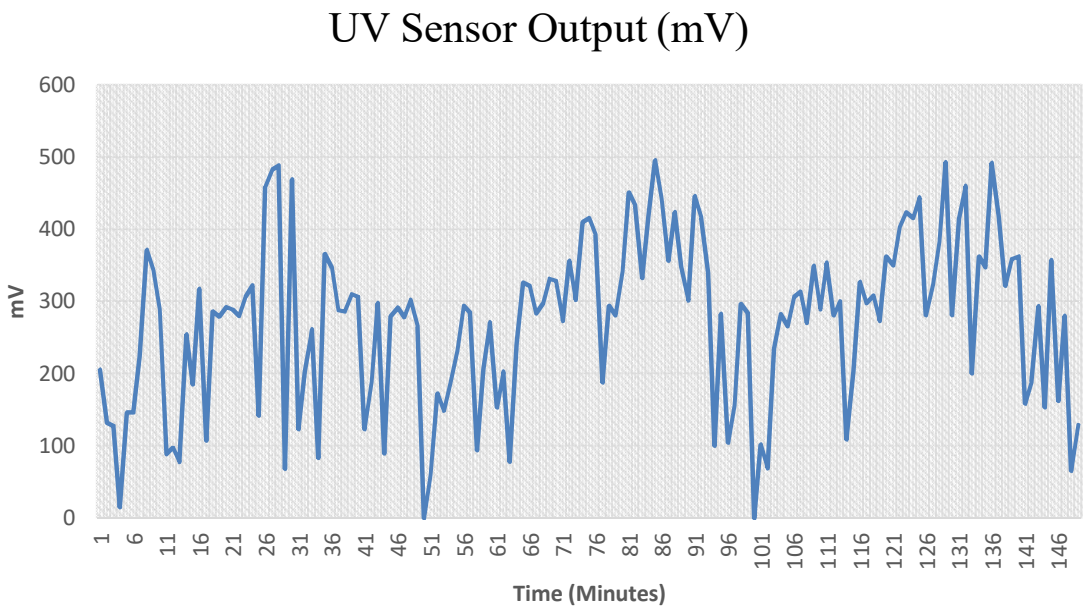

FIG. 5. Variations of the UV sensor (mV).

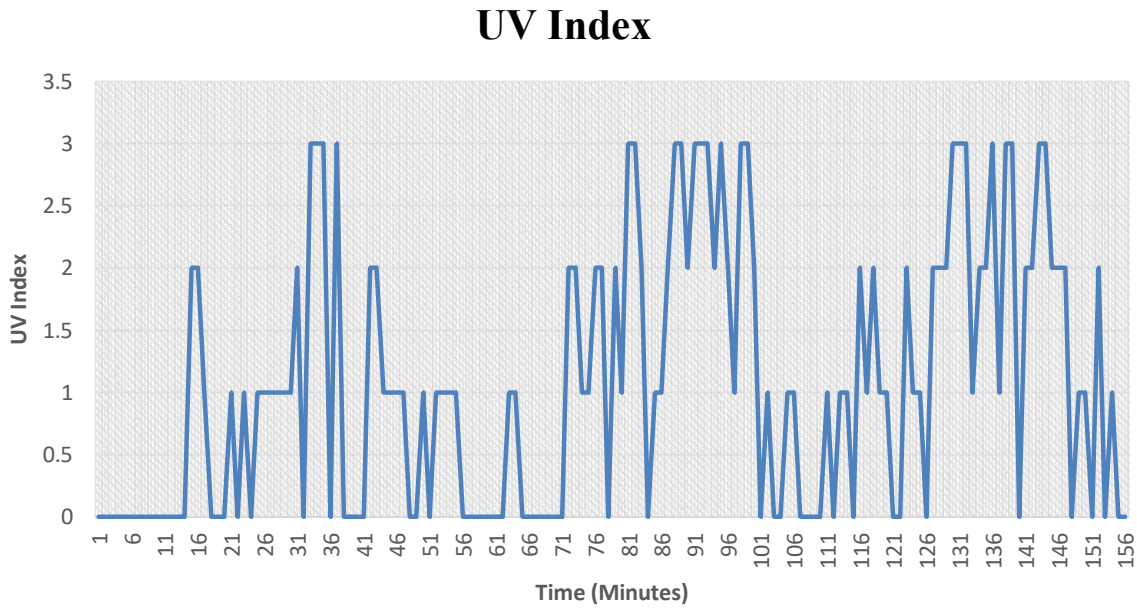

FIG. 6. UV index variations.

Fig. 7 shows the frequency of arrival of cosmic ionizing radiations in counts per minute as detected by the Geiger counter sub-system at a specific location: latitude: 6.84, longitude: 7.35, altitude: 432 m, as indicated by the GPS sub-system. These variations are between 10 am and 2 pm and at an update cycle of five minutes for a test period of three days. These variations over a much longer period of time would provide insights into the status and dynamics of the ozone layer and its permeability to UV radiations around the equatorial region through the ground-based measurement approach. The standard unit of radiation dose in an area is measured in micro-Sievert/hour (μSv/hr). Hence, the result obtained for the counts per minute (CPM) is multiplied by 0.0057 to obtain its equivalent radiation level in μSv/hr [27]. This implies that the radiation dose in the area ranges from a minimum value of 0 to a maximum value of 0.2736 μSv/hr for a period of 3 days.

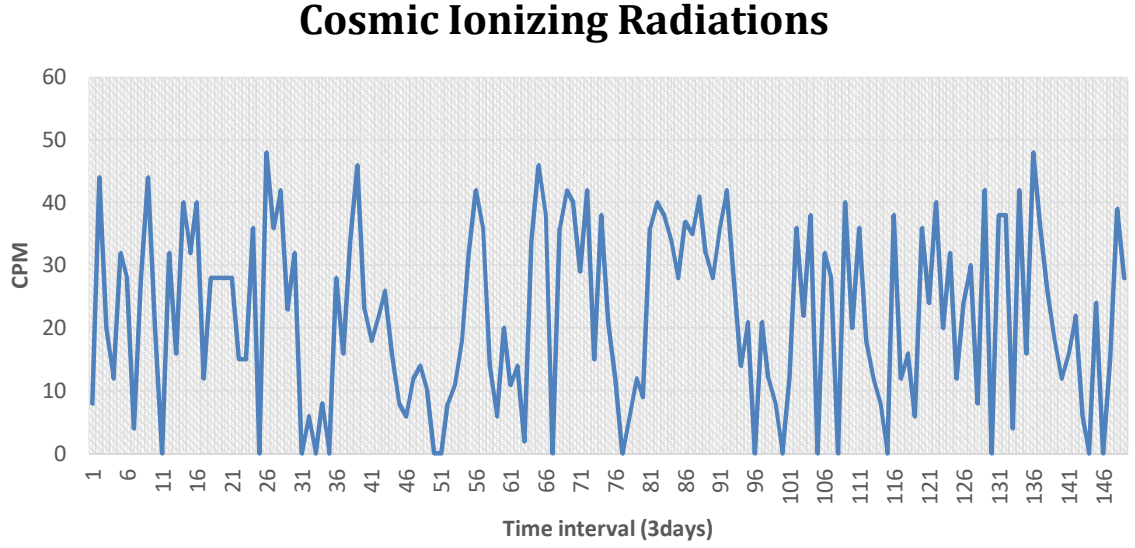

FIG. 7. Cosmic ionizing radiation variations.

The maximum mean body effective dose limit is 20 milliSieverts (mSv) per year (averaged over 5 years) [28-29]. This is recommended for people exposed to radiation as part of their occupation (including air-flight crew), while 1 mSv/year is recommended for the general population. More performance evaluation of the developed radiometer should be carried out over the period of at least one year in order to obtain the average cosmic radiation, so that comparison analysis can be carried out with the recommended standards. This will also give an indication of the permeability of the ozone layer to cosmic particles.

5. Conclusion

The aim of this study was to develop a radiometer for ground-based UV/ cosmic particle characterization. This was achieved by integrating a UV sensor, a Geiger counter, a GPS module and an SD memory card to a central microcontroller. The casing of the system was developed additively using the PETG filament. The results obtained indicate that the UV index ranges from a minimum value of 0 to a maximum value of 3, while the ionizing radiation count ranges from a minimum value of 0 to a maximum value of 48 cpm for 3 days under review. The results obtained from the performance evaluation also indicate that the UV index chart was quite good enough to give an understanding of safety levels, appropriate response and precautionary measures to be taken at certain exposure levels. The good fit for the three days review is also an indication of good repeatability of the characterizing instrument. Following a reliable means of UV measurement and Geiger counts, it is envisaged that adequate inference could be drawn from a review of much longer period of data gathering, with a view to ascertain the status of the ozone layer. The UV and cosmic ionizing radiation variations over a much longer period would provide insights into the status and dynamics of the ozone layer and its permeability to cosmic radiations around the equatorial region through the ground-based measurement approach.

Also, effective sensitization programs can be developed in order to enhance the public health and the general approach to sun protection. It is envisaged that the use of the developed system will enhance the particle characterization of cosmic rays. Future works can consider a review of at least two years.

References

[1] Leszczynski, K., "Assessment and Comparison of Methods for Solar Ultraviolet Radiation Measurements", (Helsinki, 1995), pp. 1-69.

[2] Bolonkin, A. and Friedlander, J., Scientific Research Journal of Computational Water, Energy and Environmental Engineering, 2 (2013) 83.

[3] The Universe Today “Characteristics of the Sun”, Space and Astronomy New, [Online]. www.universetoday.com/94252/characteristics-of-the-sun/. Retrieved on 6th March, 2012.

[4] Utomo, Y.S., Journal of Physics: Conf. Series, 817 (2017) 012045.

[5] International Space Science Institute, "Cosmic Rays", (Association Pro ISSI, Zurich, 2003), pp. 1-16.

[6] Kudela, K., 30th International Cosmic Rays Conference, Merida, Mexico, (2007).

[7] Putze, A., Master Thesis, Physics and Engineering: Sub-atomic Physics and Astroparticles, Joseph Fourier University at Grenoble, (2006), France.

[8] Goldhagen, P., Clem, J.M. and Wilson, J.W., Radiation Protection Dosimetry, 110 (1-4) (2004) 387.

[9] National Research Council (NRC). Health risks from exposure to low levels of ionizing radiation. BEIR VII Phase 2 report. National Academies Press; (2006). 3. Durante M. and Cucinotta, F.A., Physical basis of radiation protection.

[10] NASA, “Chemistry of the Ozone”, (2013).

[11] Global Solar UV Index: A Practical Guide, World Health Organisation, (2002), Geneva, Switzerland.

[12] Simonsen, L.C., Slaba, T.C., Guida, P. and Rusek, A., PLoS Biol., 18 (5) (2020) 1.

[13] Slaba, T.C., Blattnig, S.R., Norbury, J.W., Rusek, A. and La Tessa, C., Life Sciences in Space Research, 8, (2016) 52.

[14] Marinan, A.D., Cahoy, K.L., Bishop, R.L., Lui, S.S., Bardeen, J.R., Mulligan, T., Blackwell, W.J., Leslie, R.W., Osaretin, I.A. and Shields, M., IEEE Journal of Selected Topics In Applied Earth Observations and Remote Sensing, 9 (12) (2016) 5703.

[15] Mendonça, R.R.S., Wang, C., Braga, C.R., Echer, E., Lago, A.D., Costa, J.E.R., Munakata, K., Li, H., Liu, Z., Raulin, J-P., Kuwabara, T., Kozai, M., Kato, C., Rockenbach, M., Schuch, N-J., Al-Jasser, H.K., Sharma, M.M., Tokumaru, M., Duldig, M.L., Humble, J.E., Evenson, P. and Sabbah, I., Journal of Geophysical Research: Space Physics, 124 (2019) 9791.

[16] Park, D-H., Oh, S-H. and Lim, J-H., Sensors, 19 (754) (2016) 1.

[17] LAPIS Semiconductor, "ML8511 Datasheet", FEDL8511 – 05, March, (2013).

[18] Project Hub, "Geiger Counter with Arduino Uno", DEEDU/ Erasmus/ European Commission Project no. 2018-1 FR02 – KA205 – 014144, Jan (2018).

[19] Tysk, C., Olsson, A. and Brenner, E., "Construction of a Geiger Counter for Cosmic Radiation Measurement in near Space Conditions", (Uppsala University, June 2018).

[20] KimGrity, "LM6009 S DC-DC Power Step-up Module 3 – 34V to 4 – 35V DIY Module" [Online], www.kimgrity.com/dccdc-coverter. Retrieved on 6th March, (2012).

[21] Atmel, "ATMega328P" ATMega328P Datasheet 7810D-AVR, Jan (2015).

[22] Wanhao, "3D Printer I3 Plus Instruction Manual", Model: Duplicator I3.

[23] Daniyan, I.A., Mpofu, K., Oyesola, M.O. and Daniyan, L., Procedia CIRP, 95 (2020) 89.

[24] Daniyan, I.A., Balogun, V., Mpofu, K. and Omigbodun, F.T., International Journal on Interactive Design and Manufacturing, 14 (2020) 651.

[25] Daniyan, I.A., Mpofu, K., Daniyan, O.L., Fameso, F. and Oyesola, M., The International Journal of Advanced Manufacturing Technology, 107 (2020) 4517.

[26] Webb, G.M. and Gleeson, L.J., Journal of Astrophysics and Space Science, 60 (2) (1979) 335.

[27] Parlante, N. (2012). Nick's Geiger Counter Page. [Online], Availale at: https:// cs.stanford.edu/people/nick/geiger. Accessed on 13th August, 2021.

[28] Walker, S.A., Townsend, L.W. and Norbury, J.W., Space Res., 51 (2013) 1792.

[29] International Commission on Radiological Protection (ICRP), ICRP Publication 136, Ann. ICRP, 46 (2) (2017) 1.

المراجع: يجب طباعة المراجع بأسطر مزدوجة ومرقمة حسب تسلسلها في النص. وتكتب المراجع في النص بين قوسين مربعين. ويتم اعتماد اختصارات الدوريات حسب نظام Wordlist of Scientific Reviewers.

الجداول: تعطى الجداول أرقاما متسلسلة يشار إليها في النص. ويجب طباعة كل جدول على صفحة منفصلة مع عنوان فوق الجدول. أما الحواشي التفسيرية، التي يشار إليها بحرف فوقي، فتكتب أسفل الجدول.

الرسوم التوضيحية: يتم ترقيم الأشكال والرسومات والرسومات البيانية (المخططات) والصور، بصورة متسلسلة كما وردت في النص.

تقبل الرسوم التوضيحية المستخرجة من الحاسوب والصور الرقمية ذات النوعية الجيدة بالأبيض والأسود، على ان تكون أصيلة وليست نسخة عنها، وكل منها على ورقة منفصلة ومعرفة برقمها بالمقابل. ويجب تزويد المجلة بالرسومات بحجمها الأصلي بحيث لا تحتاج إلى معالجة لاحقة، وألا تقل الحروف عن الحجم 8 من نوع Times New Roman، وألا تقل سماكة الخطوط عن 0.5 وبكثافة متجانسة. ويجب إزالة جميع الألوان من الرسومات ما عدا تلك التي ستنشر ملونة. وفي حالة إرسال الرسومات بصورة رقمية، يجب أن تتوافق مع متطلبات الحد الأدنى من التمايز (1200 dpi Resolution) لرسومات الأبيض والأسود الخطية، و 600 dpi للرسومات باللون الرمادي، و300 dpi للرسومات الملونة. ويجب تخزين جميع ملفات الرسومات على شكل (jpg)، وأن ترسل الرسوم التوضيحية بالحجم الفعلي الذي سيظهر في المجلة. وسواء أرسل المخطوط بالبريد أو عن طريق الشبكة (Online)، يجب أرسال نسخة ورقية أصلية ذات نوعية جيدة للرسومات التوضيحية.

مواد إضافية: تشجع المجلة الباحثين على إرفاق جميع المواد الإضافية التي يمكن أن تسهل عملية التحكيم. وتشمل المواد الإضافية أي اشتقاقات رياضية مفصلة لا تظهر في المخطوط.

المخطوط المنقح (المعدّل) والأقراص المدمجة: بعد قبول البحث للنشر وإجراء جميع التعديلات المطلوبة، فعلى الباحثين تقديم نسخة أصلية ونسخة أخرى مطابقة للأصلية مطبوعة بأسطر مزدوجة، وكذلك تقديم نسخة إلكترونية تحتوي على المخطوط كاملا مكتوبا على Microsoft Word for Windows 2000 أو ما هو استجد منه. ويجب إرفاق الأشكال الأصلية مع المخطوط النهائي المعدل حتى لو تم تقديم الأشكال إلكترونيا. وتخزن جميع ملفات الرسومات على شكل (jpg)، وتقدم جميع الرسومات التوضيحية بالحجم الحقيقي الذي ستظهر به في المجلة. ويجب إرفاق قائمة ببرامج الحاسوب التي استعملت في كتابة النص، وأسماء الملفات على قرص مدمج، حيث يعلَم القرص بالاسم الأخير للباحث، وبالرقم المرجعي للمخطوط للمراسلة، وعنوان المقالة، والتاريخ. ويحفظ في مغلف واقٍ.

حقوق الطبع

يُشكِّل تقديم مخطوط البحث للمجلة اعترافاً صريحاً من الباحثين بأنّ مخطوط البحث لم يُنْشَر ولم يُقَدَّم للنشر لدى أي جهَة أخرى كانت وبأي صيغة ورقية أو إلكترونية أو غيرها. ويُشترط على الباحثين ملء أنموذج يَنُصُّ على نقْل حقوق الطبع لتُصبح ملكاً لجامعة اليرموك قبل الموافقة على نشر المخطوط. ويقوم رئيس التحرير بتزويد الباحثين بإنموذج نقل حقوق الطبع مع النسخة المُرْسَلَة للتنقيح. كما ويُمنع إعادة إنتاج أيِّ جزء من الأعمال المنشورة في المجلّة من دون إذن خَطِّيٍّ مُسبَق من رئيس التحرير.

إخلاء المسؤولية

إن ما ورد في هذه المجلة يعبر عن آراء المؤلفين، ولا يعكس بالضرورة آراء هيئة التحرير أو الجامعة أو سياسة اللجنة العليا للبحث العلمي أو وزارة التعليم العالي والبحث العلمي. ولا يتحمل ناشر المجلة أي تبعات مادية أو معنوية أو مسؤوليات عن استعمال المعلومات المنشورة في المجلة أو سوء استعمالها.

الفهرسة: المجلة مفهرسة في:

Scopus	ULRICHSWEB GLOBAL SERIALS DIRECTORY

معلومات عامة

المجلة الأردنية للفيزياء هي مجلة بحوث علميّة عالمية متخصصة مُحكمة تصدر بدعم من صندوق دعم البحث العلمي والابتكار، وزارة التعليم العالي والبحث العلمي، عمان، الأردن. وتقوم بنشر المجلة عمادة البحث العلمي والدراسات العليا في جامعة اليرموك، إربد، الأردن. وتنشر البحوث العلمية الأصيلة، إضافة إلى المراسلات القصيرة Short Communications، والملاحظات الفنية Technical Notes، والمقالات الخاصّة Feature Articles، ومقالات المراجعة Review Articles، في مجالات الفيزياء النظرية والتجريبية، باللغتين العربية والإنجليزية.

تقديم مخطوط البحث

تقدم البحوث عن طريق إرسالها إلى البريد الإلكتروني : jjp@yu.edu.jo

تقديم المخطوطات إلكترونيًا: اتبع التعليمات في موقع المجلة على الشبكة العنكبوتية.

ويجري تحكيمُ البحوثِ الأصيلة والمراسلات القصيرة والملاحظات الفنية من جانب مُحكّمين اثنين في الأقل من ذوي الاختصاص والخبرة. وتُشَجّع المجلة الباحثين على اقتراح أسماء المحكمين. أما نشر المقالات الخاصّة في المجالات الفيزيائية النَشِطَة، فيتم بدعوة من هيئة التحرير، ويُشار إليها كذلك عند النشر. ويُطْلَب من كاتب المقال الخاص تقديم تقرير واضح يتّسم بالدقة والإيجاز عن مجال البحث تمهيداً للمقال. وتنشر المجلةُ أيضاً مقالات المراجعة في الحقول الفيزيائية النشطة سريعة التغيُّر، وتُشَجّع كاتبي مقالات المراجعة أو مُستَكتبيها على إرسال مقترحٍ من صفحتين إلى رئيس التحرير. ويُرْفَق مع البحث المكتوب باللغة العربية ملخص (Abstract) وكلمات دالة (Keywords) باللغة الإنجليزية.

ترتيب مخطوط البحث

يجب أن تتم طباعة مخطوط البحث ببنط 12 نوعه Times New Roman، وبسطر مزدوج، على وجه واحد من ورق A4 (21.6 × 27.9 سم) مع حواشي 3.71 سم ، باستخدام معالج كلمات ميكروسوفت وورد 2000 أو ما استَجَد منه. ويجري تنظيم أجزاء المخطوط وفق الترتيب التالي: صفحة العنوان، الملخص، رموز التصنيف (PACS)، المقدّمة، طرق البحث، النتائج، المناقشة، الخلاصة، الشكر والعرفان، المراجع، الجداول، قائمة بدليل الأشكال والصور والإيضاحات، ثَمَّ الأشكال والصور والإيضاحات. وتُكْتَب العناوين الرئيسة بخطٍ **غامق**، بينما تُكْتَب العناوين الفرعية بخطٍ *مائل*.

صفحة العنوان: وتشمل عنوان المقالة، أسماء الباحثين الكاملة وعناوين العمل كاملة. ويكتب الباحث المسؤول عن المراسلات اسمه مشارا إليه بنجمة، والبريد الإلكتروني الخاص به. ويجب أن يكون عنوان المقالة موجزا وواضحا ومعبرا عن فحوى (محتوى) المخطوط، وذلك لأهمية هذا العنوان لأغراض استرجاع المعلومات.

الملخص: المطلوب كتابة فقرة واحدة لا تزيد على مائتي كلمة، موضحة هدف البحث، والمنهج المتبع فيه والنتائج وأهم ما توصل إليه الباحثون.

الكلمات الدالة: يجب أن يلي الملخص قائمة من 4-6 كلمات دالة تعبر عن المحتوى الدقيق للمخطوط لأغراض الفهرسة.

PACS: يجب إرفاق الرموز التصنيفية، وهي متوافرة في الموقع http://www.aip.org/pacs/pacs06/pacs06-toc.html.

المقدمة: يجب أن توضّح الهدف من الدراسة وعلاقتها بالأعمال السابقة في المجال، لا أن تكون مراجعة مكثفة لما نشر (لا تزيد المقدمة عن صفحة ونصف الصفحة مطبوعة).

طرائق البحث (التجريبية / النظرية): يجب أن تكون هذه الطرائق موضحة بتفصيل كاف لإتاحة إعادة إجرائها بكفاءة، ولكن باختصار مناسب، حتى لا تكون تكرارا للطرائق المنشورة سابقا.

النتائج: يستحسن عرض النتائج على صورة جداول وأشكال حيثما أمكن، مع شرح قليل في النص ومن دون مناقشة تفصيلية.

المناقشة: يجب أن تكون موجزة وتركز على تفسير النتائج.

الاستنتاج: يجب أن يكون وصفا موجزا لأهم ما توصلت إليه الدراسة ولا يزيد عن صفحة مطبوعة واحدة.

الشكر والعرفان: الشكر والإشارة إلى مصدر المنح والدعم المالي يكتبان في فقرة واحدة تسبق المراجع مباشرة.

Subscription Form

Jordan Journal of PHYSICS

An International Peer-Reviewed Research Journal issued by the Support of the Scientific Research and Innovation Support Fund

Published by the Deanship of Research & Graduate Studies, Yarmouk University, Irbid, Jordan

Name: ..... الأسم:

Specialty:..... التخصص:

Address: ..... العنوان:

P.O. Box:..... صندوق البريد:

City & Postal Code: ..... المدينة/الرمز البريدي:

Country: ..... الدولة:

Phone: ..... رقم الهاتف:

Fax No:..... رقم الفاكس:

E-mail:..... البريد الإلكتروني:

No. of Subscription: ..... عدد الإشتراكات:

Method of Payment:..... طريقة الدفع:

Amount Enclosed:..... المبلغ المرفق:

Signature: ..... التوقيع:

Cheques should be paid to Deanship of Research and Graduate Studies - Yarmouk University.

I would like to subscribe to the Journal
For

- One Year
- Two Years
- Three Years

One Year Subscription Rates

	Inside Jordan	Outside Jordan
Individuals	JD 8	€ 40
Students	JD 4	€ 20
Institutions	JD 12	€ 60

Correspondence

Subscriptions and Sales:

Prof. Mahdi Salem Lataifeh
Deanship of Research and Graduate Studies
Yarmouk University
Irbid – Jordan
Telephone: 00 962 2 711111 Ext. 2075
Fax No.: 00 962 2 7211121

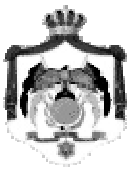

المملكة الأردنية الهاشمية

جامعة اليرموك

المجلة الأردنية
للفيزياء

مجلة بحوث علمية عالمية متخصصة محكّمة

تصدر بدعم من صندوق دعم البحث العلمي والابتكار

المجلد (15)، العدد (4)، تشرين الأول 2022م / ربيع الثاني 1444هـ

المجلة الأردنية

للفيزياء

مجلة بحوث علمية عالمية محكّمة

المجلد (15)، العدد (4)، تشرين الأول 2022م / ربيع الثاني 1444هـ

المجلة الأردنية للفيزياء: مجلة علمية عالمية متخصصة محكّمة تصدر بدعم من صندوق دعم البحث العلمي والإبتكار، عمان، الأردن، وتصدر عن عمادة البحث العلمي والدراسات العليا، جامعة اليرموك، إربد، الأردن.

ترسل البحوث إلى العنوان التالي:

الأستاذ الدكتور مهدي سالم لطايفة

رئيس تحرير المجلة الأردنية للفيزياء

عمادة البحث العلمي والدراسات العليا، جامعة اليرموك

إربد ، الأردن

هاتف 7211111 2 962 00 **فرعي** 2075

E-mail: *jjp@yu.edu.jo* **Website**: *http://Journals.yu.edu.jo/jjp*